Virgo Redux: The Masses and Stellar Content of Nuclei in Early-type Galaxies from Multiband Photometry and Spectroscopy

Chelsea Spengler[1] , Patrick Côté[2] , Joel Roediger[2] , Laura Ferrarese[2] , Rubén Sánchez-Janssen[2,3] , Elisa Toloba[4] ,
Yiqing Liu[15], Puragra Guhathakurta[7] , Jean-Charles Cuillandre[8], Stephen Gwyn[2], Andrew Zirm[9] , Roberto Muñoz[10] ,
Thomas Puzia[10], Ariane Lançon[11], Eric W. Peng[5,6] , Simona Mei[12,13,14] , and Mathieu Powalka[11]

[1] Department of Physics and Astronomy, University of Victoria, Victoria, BC V8P 5C2, Canada; spengler@uvic.ca
[2] Herzberg Institute of Astrophysics, National Research Council of Canada, Victoria, BC V9E 2E7, Canada
[3] STFC UK Astronomy Technology Centre, The Royal Observatory Edinburgh, Blackford Hill, Edinburgh, EH9 3HJ, UK
[4] Department of Physics, University of the Pacific, 3601 Pacific Avenue, Stockton, CA 95211, USA
[5] Department of Astronomy, Peking University, Beijing 100871, China
[6] Kavli Institute for Astronomy and Astrophysics, Peking University, Beijing 100871, China
[7] UCO/Lick Observatory, Department of Astronomy and Astrophysics, University of California Santa Cruz, 1156 High Street, Santa Cruz, CA 95064, USA
[8] CEA/IRFU/SAp, Laboratoire AIM Paris-Saclay, CNRS/INSU, Université Paris Diderot, Observatoire de Paris, PSL Research University,
F-91191 Gif-sur-Yvette Cedex, France
[9] Greenhouse Software, 3rd Floor, 110 5th Avenue, New York, NY 10011, USA
[10] Institute of Astrophysics, Pontificia Universidad Católica de Chile, Av. Vicuña Mackenna 4860, 7820436 Macul, Santiago, Chile
[11] Observatoire Astronomique de Strasbourg, Université de Strasbourg, CNRS, UMR 7550, 11 rue de l'Université, F-67000 Strasbourg, France
[12] LERMA, Observatoire de Paris, PSL Research University, CNRS, Sorbonne Universités, UPMC Univ. Paris 06, F-75014 Paris, France
[13] University of Paris Denis Diderot, University of Paris Sorbonne Cité (PSC), F-75205 Paris Cedex 13, France
[14] Jet Propulsion Laboratory, Cahill Center for Astronomy & Astrophysics, California Institute of Technology, 4800 Oak Grove Drive, Pasadena, California, USA
[15] Sub-department of Astrophysics, Department of Physics, University of Oxford, Denys Wilkinson Building, Keble Road, Oxford OX1 3RH, UK

Abstract

We present an analysis of 39 nuclei and their early-type hosts in the Virgo Cluster using 10 broadband filters: F300W, F475W, F850LP, F160W, u^*griz, and K_s. We describe the Virgo Redux program, which provides high-resolution UV and NIR imaging. Combining this data with optical and NIR imaging from the ACS Virgo Cluster Survey and the Next Generation Virgo Cluster Survey, we estimate masses, metallicities, and ages using simple stellar population (SSP) models. For 19 nuclei, we compare to SSP parameters derived from Keck and Gemini spectra and find reasonable agreement between the photometric and spectroscopic metallicity: the rms scatter is 0.3 dex. We reproduce the nucleus–galaxy mass fraction of $0.33^{+0.09}_{-0.07}\%$ for galaxy stellar masses $10^{8.4}$–$10^{10.3}\,M_{\odot}$ with a typical precision of $\sim$35% for the nuclei masses. Based on available model predictions, there is no single preferred formation scenario for nuclei, suggesting that nuclei are formed stochastically through a mix of processes. Nuclei metallicities are statistically identical to those of their hosts, appearing 0.07 ± 0.3 dex more metal-rich on average; however, omitting galaxies with unusual origins, nuclei are 0.20 ± 0.28 dex more metal-rich. Nuclei appear to be 0.56 ± 0.12 dex more metal-rich than ultracompact dwarf galaxies (UCDs) at fixed mass. We find no clear age difference between nuclei and their galaxies, with nuclei displaying a broad range of ages. Interestingly, we find that the most massive nuclei may be flatter and more closely aligned with the semimajor axes of their hosts, suggesting that they formed through predominantly dissipative processes.

Key words: galaxies: clusters: individual (Virgo) – galaxies: elliptical and lenticular, cD – galaxies: nuclei – galaxies: photometry

1. Introduction

The spectral energy distribution (SED) of a stellar population is dictated by a host of properties, including its initial mass function (IMF), chemical composition, dust content, and detailed star formation history. The method of SED fitting aims to recover these properties by comparing observed SEDs to theoretical spectra. While a detailed knowledge of the full spectrum is necessary for a complete understanding of an object and its evolutionary history, even a rough sampling of the SED with broadband photometry can provide useful constraints on important properties such as stellar mass (e.g., Taylor et al. 2011; Mendel et al. 2014), age, and metallicity (e.g., Li et al. 2007; Salim et al. 2007; Crockett et al. 2011; Kaviraj et al. 2012; Fan & de Grijs 2014). The inclusion of ultraviolet (UV) or infrared (IR) wavelengths are especially useful for improved age and metallicity measurements (e.g., Anders et al. 2004; Kaviraj et al. 2007a; Georgiev et al. 2012;

de Meulenaer et al. 2014), or estimates of the star formation history (e.g., Yi et al. 2005; Kaviraj et al. 2007b). No matter what data are used to sample the SED, the precise choice of comparison model—and some assumptions applied during the SED fitting procedure—may introduce ambiguities into the derived parameters (Conroy & Gunn 2010; Fan & de Grijs 2012; Powalka et al. 2016). Nevertheless, SED fitting using broadband photometry can be a powerful method for characterizing the stellar populations of a stellar system, particularly in situations where spectroscopic measurements are challenging or impractical.

One such application of SED fitting using broadband photometry is the study of compact stellar nuclei—objects whose origins and properties have been the focus of numerous studies during the last decade. These nuclei, which are sometimes referred to as nuclear star clusters, are found nestled in the cores of galaxies spanning wide ranges in morphology, mass, and size. Unlike supermassive black holes (SMBHs)—

which occupy similar locations at the bottoms of their host galaxy gravitational potential wells—nuclei can be observed *directly*, providing insight into the formation and evolution of galactic cores.

Early imaging surveys with the *Hubble Space Telescope* (*HST*) found nuclei in ~50%–60% of late-type galaxies, with slightly higher nucleation fractions among the later morphologies (Phillips et al. 1996; Carollo et al. 1997, 1998). More recent surveys have increased that fraction to 65%–80% (Böker et al. 2002; Seth et al. 2006; Georgiev & Böker 2014). For early-type galaxies, the nucleation fraction is similar, at 70%–80% in the luminosity range $-19.5 \lesssim M_B \lesssim -11$ (Côté et al. 2006; Turner et al. 2012; den Brok et al. 2014).

As the name implies, compact nuclei are small, dense objects. Typical half-light radii are 2–5 pc (Böker et al. 2004; Côté et al. 2004, 2006), with some as large as tens of parsecs (Geha et al. 2002; Georgiev & Böker 2014). Estimated masses fall in the range ~10^5–$10^8 M_\odot$ (Böker et al. 2004; Walcher et al. 2005) and appear to be related to their host galaxy masses, following roughly the same relation that exists for SMBHs (Côté et al. 2006; Rossa et al. 2006; Wehner & Harris 2006; Turner et al. 2012). The existence of similar mass relationships involving nuclei and SMBHs implies that these central massive objects (CMOs) may share similar formation processes, with a gradual transition from SMBH- to nucleus-dominated CMOs as galaxy profiles smoothly transition from central light deficits to excesses (Glass et al. 2011). However, recent work suggests that the nucleus mass relation can vary with galaxy morphology, with late-type galaxies having a shallower mass relation than early types (Georgiev et al. 2016) and more concentrated galaxies having brighter—and presumably more massive— nuclei (den Brok et al. 2014). Other studies have found that SMBHs and nuclei follow relations with different slopes (Balcells et al. 2007; Graham 2012; Leigh et al. 2012; Scott & Graham 2013), so the exact nature of CMOs remains unclear.

Nuclei and galaxy colors seem to be loosely connected as well. Although nuclei display a broad range of colors, they are usually somewhat bluer than their hosts (Lotz et al. 2004; Côté et al. 2006), suggesting that their stellar populations are younger than the underlying galaxy or that they might have a steeper IMF (Goudfrooij & Kruijssen 2014). Detailed investigations of nuclei ages, however, have yielded mixed results. Some nuclei show evidence of multiple stellar populations (Rossa et al. 2006; Walcher et al. 2006; Carson et al. 2015), although this can only be determined for resolved objects. Spectroscopic studies have measured ages ranging from 10 Myr to 12 Gyr, although with a few exceptions, the nuclei ages are usually found to be younger than their host galaxies (Butler & Martínez-Delgado 2005; Seth et al. 2006; Chilingarian et al. 2007; Chilingarian 2009; Paudel et al. 2011; Guérou et al. 2015).

The relationship between nuclei and other compact stellar systems (such as globular clusters and ultracompact dwarf galaxies, hereafter GCs and UCDs) is also a matter of interest. Nuclei are quite similar in size to most GCs, but tend to be brighter by ~4 magnitudes (Böker et al. 2004; Georgiev & Böker 2014). In contrast, UCDs are somewhat larger than nuclei, with half-light radii of 10–100 pc (Drinkwater et al. 2003; Mieske et al. 2008), and yet have similar masses ($2 \times 10^6 \leqslant M_\star \leqslant 10^8 M_\odot$). The optical colors of nuclei, GCs, and UCDs in the central region of the Virgo cluster are remarkably similar (Roediger et al. 2017). A number of groups have proposed that GCs could be the progenitors of nuclei (see below), and at least some UCDs are thought to be the stripped nuclei of disrupted nucleated dwarf galaxies (Goerdt et al. 2008; Pfeffer & Baumgardt 2013).

How nuclei form is still not well understood. Generally speaking, there are two broad scenarios for their formation: star cluster infall or in situ formation. In the cluster infall scenario, GCs spiral into the galaxy's core via dynamical friction and then merge to form a massive central star cluster (e.g., Tremaine et al. 1975; Oh & Lin 2000; Lotz et al. 2001; Capuzzo-Dolcetta & Miocchi 2008; Antonini et al. 2012; Gnedin et al. 2014). The alternative scenario is that the nuclei develop from gas funneled into the galactic center, possibly as the result of a merger (e.g., Mihos & Hernquist 1994; Milosavljević 2004; Schinnerer et al. 2008; Bekki 2015). In this picture, stellar feedback can regulate the growth of the nucleus, potentially producing multiple stellar populations and leading to the M–σ relation, involving the galaxy stellar mass M and velocity dispersion σ, via the same mechanisms proposed for the growth of SMBHs (McLaughlin et al. 2006; Bourne & Power 2016). Recently, Guillard et al. (2016) proposed a wet migration model in which massive clusters form outside the galaxy center, but retain gas reservoirs to continue forming stars as they fall to the center, merging with other clusters in the process. In reality, nucleus formation is likely more complex than idealized models suggest, and some studies have indicated that nuclei probably form through a mixture of scenarios (den Brok et al. 2014; Antonini et al. 2015; Cole et al. 2017).

Although refinements to the simulations are always welcome, a robust test of any formation model will be impossible until we have a large database of compact stellar nuclei with accurately measured parameters based on high-quality, homogeneous data. Unfortunately, such studies are observationally challenging. Given their compact sizes, nuclei are only marginally resolved, even with *HST*, in all but the nearest galaxies. Bright galaxies present an additional challenge, as their nuclei must be separated from the high underlying surface brightness of the host. In addition, large sample sizes are required for a meaningful statistical analysis of nuclei properties. Although it is possible to acquire spectra with sufficient signal for age and metallicity measurements, most spectroscopic studies of nuclei have concentrated on small samples of nearby galaxies (e.g., Seth et al. 2006) or limited surveys of more distant systems (Paudel et al. 2011). Multiband imaging is thus an attractive alternative since it avoids the long observation times needed for spectroscopy, making it possible to efficiently characterize statically meaningful samples.

At a distance of 16.5 Mpc (Mei et al. 2007; Blakeslee et al. 2009), the Virgo Cluster is a convenient target for studying nuclei and their parent galaxies. It is near enough for nuclei, with typical sizes of ~$0.''05$ (4 pc; Côté et al. 2006), to be marginally resolved by *HST*. The cluster contains a vast collection of nucleated galaxies that is especially useful for studying nucleation in early-type galaxies.

Three past or ongoing surveys of Virgo Cluster galaxies can provide both high-resolution, space-based imaging and deep, ground-based imaging in broadband filters that span the UV to near-IR wavelength region. The first of these studies used the Advanced Camera for Surveys (ACS) instrument on *HST* to carry out the ACS Virgo Cluster Survey (ACSVCS; Côté et al. 2004, 2006; Ferrarese et al. 2006a, 2006b). A follow-up *HST* program, Virgo Redux, expanded the ACSVCS data set by adding UV and IR imaging. The latest, and most extensive,

program is the Next Generation Virgo Cluster Survey (NGVS; Ferrarese et al. 2012), which used the MegaCam instrument on the 3.6 m Canada–France–Hawaii Telescope (CFHT) to acquire deep, wide-field u^*giz imaging over 104 deg^2 of the Virgo Cluster. Using the NGVS, it is possible to identify and study nuclei belonging to galaxies of unprecedented faintness (R. Sánchez-Janssen et al. 2017, in preparation). The NGVS also makes it possible to study the structural and photometric properties of not just nuclei, but also GCs and UCDs (Durrell et al. 2014; Liu et al. 2015; Zhang et al. 2015). The NGVS also includes deep r-band and infrared (K_s) imaging for a subset of the NGVS fields (Muñoz et al. 2014).

In this study, we combine all available data from the ACSVCS, Virgo Redux, and NGVS (including NGVS-IR) for 39 nucleated galaxies observed in the various surveys. The combined data set consists of observations in up to 10 filters spanning the UV, optical, and near-IR regions. With high-resolution imaging from *HST*, and deep, wide-field imaging from CFHT, we are able to estimate the masses, ages, and metallicities for the nuclei and their host galaxies in a systematic and homogeneous way. Additionally, for a subset of our targets, we use high-quality optical spectra acquired with the 10 m Keck and 8 m Gemini telescopes to validate our photometrically derived parameters.

This article is organized as follows. Section 2 summarizes our sample and observations, while Section 3 describes the isophotal and 2D decomposition methods for measuring structural and photometric parameters. In Section 4, we describe the reduction and analysis of various ground-based spectroscopic observations available for a subset of the nuclei. In Section 5, we describe our SED-fitting process and present results on the nuclei properties measured from photometry and spectroscopy. We summarize our findings in Section 6 and conclude with some directions for future work.

2. Data and Observations

2.1. Sample Selection and Properties

Our 39 program galaxies were selected from three imaging surveys of the Virgo cluster that together span the UV, optical, and IR regions (i.e., wavelength in the range 0.3–2.2 μm). Figure 1 shows the giz color images created from NGVS data with the different *HST* instrument footprints overlaid. The wide spectral coverage of the data enables more precise determination of stellar population properties, particularly ages and metallicities, which have a well-known degeneracy for old or intermediate-age populations, such as those expected for many compact stellar nuclei. Figure 2 demonstrates the sensitivity of our filter set to differences in theoretical spectra for simple stellar populations (SSPs) of various ages and metallicities. The observational details of each program are explained in the following subsections, with some general information summarized in Table 1.

Here we focus on our target selection, which is largely determined by the ACSVCS sample and classifications. The ACSVCS imaged 100 early-type galaxies in the Virgo Cluster in the F475W ($\sim g$) and F850LP ($\sim z$) filters (Côté et al. 2004), covering a range of early-type morphologies (E, S0, dE, dE,N, dS0, dS0,N) with magnitudes $9.3 \lesssim B_T \lesssim 15.7$. The survey is 44% complete down to its limiting magnitude of $M_B = -15.2$.

Our sample originates from the 51 galaxies in ACSVCS that were classified as clearly nucleated (Type Ia) in Côté et al.

(2006), meaning that a King (1966) model profile was successfully fitted to the galaxy's nuclear component. While other ACSVCS galaxies were classified as likely, or possibly, nucleated, we opted to focus only on the unambiguously nucleated galaxies, as these nuclei can be most easily modeled and separated from their host galaxies. The sample was further reduced by restricting ourselves to galaxies within the $\sim$100 deg^2 NGVS survey footprint—a total of 39 galaxies. Some basic information for these galaxies, including coordinates, velocities from the NASA/IPAC Extragalactic Database (NED), and morphologies from Binggeli et al. (1985, hereafter BST85), NED and Kim et al. (2014), are given in Table 2. The more recent numerical classifications from Kim et al. (2014), which are based on Sloan Digital Sky Survey (SDSS) imaging, confirm that these are predominantly early-type systems: 21 are dwarf ellipticals (classifications in the form 4XX), while another eight are considered ellipticals (1XX). The remaining nine galaxies classified by Kim et al. (2014) are disk galaxies (2XX) or lenticulars in the other classifications listed here. The sample galaxies are distributed throughout the cluster, as shown in Figure 3. Figure 4 shows the magnitude distribution of the galaxies selected for this analysis compared to the full set of `Type 1a` galaxies, the rest of the ACSVCS, and the general population of early-type galaxies in Virgo. The program galaxies span the full magnitude range of nucleated galaxies detected in the ACSVCS and are well-distributed across this range.

2.2. HST/ACS Imaging

The ACSVCS carried out imaging with the ACS instrument (Ford et al. 1998) in its Wide Field Channel (WFC) mode (Program ID = 9401). ACS/WFC provides high-resolution (FWHM $\approx 0.''1$) imaging across a $202'' \times 202''$ field of view with a pixel scale of $0.''049$ px^{-1}, although our final data products have been drizzled to a scale of $0.''05$ px^{-1}. Each galaxy was observed for a single orbit with two exposures per filter, plus an additional 90 s exposure in F850LP to correct any central saturation. Total exposure times were 750 s in F475W and 1210 s in F850LP. The center of each object was initially positioned on the WFC1 detector, one of the WFC's two 2048×4096 detectors, roughly $15''$–$20''$ from the chip gap, depending on galaxy brightness.

After correcting for any small offsets ($\lesssim 0.2$ px) between exposures, the images were drizzled and cosmic-ray corrected using *multidrizzle* in `PyRAF`. Sky subtraction was omitted in the drizzling process because many target galaxies in the full ACSVCS sample dominate the field of view. The drizzling process also applies a kernel to the images when distributing flux onto the final science image. The ACSVCS reduction created science images with both the "Gaussian" and "Lanczos3" kernels. For this work, we use images created with the "Gaussian" kernel, which allows for more effective bad pixel repair and therefore better estimates of the light profile in the central galaxy regions where the nucleus dominates. Point-spread functions (PSFs) were generated using DAOPHOT II (Stetson 1987, 1993) and archival observations of the globular cluster 47 Tucanae, and were allowed to have second-order variations across the field. For each galaxy, we retrieved a PSF at the nucleus' position on the chip. Additional details of the observational techniques and data reduction are available in Jordán et al. (2004a).

With its excellent resolution, high signal-to-noise ratio (S/N), and comparatively wide field of view, the ACSVCS
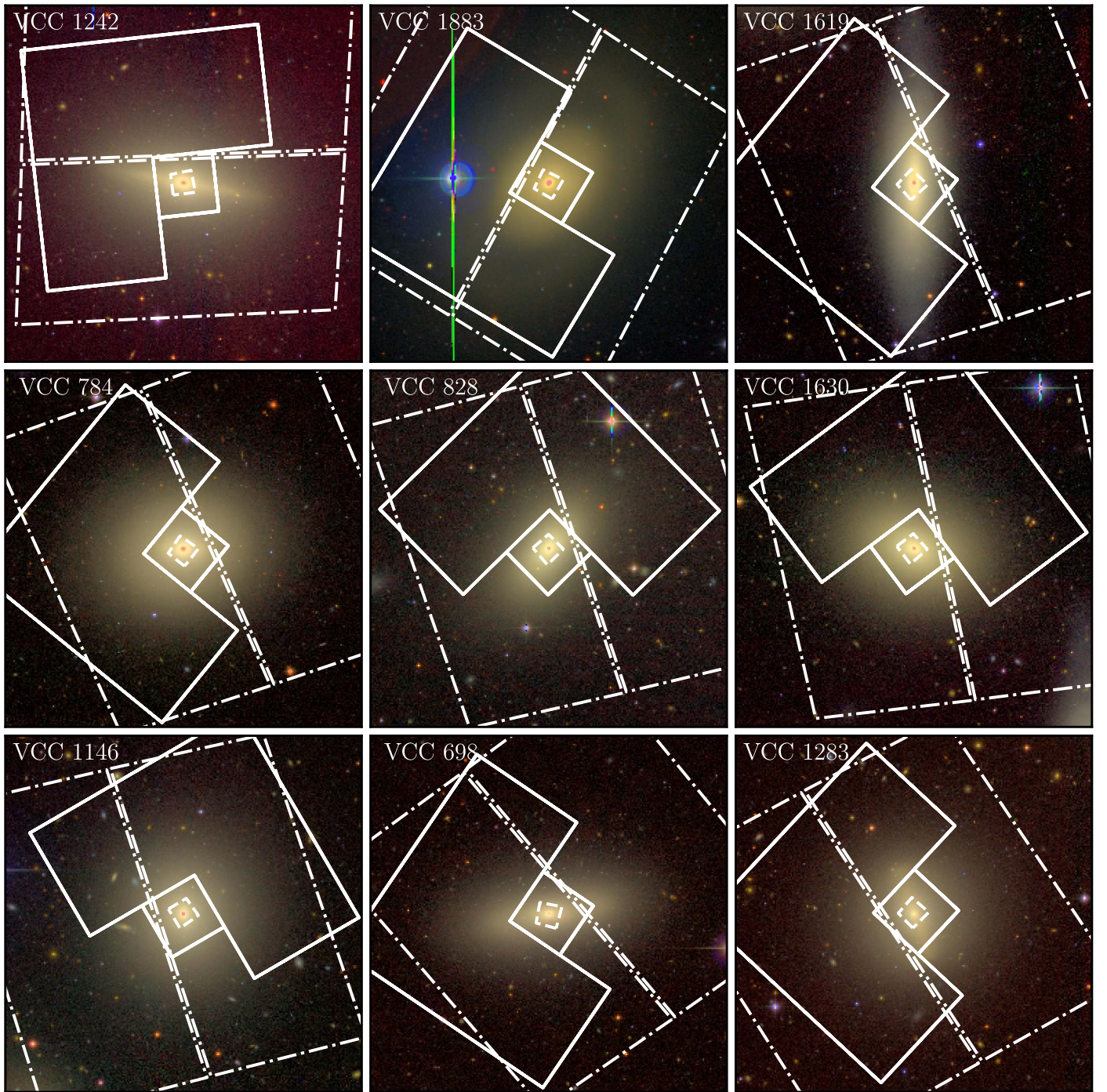
Figure 1. CFHT/MegaCam *giz* color images with *HST* instrument footprints overlaid. Galaxies are shown in order of decreasing luminosity in the F475W filter (from left to right and top to bottom). Note that the intensity scaling is not absolute across all panels. Each image measures $3\overset{'}{.}75 \times 3\overset{'}{.}75$ (18×18 kpc) and thus covers only a small fraction of the MegaCam 1 deg^2 field. ACS/WFC footprints are shown as dashed–dotted lines, NICMOS footprints are show as dashed lines, and WFPC2 footprints are shown as solid lines. In all cases, north is up and east is to the left.

data are the clear choice for reference images in the 2D decompositions of our program galaxies. Figure 5 shows $20'' \times 20''$ (1.6×1.6 kpc) cutouts of the nuclear regions for the data set. The nuclei are prominent and resolved in most of the galaxies, which aids in modeling and separating the nucleus and galaxy components. We therefore use the ACS F475W image to measure one set of structural parameters, which are then applied to the full data set. This procedure is described fully in Section 3.2.

2.3. CFHT Imaging: MegaCam and WIRCam

Full details on the NGVS observing strategy and data reduction procedures can be found in Ferrarese et al. (2012) and Muñoz et al. (2014). Here, we briefly explain the salient details of the observations.

NGVS was allocated ~ 900 hr between 2008 and 2013 with the MegaCam (Boulade et al. 2003) instrument on CFHT. The survey was designed to cover 104 deg^2 of the Virgo Cluster in the u^*, g, r, i, and z bands—an area that fully covers the region
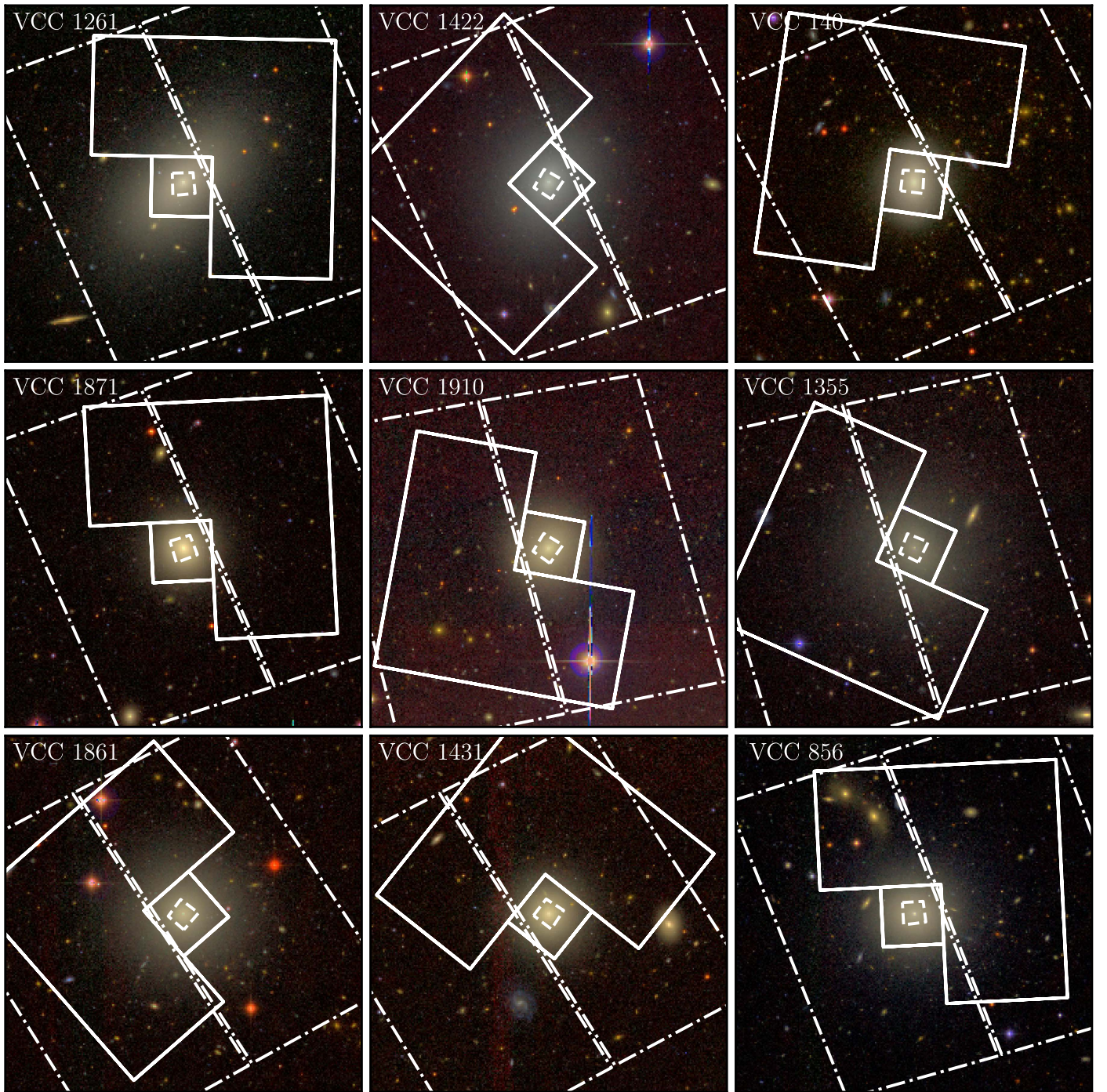
Figure 1. (Continued.)

within the virial radii of the Virgo A and B subclusters (which are centered on the galaxies M87 and M49, respectively; see Figure 3). Unfortunately, bad weather and dome shutter problems made it impossible to complete the r-band imaging; therefore, full-depth r-band exposures are available for only $\approx 9\ \mathrm{deg}^2$. Complete coverage of the survey region is available in the u^*giz bands.

Each MegaCam exposure covers 0.96×0.94 on the sky using a mosaic of 36 CCDs arranged in a 4×9 grid. With a pixel scale of $0\rlap{.}''187\ \mathrm{px}^{-1}$ and typical seeing $0\rlap{.}''7$, the PSF is well-sampled. The data are of good quality, with a median seeing of $0\rlap{.}''88$, $0\rlap{.}''80$, $0\rlap{.}''54$, and $0\rlap{.}''75$ in the u^*, g, i, and z

bands, respectively. The long exposure data used in this work have exposure times between 2055s in i and 6402s in u^*, and reach limiting surface brightnesses of 29.3, 29.0, 27.4, and 26.0 AB mag arcsec^{-2} in the u^*, g, i, and z bands, respectively.

All NGVS data were reduced using the *Elixir* pipeline, which carries out bias subtraction, flat-fielding, and bad pixel masking, and applies a fringing correction to the i- and z-band images. A number of stacked science images were then produced using the *MegaPipe* pipeline (Gwyn 2008). In this pipeline, all frames are matched to the SDSS DR7 astrometric and photometric catalogs to produce astrometric corrections and photometric zeropoints. For this paper, we
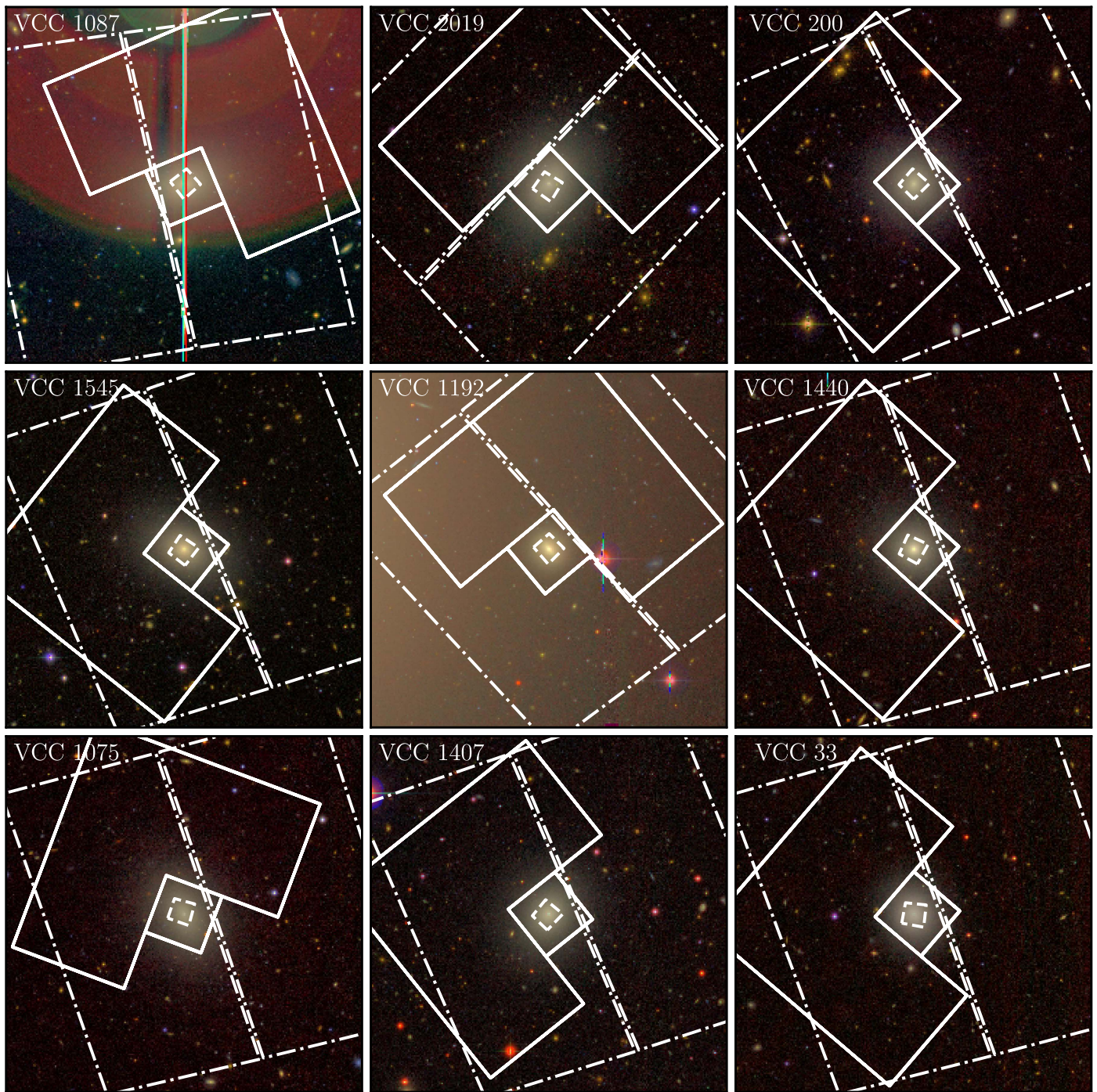
Figure 1. (Continued.)

use the "global background subtraction" stacks. In these stacks, a background map, estimated from median-combined archival MegaCam imaging processed with *Elixir*, is scaled to each frame and then subtracted. Although these stacks tend to have higher sky residuals (a few percent of the background level) compared to those created using *Elixir-LSB*, we nevertheless use them for this analysis because they are available for all filters—*Elixir-LSB* requires the input images to be acquired in a specific dither pattern, which was not possible for the *r* band. Despite the sky residuals, our chosen stacks have superior photometric accuracy compared to the other stacking techniques. PSFs were created using DAOPHOT and stars in each

frame detected by both DAOPHOT and SExtractor. As with the ACS PSFs, second-order variations were permitted, and a PSF in each filter was generated for the position of the nucleus.

The NGVS includes K_s-band imaging from the Wide-Field InfraRed Camera (WIRCam; Puget et al. 2004) over the $2° \times 2°$ region centered on M87 (Muñoz et al. 2014). WIRCam has a $21' \times 21'$ field of view covered by four detectors with a pixel scale of $0\rlap{.}''3\,\mathrm{px}^{-1}$. A total of 36 pointings were made between 2009 December and 2010 July. Each pointing was built from a series of 25 s exposures observed in specific dither patterns designed to cover the $45''$ chip gap between detectors, to ensure that each pixel covers a different
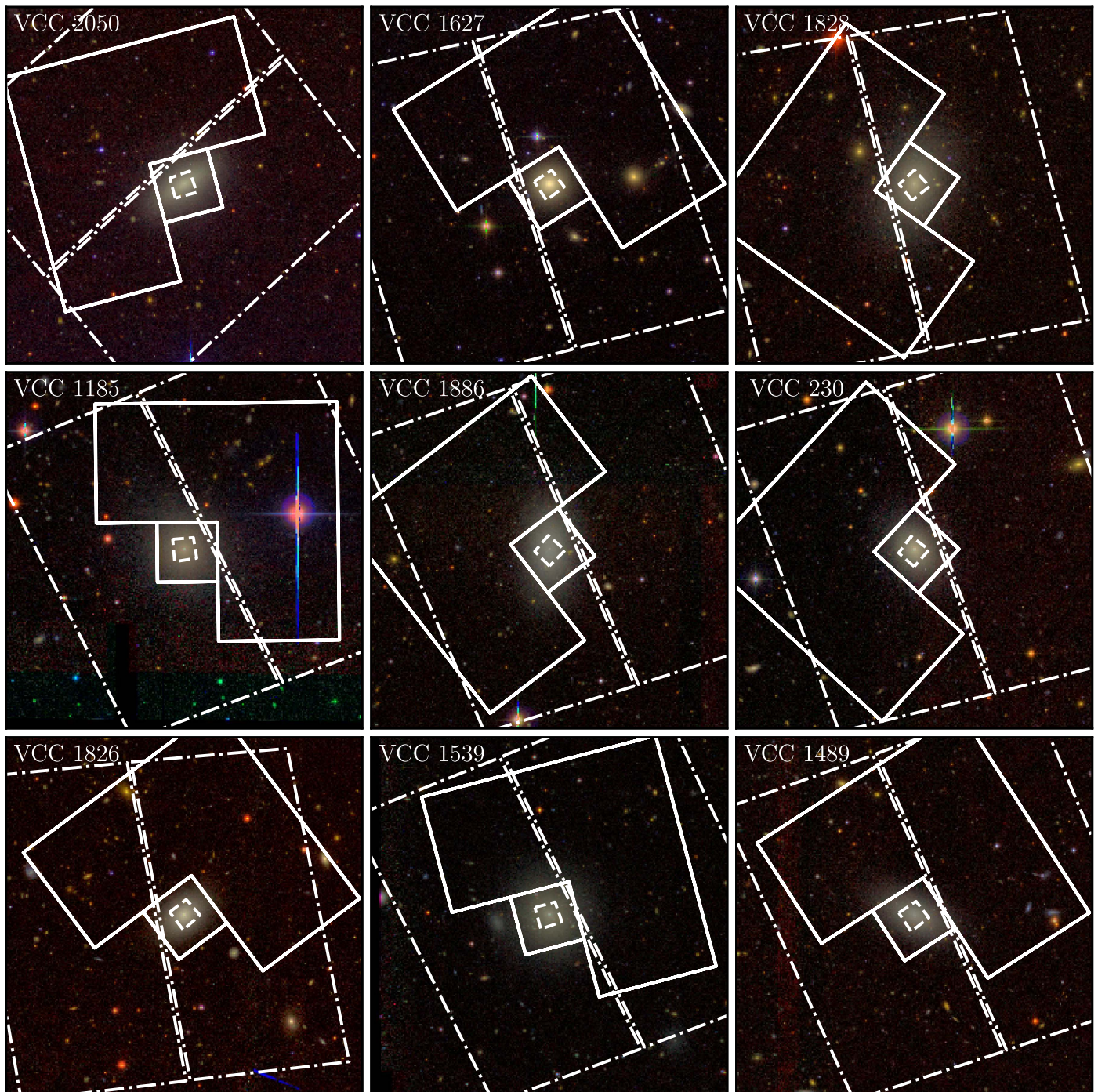
Figure 1. (Continued.)

sky region for each exposure, and to enable precise sky subtraction. Total exposure times were 2700 s per pointing. The raw images were processed for dark subtraction, nonlinearity correction, flat-fielding, and bad pixel masking using the 'I'iwi 2.0 pipeline.[16] After removing cosmic-rays and satellite trails, sky subtraction was performed in two steps. First, a median sky for each science frame was calculated using designated sky pointings and then subtracted from the target frames. The sky-subtracted frames were then stacked, and all sources identified in the stacked image were masked in each sky frame. New median skies were created with the masked sky frames and subtracted from the stacked target images. Additional corrections for variations in the amplifiers of each detector and large-scale sky fluctuations were also applied. Astrometric and photometric calibrations were performed by comparing to 2MASS, resulting in an astrometric accuracy better than $0\rlap{.}''02$ and zeropoint uncertainty lower than 0.02 mag.

Images with seeing better than $0\rlap{.}''7$ were selected to create four stacked frames that mirror the NGVS MegaCam positions and field of view for the 2 deg $\times$ 2 deg region around M87.

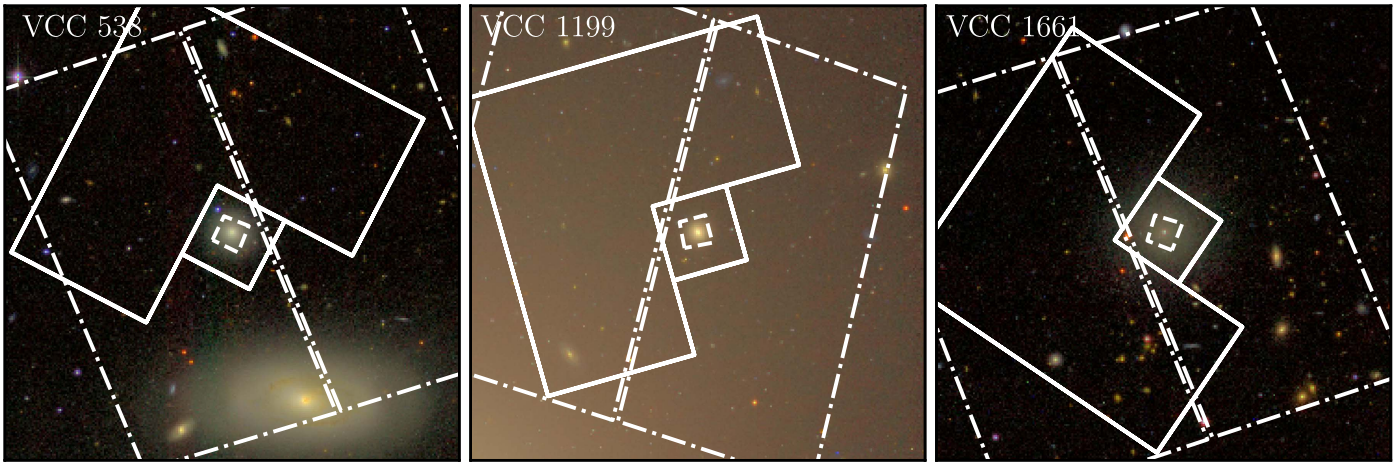[16] http://www.cfht.hawaii.edu/Instruments/Imaging/WIRCam/IiwiVersion2Doc.html

Figure 1. (Continued.)

These final images have a pixel scale $0\rlap{.}{''}186$ and median seeing $0\rlap{.}{''}54$. The limiting surface brightness is ~24.0 AB mag arcsec^{-2} in K_s. PSFs were generated separately for each of these four fields using PSFex (Bertin et al. 2011). Spatial variations in the PSFs were modeled with a seventh-order polynomial. As with the other data sets, we extracted PSFs at the pixel position of each nucleus.

2.4. HST/WFPC2 and HST/NICMOS Imaging

A follow-up program to the ACSVCS, Virgo Redux, re-imaged the sample of ACSVCS galaxies at the UV and IR wavelengths (Program ID = 11083). UV observations were carried out using the F300W filter on the Wide Field Planetary Camera 2 (WFPC2). Galaxies were centered on the Planetary Camera (PC) chip, which has a finer pixel scale ($0\rlap{.}{''}046$ px^{-1}) than the adjacent Wide Field (WF) chips ($0\rlap{.}{''}1$ px^{-1}). Each galaxy was observed for one orbit; three exposures were collected in order to aid in cosmic-ray rejection, for a total exposure times of 2100s. Our analysis uses only the PC chip, which measures $35'' \times 35''$, since it contains the nucleus and most of the galaxy signal for all our targets. The data were retrieved from the Hubble Legacy Archive, which provides PC exposures that have been combined and scaled to $0\rlap{.}{''}05$ px^{-1} using *multidrizzle* in PyRAF. Flat-fielding, bias and dark subtraction, removal of saturated or bad pixels, and shutter-shading correction were performed using the *calwp2* software as part of the standard WFPC2 calibration pipeline. No sky subtraction was performed since the sky has a negligible contribution to the nuclei counts.

Virgo Redux also includes IR imaging taken in the F160W filter ($\sim H$) with the Near-Infrared Camera and Multi-Object Spectrometer (NICMOS; Thompson 1994). Images were acquired using the NIC1 detector, which has a native pixel scale of $0\rlap{.}{''}043$ px^{-1} and a field of view of $11'' \times 11''$. Each galaxy was observed in a series of 12 exposures, in a spiral dither pattern, for a total exposure time of 1920s. One additional image was taken offset $2'$ from the galaxy center to aid in background sky measurements. For some of the larger, brighter galaxies in the survey, this offset pointing is likely contaminated with galaxy light, so we excluded it from our background measurements. An additional 13 exposures, offset $\sim5'$ from the galaxy center, were taken in parallel with the WFPC2 imaging to serve as blank sky fields. Flat-fielding, bias

and dark corrections, and other reduction steps were performed using the *calnica* pipeline in IRAF. NICMOS images also have a pedestal effect, appearing as a residual flat-field signature that differs for each quadrant on the detector and varies with time. We corrected for this effect using *pedsub*. Our final science images were created using *multidrizzle* and have a pixel scale of $0\rlap{.}{''}03$ px^{-1}. Note that the drizzling task was run without sky subtraction. Instead, we later subtracted a sky level based on the mean sky measured from the 13 exposures with $5'$ offsets. PSFs for all Virgo Redux images were created using the Tiny Tim package.[17]

2.5. Ground-based Spectroscopy

For 19 of the nuclei in our sample, high-quality optical spectroscopy is available from three different ground-based instruments. Although these data are only available for a subset of the objects, they provide an important point of comparison for the photometric results, allowing us to evaluate the robustness of the photometrically determined masses, ages, and metallicities (and vice versa). In a few cases, spectroscopy is available from multiple sources, which allows us to assess the level of agreement among parameters derived from the different spectroscopic data sets.

Five nuclei were observed with the Integral Field Unit (IFU; Allington-Smith et al. 2002) within the Gemini Multi-Object Spectrograph (GMOS; Hook et al. 2004) on the Gemini South telescope during the 2008A and 2009A observing seasons. The IFU's $7'' \times 5''$ field of view, containing 1000 fibers, was centered on each object and rotated to align with the galaxy's semimajor axis. Another 500 fibers were configured in a $5'' \times 3''$ field, offset by $1'$ from the center of the science field. Observations were performed in the two-slit mode using the B600 grating (600 l mm^{-1}) and g' filter, although data from one slit were excluded because the key spectral features—H$_\beta$, Mgb, and Fe Lick indices—fell on a CCD with a number of bad columns and pattern noise. Four exposures for each nucleus were acquired, giving total exposure times between 1600 and 8000 s. The final binned science spectra have a dispersion of 0.9 Å px^{-1}. Full details on the instrumental configuration and data reduction procedures are given in Liu et al. (2016).

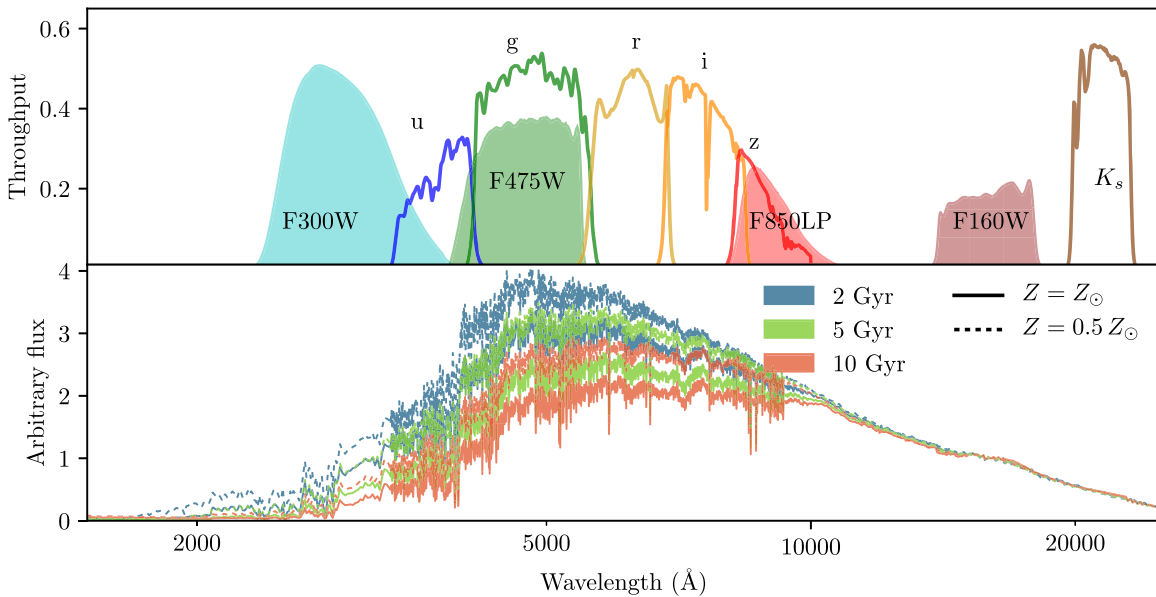[17] http://www.stsci.edu/hst/observatory/focus/TinyTim

Figure 2. (Top panel) Passbands for the different filters used in this study. Filled curves show the *HST* filters while open curves show the CFHT filters. Note that the K_s filter is only available for the six galaxies that fall inside the 2 deg × 2 deg region around M87. (Bottom panel) Model spectra for selected SSPs using the BC03 models with a Chabrier IMF. Three different ages are shown: 2, 5, and 10 Gyr (blue, green, and red lines, respectively). Solid lines denote SSPs with solar metallicity, while dotted lines correspond to populations with half solar metallicity. The spectra have been normalized at 1.6 μm in the F160W filter.

Another 17 galaxies were observed with the Echellette Spectrograph and Imager (ESI; Sheinis et al. 2002) on the Keck II telescope during the 2003A and 2004A observing seasons. In its echelle mode, ESI offers 10 spectral orders, with complete wavelength coverage from 3900 to 10900 Å at a dispersion ranging from 0.15 Å px^{-1} (for $\lambda = 3900$–4400 Å in order No. 15) to 0.39 Å px^{-1} (for $\lambda = 9500$–11000 Å in order No. 6). The spectral dispersion, in units of velocity, is a nearly constant 11.5 km s^{-1} px^{-1}. Objects were observed with either a 0″75 × 20″ or a 1″0 × 20″ slit, giving an instrumental velocity resolution between 1.0 and 1.4 Å at ~5200 Å. The processing of the raw data involved bias subtraction, finding and tracing the apertures, flat normalization, cosmic-ray removal, arc extraction, and spectral calibration. Reductions were carried out using the Mauna Kea Echelle Extraction package (MAKEE; Barlow & Sargent 1997).

Lastly, seven nuclei were observed using the DEep Imaging Multi-Object Spectrograph (DEIMOS; Faber et al. 2003) on the Keck II telescope during the 2012A observing season. The observations, which were optimized for radial velocity and chemical abundance studies of star clusters in these galaxies, were carried out using the 600 lines mm^{-1} grating centered at 7000 Å. When combined with the GG4455 filter, this set-up provided a wavelength coverage of 4800–9500 Å at a dispersion of 0.52 Å px^{-1}. Slit lengths were kept somewhat short, typically ~4″–8″, in order to place as many globular clusters, stars, and other point-like objects, including nuclei, as possible on each slit mask. A slit width of 0″8 was used in all cases. Exposure times varied between 3600 and 4800 s, with the different exposure times meant to account for variations in the observing conditions (i.e., the seeing varied between 0″6 and 0″9). Additional observational details are presented in Toloba et al. (2016) and P. Guhathakurta et al. (2017, in preparation).

A summary of the spectroscopic observations is provided in Table 3. In Figure 6, we show slit and IFU orientations for VCC 1545, one of two galaxies included in all three spectral data sets.

3. Photometric and Structural Measurements

There are a number of challenges involved in the measurement of photometric and structural parameters for nuclei, and, ultimately, in the characterization of their stellar populations. Nucleus–galaxy decompositions can be uncertain due to such factors as the number of components used in the modeling of the light distribution, the PSF used for the model convolution, and the presence of complex or nonparametric structures that may skew the model fit (see, e.g., Turner et al. 2012 for a discussion of these issues). When deriving stellar population properties, one familiar difficulty is the age–metallicity degeneracy. This is undoubtedly important for nuclei in early-type hosts, as both the galaxies and nuclei are likely to contain old to intermediate-age ($t > 5$ Gyr) populations. Age sensitivity can be improved by extending the photometric coverage into the UV and IR regions (Worthey et al. 1994; Puzia et al. 2002; Hempel et al. 2003; de Meulenaer et al. 2014)—a prime motivation for our study. Of course, the derived stellar population parameters can also vary with the choice of comparison models, which often rely on different isochrones, spectral libraries, and stellar evolution treatments (Conroy & Gunn 2010; Powalka et al. 2016).

To test the robustness of our results with these uncertainties in mind, we use multiple procedures to understand any possible systematics. This includes using different nucleus–galaxy decomposition techniques (described in Sections 3.1 and 3.2) as well as deriving stellar population parameters from various population synthesis models.

3.1. ELLIPSE-based Analysis

Nuclei and galaxy parameters were derived from Sérsic component fits to radial profiles created using the IRAF task ELLIPSE, which fits elliptical isophotes to each object using the method of Jedrzejewski (1987). The image intensity is

Table 1
Summary of Imaging

Telescope	Instrument	Field of View	Filters	Scale (arcsec px^{-1})	FWHM ($''$)	N_{gal}
(1)	(2)	(3)	(4)	(5)	(6)	(7)
HST	ACS-WFC	$202'' \times 202''$	F475W, F850LP	0.05	0.1	39
HST	WFPC2-PC	$35'' \times 35''$	F255W, F300W	0.05	0.08	37
HST	NICMOS-NIC1	$11'' \times 11''$	F160W	0.03	0.095	38
CFHT	MegaCam	$0°96 \times 0°94$	u^*griz	0.187	$\leqslant 1$	39
CFHT	WIRCam	$21' \times 21'$	K_s	0.186	$\leqslant 0.7$	6

Note. Summary of telescopes and instruments used to collect the images analyzed in this paper. All MegaCam images have seeing better than $1''$ but FWHM varies with filter; the median seeing ranges from $0\farcs54$ in i to $0\farcs88$ in u^*. Note that two galaxies (VCC 1185 and VCC 1627) are missing WFPC2 observations due to a loss of guiding during the observation; similarly, VCC 1627 is missing NICMOS data due to a guiding failure. Only six objects have K_s-band imaging because WIRCam observations are available for only the central 4 deg^2 of the Virgo cluster (Muñoz et al. 2014).

sampled along each ellipse's path, creating an intensity distribution as a function of azimuthal angle, ϕ. If the ellipse's parameters are well matched to the galaxy's shape, then the intensity should be constant at all values of ϕ. Any deviations from the isophote can be expressed as higher-order moments of a Fourier series:

$$I(\phi) = I_0 + \sum_k [A_k \sin(k\phi) + B_k \cos(k\phi)], \qquad (1)$$

where A_k and B_k represent the amplitude of each moment. A pure ellipse can be described by the first two moments of the series, while any deviations (e.g., a disky or boxy isophote) can be expressed with terms for $k \geqslant 3$. ELLIPSE determines the best-fit parameters by least-squares minimization of the residuals between the sampled image intensity and Equation (1). This isophotal fitting process is described in full in Ferrarese et al. (2006b) and Côté et al. (2006).

To capitalize simultaneously on HST's superior resolution and the depth of the wide-field NGVS imaging, composite surface brightness profiles were created by combining ACS F475W and MegaCam g-band profiles, as well as F850LP and z-band profiles. The two filter pairs are nearly identical, although a small ($\lesssim 0.01$ mag) zeropoint correction is required to transform each set to a common system. In addition, the HST profiles must have the sky removed. To accomplish both of these tasks, the g and z profiles were first transformed to the SDSS photometric system using the color transformations provided by the MegaPipe Web pages.[18] Next, we estimated the zeropoint shifts and sky levels of the ACS images simultaneously. For the ACS profiles, a corrected surface brightness profile can be calculated using the equation

$$\mu_{AB}(r) = -2.5 \log_{10}(f(r) + f_{sky}) + z + \Delta z, \qquad (2)$$

where $f(r)$ is the measured flux at each radial step, f_{sky} is the estimated sky level, z is the zeropoint for initial photometric system, and Δz is the zeropoint correction.

These corrections were determined on a galaxy-by-galaxy basis by matching the ACS profile produced by Equation (2) to the CFHT profile using the orthogonal distance regression package within SciPy. For the fit, only the profile regions beyond $4''$ were considered. This is roughly five times the seeing of the NGVS data, which should safely avoid any blurring of the nucleus and galaxy profiles (Schweizer 1979). Figure 7 shows the matched profiles for the galaxy VCC 1422

once the ACS component has been zeropoint-corrected and sky-subtracted. Residuals between the two original profiles in the fitted regions, unaffected by smearing, are shown as well.

Parametric fits to the composite profiles were produced following a method similar to that in Côté et al. (2006), Ferrarese et al. (2006a), and Turner et al. (2012). However, the approach here differs in a few ways, most notably in that we fitted the nucleus light using a Sérsic profile rather than a King profile (i.e., the entire profile nominally contains two Sérsic components). The intensity in a Sérsic profile is described by the equation

$$I(r) = I_e \exp \left\{ -b_n \left[\left(\frac{r}{r_e} \right)^{1/n} - 1 \right] \right\}, \qquad (3)$$

where the free parameters are I_e, the intensity at the effective radius r_e, and the Sérsic index n. The constant b_n is defined by complete and incomplete gamma functions, $\Gamma(n)$ and $\gamma(n, x)$, respectively, such that $\Gamma(2n) = 2\gamma(2n, b_n)$. For the nuclear component, n was fixed to $n = 2$ to diminish the likelihood of the nucleus component fitting non-nucleus light in galaxies with complex substructure.

The best-fit model was determined using χ^2 minimization with equal weight applied to all points in the profile after convolution with the appropriate PSF. Fits to the g and z profiles were performed both independently for each filter as well as simultaneously. We found that the structural parameters derived with independent and simultaneous fits were consistent, although small variations between the g and z parameters arose in the independent fits. However, each fit remained well-behaved. We adopt the results from the independent fits for our analysis.

3.2. GALFIT Analysis

Galaxy and nucleus magnitudes were measured simultaneously using GALFIT, a familiar algorithm that fits two-dimensional (2D) parametric models to images (Peng et al. 2002, 2010). A galaxy model can be composed of an arbitrary number of components (e.g., exponential disk, Sérsic profile, point source) that are combined to best fit the 2D galaxy image. As inputs, GALFIT requires the original image, a PSF image to convolve with the model component(s), and either a sigma map containing the errors for each pixel or the gain of the instrument in order to estimate errors from the Poisson noise.

---

[18] http://www.cadc-ccda.hia-iha.nrc-cnrc.gc.ca/en/megapipe/docs/filt.html

Table 2
Basic Data for Program Galaxies

VCC	Other	α(2000) (h:m:s)	δ(2000) (°:′:″)	B_T (mag)	$E(B-V)$ (mag)	V_r (km s^{-1})	BST85	NED	EVCC
(1)	(2)	(3)	(4)	(5)	(6)	(7)	(8)	(9)	(10)
33	IC3032	12:11:07.8	+14:16:29.3	14.67	0.037	1186	d:E2,N:	E?	411
140	IC3065	12:15:12.6	+14:25:58.3	14.30	0.037	993	SO1/2(4)	S0?	200
200	…	12:16:33.7	+13:01:53.7	14.69	0.030	16	dE2,N	dE2,N	411
230	IC3101	12:17:19.7	+11:56:36.5	15.20	0.028	1429	dE4:,N:	dE4:,N:	401
538	NGC4309A	12:22:14.7	+07:10:01.7	15.40	0.020	750	E0	E0	100
698	NGC4352	12:24:05.0	+11:13:05.1	13.60	0.026	2070	S01(8)	SA0: sp	200
784	NGC4379	12:25:14.7	+15:36:26.7	12.67	0.024	1074	S01(2)	S0 pec:	200
828	NGC4387	12:25:41.7	+12:48:37.9	12.84	0.033	565	E5	E5	100
856	IC3328	12:25:57.9	+10:03:13.5	14.25	0.024	1025	dE1,N	dE,N	411
1075	IC3383	12:28:12.3	+10:17:51.5	15.08	0.027	1844	dE4,N	dE4,N	401
1087	IC3381	12:28:14.9	+11:47:23.3	14.31	0.027	675	dE3,N	dE,N	401
1146	NGC4458	12:28:57.6	+13:14:30.9	12.93	0.023	677	E0-1	E0-1	100
1185	…	12:29:23.5	+12:27:02.9	15.68	0.023	500	dE1,N	dE1	401
1192	NGC4467	12:29:30.3	+07:59:34.3	15.04	0.023	1423	E3[a]	E2	200
1199	…	12:29:35.0	+08:03:28.8	15.50	0.022	1401	E2[a]	E2	100
1242	NGC4474	12:29:53.6	+14:04:06.9	12.60	0.042	1611	S01(8)	S0 pec:	200
1261	NGC4482	12:30:10.3	+10:46:46.1	13.56	0.029	1871	d:E5,N	dE,N	400
1283	NGC4479	12:30:18.4	+13:34:39.4	13.45	0.029	876	SB02(2)	SB(s)0!0!:?	210
1355	IC3442	12:31:20.2	+14:06:54.7	14.31	0.034	6210	dE2,N	E0:	…
1407	IC3461	12:32:02.7	+11:53:24.3	15.49	0.032	1019	dE2,N	dE,N	401
1422	IC3468	12:32:14.2	+10:15:05.2	13.64	0.031	1288	E1,N:	E1,N:	210
1431	IC3470	12:32:23.4	+11:15:46.7	14.51	0.051	1505	E?	E?	401
1440	IC798	12:32:33.4	+15:24:55.5	15.20	0.028	382	E0[a]	E0	100
1489	IC3490	12:33:13.9	+10:55:42.5	15.89	0.034	80	dE5,N?	E?	401
1539	…	12:34:06.7	+12:44:29.7	15.68	0.032	1491	dE0,N	dE0,N	401
1545	IC3509	12:34:11.5	+12:02:56.2	14.96	0.042	2000	E4[a]	E4	401
1619	NGC4550	12:35:30.6	+12:13:15.0	12.50	0.040	459	E7/S01(7)	SB0!0!:sp LINER	200
1627	…	12:35:37.3	+12:22:55.3	15.16	0.039	236	E0[a]	E0	100
1630	NGC4551	12:35:38.0	+12:15:50.4	12.91	0.039	1176	E2	E:	100
1661	…	12:36:24.8	+10:23:04.8	15.97	0.020	1457	dE0,N	dE0,N	401
1826	IC3633	12:40:11.3	+09:53:46.0	15.70	0.017	2033	dE2,N	dE2,N	401
1828	IC3635	12:40:13.4	+12:52:29.1	15.33	0.037	1569	dE2,N	dE,N	401
1861	IC3652	12:40:58.6	+11:11:04.2	14.37	0.029	629	dE0,N	E	401
1871	IC3653	12:41:15.7	+11:23:14.0	13.86	0.030	588	E3	E3	100
1883	NGC4612	12:41:32.8	+07:18:53.5	12.57	0.025	1775	S01(6)	(R)SAB0!0!	200
1886	…	12:41:39.4	+12:14:50.6	15.49	0.033	914	dE5,N	dE5,N	401
1910	IC809	12:42:08.7	+11:45:15.3	14.17	0.031	206	dE1,N	E	401
2019	IC3735	12:45:20.4	+13:41:33.6	14.55	0.022	1895	dE4,N	E?	411
2050	IC3779	12:47:20.6	+12:09:59.1	15.20	0.023	1156	dE5:,N	dE5:,N	400

Note. Key to columns: (1) VCC identification number, (2) alternate names in the NGC, IC, or UGC catalogs, (3) right ascension, (4) declination, (5) total B magnitude from BST85, (6) extinction from Schlafly & Finkbeiner (2011), (7) recessional velocity from NED, (8) morphological classification from BST85, (9) morphological classification from NED, and (10) morphological classification from Kim et al. (2014).
[a] Compact, low-luminosity E (M32-type) galaxy from Table XIII of BST85.

Final magnitude measurements for the various components were obtained using an iterative process. Initially, each object was fitted with a basic model containing (1) a Sérsic component for the galaxy and (2) a Sérsic component for the nucleus. These components were defined by a single ellipticity and position angle (i.e., no isophote twisting), as well as an effective radius r_e, Sérsic index n, axis ratio b/a, and magnitude. Although GALFIT can estimate and fit the sky level, its brightness was fixed to a predetermined value because the fitted images are often object, not sky, dominated, and so GALFIT's sky level estimates were found to be consistently high. For the u^*griz, F300W, and F160W images, sky subtraction had already been applied to the data, so sky levels were fixed to zero. For the ACS F475W and F850LP images, sky levels were determined from matching the F475W and F850LP one-dimensional (1D) profiles to the corresponding

CFHT g and z profiles (see Section 3.1). The output parameters of the fit obtained with the basic model were then inspected for each object. The model was subsequently refined with additional Sérsic components for the galaxy if the fit met either, or both, of the following conditions: (1) n for any component was outside the range $0.5 < n < 4$, and (2) the nucleus' r_e was more than 10% of the galaxy's r_e. This second condition, a quite conservative criterion, was imposed to catch only the most obvious outliers: i.e., typically, the nucleus radius is ∼2% of the galaxy half-light radius. In all cases, a single component was used to fit the nucleus, resulting in an average $n = 1.57 \pm 0.64$ and average $r_e = 5.74 \pm 1.74$ pc. The models were also refined if a visual inspection of the fit residuals indicated an incomplete fit, even if the above conditions were not met. Even dwarf galaxies can display multiple structural components (see, e.g., Janz et al. 2012 and
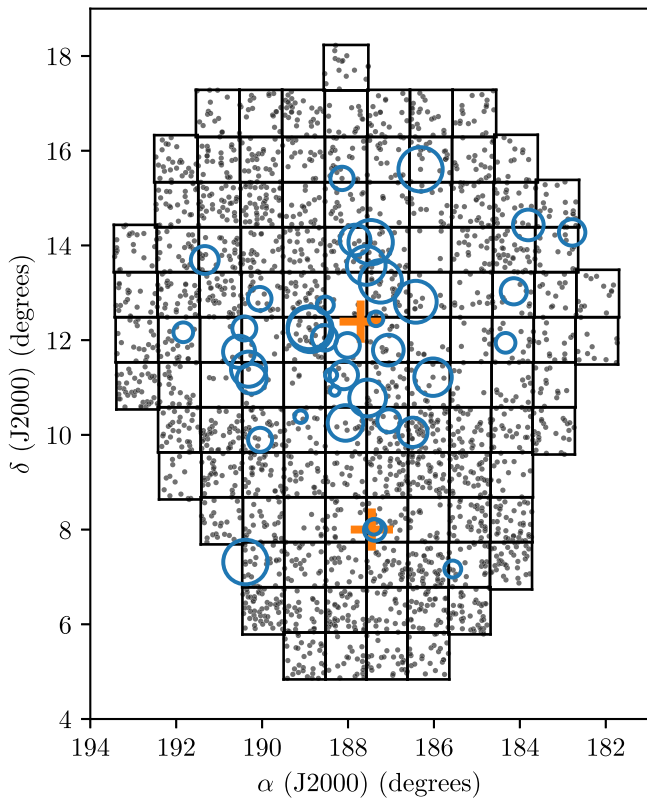
Figure 3. Distribution of the 39 galaxies selected for this analysis overlaid on the NGVS fields. Open blue circles indicate each sample galaxy. The size of the circles corresponds to galaxy brightness. M87 (VCC 1316) and M49 (VCC 1226) are labeled with orange crosses. Gray points show NGVS galaxies brighter than $M_g \simeq -14.5$.
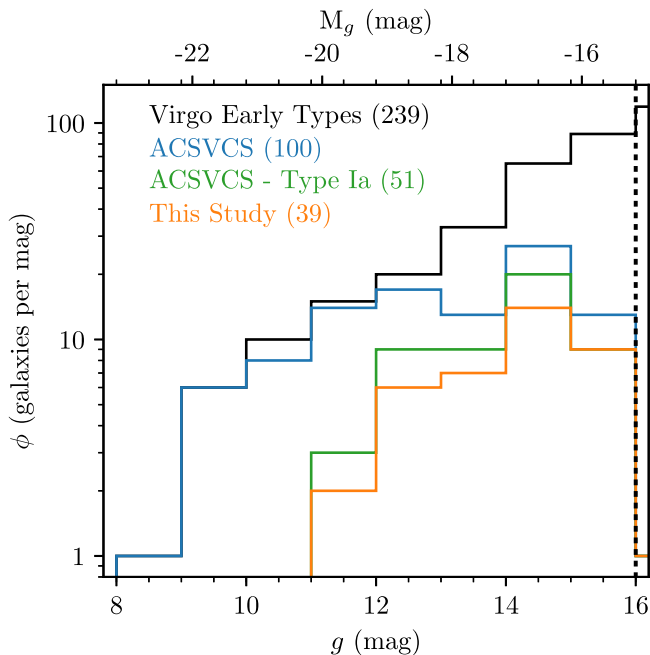

Figure 4. Magnitude distribution for the full ACSVCS sample, 51 nucleated galaxies (Type Ia), and 39 Type Ia galaxies analyzed in this work. For comparison, we also show the complete sample of Virgo early-type galaxies from Janz & Lisker (2008, 2009).

references therein), so most of the galaxies in our sample have been modeled with more than one Sérsic component, typically requiring two or three. The maximum number of components

required was seven for VCC 784, one of the brightest galaxies in the sample.

To ensure consistent measurements across all bands, the same physical parameters were held fixed and fitted to all images, with the only free parameters being the magnitudes of the model components (the sky level, however, was always held fixed). To determine the values of the fixed parameters, a completely free fit was performed on the F475W images. These are the obvious choices as reference images due to the combination of high S/N, high resolution, and relatively wide field coverage. All nuclei in this sample were resolved in the *HST* data, enabling better measurement of nuclei parameters. Once the fits to the F475W images were completed, the best-fit parameters for each object were extracted and fitted to the remaining images, with only the magnitudes being allow to vary from their input values. Using this technique, we were able to measure component magnitudes in a homogeneous way. This is particularly important for the NICMOS and WFPC2 data, where a limited field of view, or marginal S/N, can present challenges in the fitting process. Figure 8 shows the GALFIT results for three program galaxies at a range of magnitudes and structural complexities. With the flexibility of adding multiple galaxy components, even a bright, complex galaxy such as VCC 1146 can be well-modeled. For the faintest galaxies in the sample, such as VCC 1539, the fixed structural parameters ensure consistent fits, even in filters where the detection is limited. Tables 4 and 5 list the extracted magnitudes for the nuclei and galaxies, respectively. Galaxy magnitudes are defined as the total magnitude of all components *excluding* the nucleus component.

3.3. Comparison of Results

Before proceeding, we pause to consider the robustness of our magnitude measurements. For the F475W and F850LP images, it is possible to compare magnitudes derived using the two methods described in Sections 3.1 and 3.2. We can also compare the space- and ground-based 2D magnitudes from Section 3.2 to investigate the effect of resolution on the resulting values. All GALFIT F475W, F850LP, g-band, and z-band magnitudes were first transformed to the SDSS photometric system following the same procedure outlined in Section 3.1. Comparisons among the various methods in the g bandpass are shown in Figure 9. For the galaxies, we find that both ground- and space-based 2D magnitudes differ slightly from the 1D composite profile magnitudes, with a typical scatter of ∼0.1 mag. The 1D magnitudes tend to be systematically brighter in galaxies with $g \gtrsim 14$ mag. This is not surprising as the 1D and 2D models differ in complexity. We find excellent agreement between the space- and ground-based 2D galaxy magnitudes, with a typical scatter of just ∼0.02 mag.

For the nuclei, the scatter among all measurement methods is understandably larger. Adjusting the nucleus model, even dramatically, will generally have a negligible effect on the derived galaxy magnitude (or on the total magnitude of the system). When comparing the 1D and 2D magnitudes, the scatter is largest for the brightest nuclei, which have $g \lesssim 19.5$ mag. In this regime, the nuclei are embedded in the brightest and most structurally complex galaxies in our sample, and are thus the most difficult to model well (see Turner et al. 2012). These objects are also expected to be the most affected by the number of components used in the model fit, which is a factor when comparing the 1D profile measurements
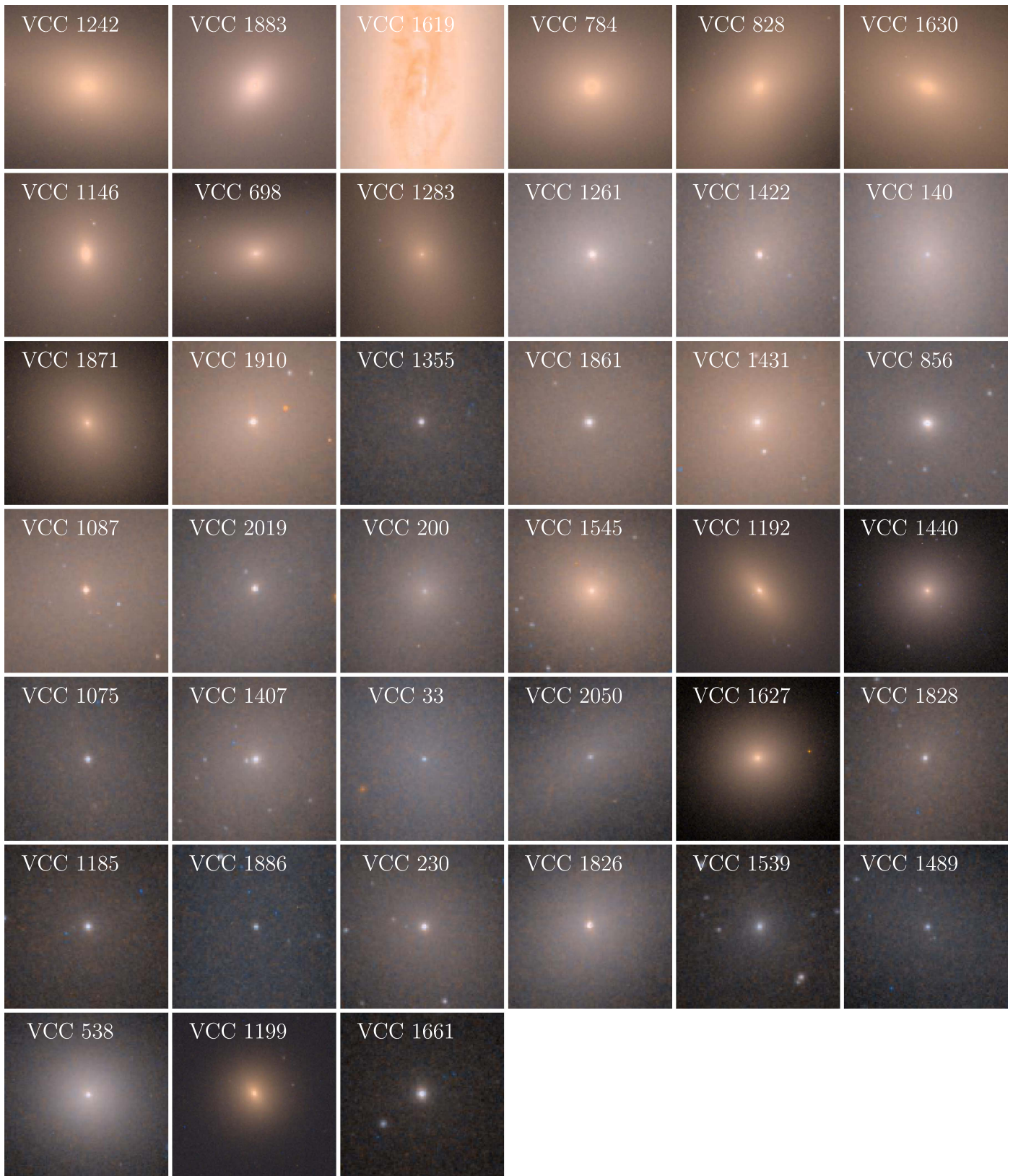
Figure 5. *HST* color images focusing on the central $20'' \times 20''$ (1.6×1.6 kpc) region of each program galaxy, sorted by decreasing F475W luminosity. In all images, north is up and east is to the left.

(made with two Sérsic components) to the 2D method (which may include as many components as needed). However, despite the fairly large scatter of 0.2–0.5 mag, we see no evidence of systematic offsets among the various measurement methods. The good overall agreement between the space- and ground-based 2D magnitudes is especially notable: the nuclei are unresolved in the CFHT imaging, but we are nevertheless able to measure consistent total magnitudes.

Table 3
Summary of Spectroscopic Observations

VCC	Telescope	Instrument	Grating	Dimensions (arcsec)	Θ (deg)	λ Range (Å)	Date (yyyy mm dd)	Exposure Time (sec)
(1)	(2)	(3)	(4)	(5)	(6)	(7)	(8)	(9)
33	Gemini-S	GMOS-IFU	g' filter + B600	$7'' \times 5''$	115.0	3980–5520	2009 Feb 22	4400
33	Keck II	ESI	echelle	$1'' \times 20''$	29.7	4020–7200	2003 Feb 26	1800
200	Keck II	ESI	echelle	$1'' \times 20''$	165.0	4020–7200	2004 Mar 17	1800
230	Keck II	ESI	echelle	$1'' \times 20''$	27.4	4020–7200	2003 Feb 27	2400
538	Keck II	ESI	echelle	$1'' \times 20''$	60.6	4020–7200	2003 Feb 26	2100
1075	Keck II	DEIMOS	600ZD	$0\rlap{.}''8 \times 7\rlap{.}''2$	−1.9	4800–9500	2012 Apr 23	4500
1075	Keck II	ESI	echelle	$0\rlap{.}''75 \times 20''$	45.0	4020–7200	2000 May 01	1200
1185	Gemini-S	GMOS-IFU	g' filter + B600	$7'' \times 5''$	77.0	3980–5520	2009 Feb 25	8400
1185	Keck II	ESI	echelle	$1'' \times 20''$	28.2	4020–7200	2003 Feb 26	2700
1192	Keck II	ESI	echelle	$1'' \times 20''$	37.6	4020–7200	2003 Feb 26	1800
1199	Keck II	ESI	echelle	$1'' \times 20''$	45.0	4020–7200	2003 Feb 26	2100
1355	Gemini-S	GMOS-IFU	g' filter + B600	$7'' \times 5''$	127.0	3980–5520	2009 Mar 5	8400
1407	Keck II	DEIMOS	600ZD	$0\rlap{.}''8 \times 4\rlap{.}''39$	−173.6	4800–9500	2012 Apr 22	3730
1407	Keck II	ESI	echelle	$0\rlap{.}''75 \times 20''$	68.0	4020–7200	2000 May 01	1800
1440	Keck II	ESI	echelle	$1'' \times 20''$	28.9	4020–7200	2003 Feb 26	2100
1489	Keck II	ESI	echelle	$1'' \times 20''$	60.5	4020–7200	2003 Feb 27	3600
1539	Gemini-S	GMOS-IFU	g' filter + B600	$7'' \times 5''$	345.0	3980–5520	2009 Mar 2	8800
1539	Keck II	DEIMOS	600ZD	$0\rlap{.}''8 \times 4\rlap{.}''06$	119.2	4800–9500	2012 Apr 21	4800
1539	Keck II	ESI	echelle	$1'' \times 20''$	46.0	4020–7200	2004 Mar 17	2100
1545	Gemini-S	GMOS-IFU	g' filter + B600	$7'' \times 5''$	335.0	3980–5520	2008 Apr 9	3600
1545	Keck II	DEIMOS	600ZD	$0\rlap{.}''8 \times 5\rlap{.}''66$	−20.0	4800–9500	2012 Apr 21	3600
1545	Keck II	ESI	echelle	$1'' \times 20''$	67.8	4020–7200	2003 Feb 27	2400
1627	Keck II	ESI	echelle	$1'' \times 20''$	93.6	4020–7200	2003 Feb 26	2100
1826	Keck II	ESI	echelle	$1'' \times 20''$	131.2	4020–7200	2003 Feb 26	2100
1828	Keck II	DEIMOS	600ZD	$0\rlap{.}''8 \times 6\rlap{.}''45$	−50.7	4800–9500	2012 Apr 23	4499
1828	Keck II	ESI	echelle	$0\rlap{.}''75 \times 20''$	75.0	4020–7200	2000 Apr 30	1800
1861	Keck II	DEIMOS	600ZD	$0\rlap{.}''8 \times 3\rlap{.}''86$	14.9	4800–9500	2012 Apr 22	3599
1871	Keck II	DEIMOS	600ZD	$0\rlap{.}''8 \times 4\rlap{.}''62$	14.9	4800–9500	2012 Apr 22	3599
2050	Keck II	ESI	echelle	$1'' \times 20''$	127.0	4020–7200	2003 Feb 26	2400

Note. Key to columns: (1) VCC identification number, (2) telescope, (3) spectrograph, (4) grating, (5) slit or IFU dimensions, (6) position angle, Θ, of the slit or major axis of the IFU, (7) wavelength range, (8) date of observation, and (9) total exposure time. For DEIMOS, slit lengths vary from galaxy to galaxy, with values in the range $\sim 4''$–$8''$.
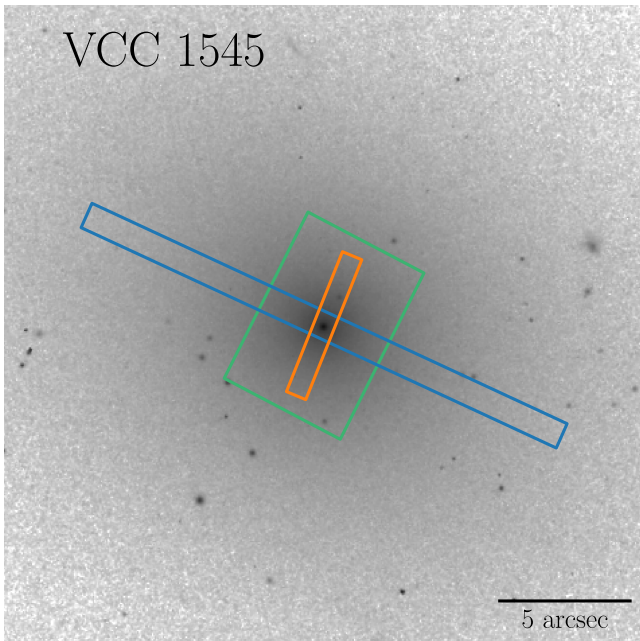

Figure 6. NGVS g-band image for VCC 1545 with the location of the Keck/ESI and Keck/DEIMOS slits shown in blue and red, respectively. The green rectangle indicates the location of the Gemini/GMOS-IFU.

3.4. Adopted Errors

The uncertainties provided by GALFIT are purely statistical and do not account for systematic effects such as the deviation of real galaxies from parametric models. As a result, the errors on GALFIT parameters are unrealistically small and not well determined (Häussler et al. 2007; Lange et al. 2016), so we do not apply these errors to our results. Instead, we estimate the errors based on the comparisons in Section 3.3. Our largest source of error for the nuclei is almost certainly due to the modeling process, as even subtle adjustments to the overall galaxy model may affect the distribution of light in its center. As a result, the nucleus parameters can vary significantly. In addition, with only a few pixels in each image providing information on the nucleus, the χ^2 values calculated by GALFIT are dominated by the quality of the fit of the galaxy components, so determining the best-fit nucleus model can prove challenging. Comparing the results from multiple fitting methods can help quantify the uncertainties in our component magnitudes.

Magnitude differences in the g and z bands appear similar, so we do not expect a strong wavelength dependence on our estimated errors. In fact, the errors should be quite correlated, as all structural parameters have been held fixed at those measured from the F475W images. For the u^*griz, K_s, F475W, F850LP, and F160W images, we adopt errors based on the
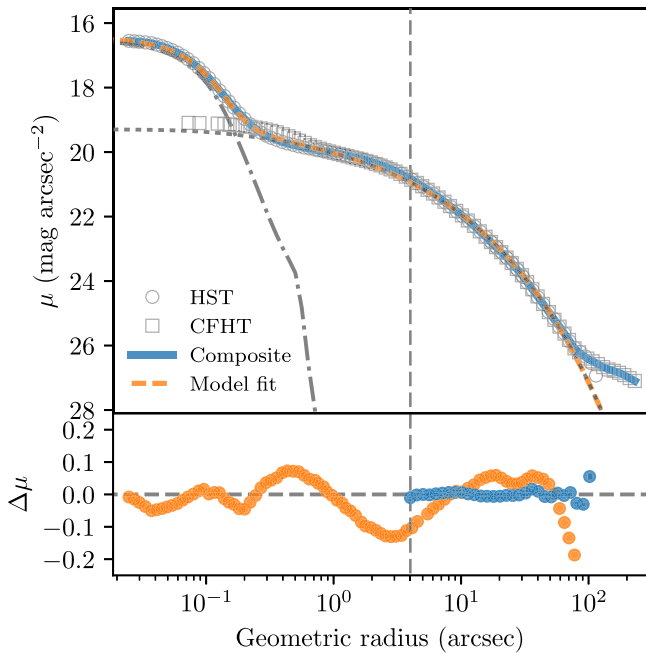
Figure 7. (Top panel) Matched *HST*/ACS (gray circles) and CFHT (gray squares) *g*-band surface brightness profiles for VCC 1422. The final composite profile is plotted in blue. The vertical dashed line indicates the inner boundary of the region used to match the space- and ground-based profiles. The dashed orange line shows a fit to the profile using two Sérsic components; the nucleus component is shown by the dotted–dashed gray curve, and the galaxy component by the dotted gray curve. (Bottom panel) Blue points show the residuals between the *HST* and CFHT profiles in the region used to match the profiles. Orange points show the residuals between the composite profile and the best-fit model. Error bars are smaller than the data points.

typical scatter in the bottom-left and -right panels of Figure 9 at each object's *g* magnitude. However, other factors can contribute to the error budget in the case of WFPC2 imaging, e.g., the low S/N and the limited field of view. In these images, we estimate errors directly from the annuli on the images. We treat any signal outside 20 pixels of the nucleus to be noise that dominates the uncertainty on the nucleus measurement. We estimate this uncertainty from an annulus 5 pixels wide and with an inner radius of 20 pixels, centered on the nucleus.

4. Spectroscopic Analysis

The spectroscopic observations for our target nuclei are summarized in Table 3. For our spectroscopic analysis, we focus entirely on the nuclei spectra because coverage of the galaxy is usually quite limited. For all three data sets (GMOS, ESI, and DEIMOS), we have employed an analysis that is as homogeneous as possible in order to minimize any differences arising from different techniques.

4.1. Data Reduction and Calibration

Full details on the reduction of the GMOS spectra are given in Liu et al. (2016). In brief, cosmic-rays were removed from the spectra before reducing them using the standard GMOS-IFU pipeline in IRAF, which performs bias subtraction, dark correction, flat-fielding, sky subtraction, and wavelength calibration. The spectra were then continuum-normalized and stacked. For each galaxy, the galaxy light was modeled as a Sérsic profile using the signal outside one FWHM of the galaxy

center. This profile was then extrapolated into the central region and subtracted to isolate the nucleus spectrum.

The ESI spectra were reduced using the MAKEE pipeline (Barlow & Sargent 1997). MAKEE is designed to extract isolated and unresolved sources, subtract a sky spectrum from the source, and perform wavelength calibrations using a sixth-order polynomial fit to each echelle order. While the nuclei are unresolved, they clearly are not isolated. Therefore, MAKEE was adapted to treat the adjacent galaxy spectrum as the "sky" component during the sky removal step of the pipeline. As before, the nuclei spectra were continuum-normalized and then shifted to rest-frame wavelengths.

The spec2D pipeline was used on the DEIMOS spectra to reduce 1D and 2D spectra corrected for flat-fielding, sky subtraction, cosmic-ray removal, and wavelength calibration. The nucleus light in each spectrum was extracted from the galaxy light by collapsing the 2D spectrum in the wavelength direction and fitting a Gaussian distribution to the resulting light profile. The width of this Gaussian defines an extraction window. Each pixel within this window is weighted by the value of the Gaussian distribution at that position before being added to the final 1D spectrum. Complete details of this reduction process are provided in Toloba et al. (2016). Once again, the nuclei spectra were then continuum-normalized and shifted to rest-frame wavelengths. As an illustration of the data quality, the final, wavelength-calibrated, continuum-normalized spectra for the nucleus of VCC 1545 are shown in Figure 10.

4.2. Line Index Measurements

Line indices were measured using the IDL script Lick-EW, provided as part of the EZ-AGES code package (Schiavon 2007; Graves & Schiavon 2008). Lick-EW measures equivalent widths on the Lick system by broadening the input spectra to Lick/IDS resolution and following the method described in Worthey et al. (1994). For this sample, we omit corrections for the velocity dispersion, as the low dispersions ($\sim$50 km s^{-1}) for dwarf early-type galaxies do not significantly affect the line widths (Kuntschner 2004). While Lick-EW will measure every available Lick index, we selected only the H$_\beta$, Mg*b*, Fe5270, and Fe5335 lines to estimate the ages, metallicities, and α-element abundances due to their strong features and presence in the wavelength coverage of all three data sets. The measured Lick indices for each nucleus are listed in Table 6. The tabulated values are the mean values of the measurements from each data set when multiple observations are available.

To investigate the robustness of our line index measurements, we compare results from the three spectroscopic data sets for all nuclei that appear in more than one data set. These comparisons are shown in Figure 11 for the H$_\beta$, Mg*b*, Fe5270, and Fe5335 indices. There is generally very good agreement among the index measurements, particularly for Fe5270. The H$_\beta$ agreement for DEIMOS data is somewhat poorer for two objects; however, we note that the H$_\beta$ feature is at the extreme blue end of the DEIMOS wavelength range where the detector's efficiency drops quickly, leading to low S/N. Overall, the agreement among data sets suggests that our line index measurements are reliable.
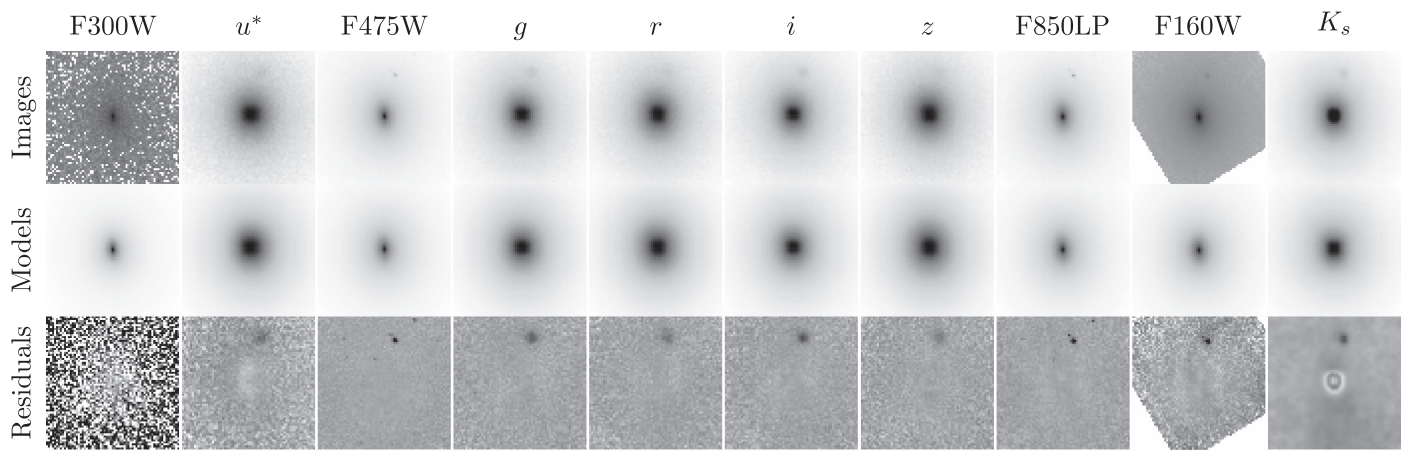
a) VCC 1146.
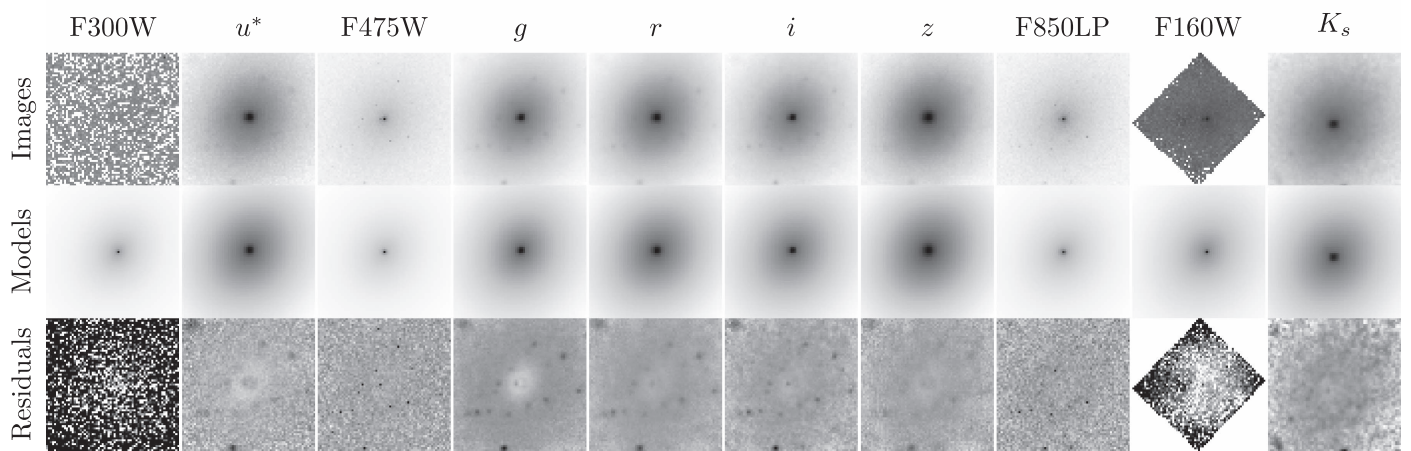
b) VCC 1407.
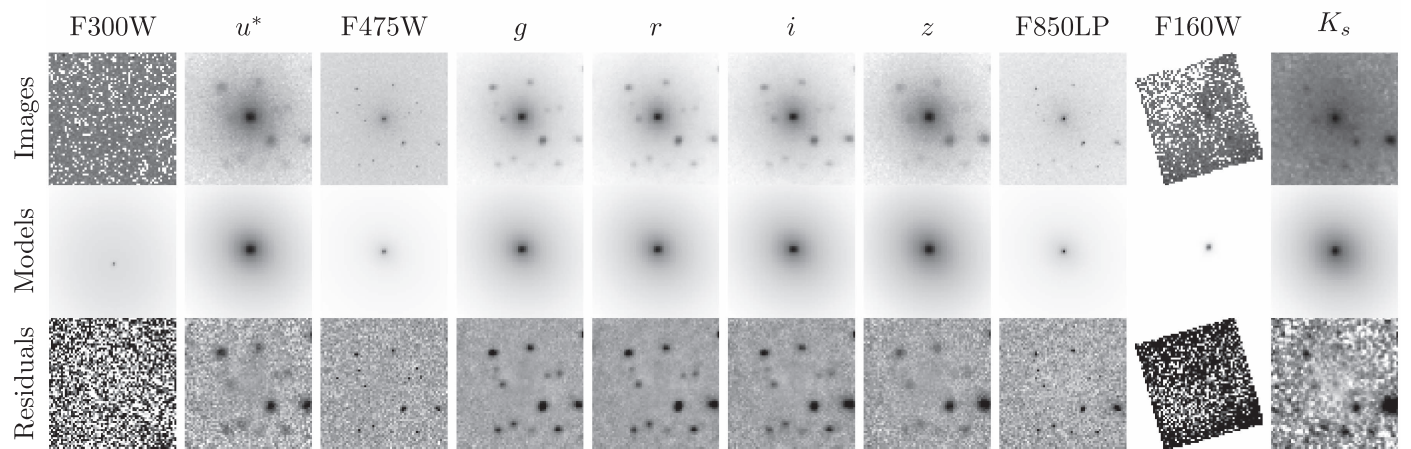
c) VCC 1539.

Figure 8. Final images, best-fit GALFIT models, and model residuals for three of our program galaxies: (a) VCC 1146, (b) VCC 1407, and (c) VCC 1539.

5. Results

5.1. Nucleus and Galaxy Colors

Many studies have noted that nuclei are typically bluer than their hosts in optical colors (e.g., Lotz et al. 2004; Côté et al. 2006; Turner et al. 2012). This is consistent with our findings here. In Figure 12, we present (F475W − F850LP)

colors, as well as (F300W − g) and (z− F160W) colors. We confirm that nuclei are bluer than their hosts in optical colors. This trend does not persist in infrared colors, with no clear color offsets between nuclei and their host galaxies. Unfortunately, given the uncertainties in our UV data, it is difficult to draw any strong conclusions about how nuclei compare to their hosts' UV colors. If the nuclei are truly bluer, this could be indicative of

Table 4
Photometric Measurements for Program Nuclei

VCC (1)	F300W (AB mag) (2)	u^* (AB mag) (3)	F475W (AB mag) (4)	g (AB mag) (5)	r (AB mag) (6)	i (AB mag) (7)	z (AB mag) (8)	F850LP (AB mag) (9)	F160W (AB mag) (10)	K_s (AB mag) (11)
33	25.79 ± 0.30	23.43 ± 0.37	22.20 ± 0.37	22.27 ± 0.37	...	21.45 ± 0.37	22.06 ± 0.37	21.34 ± 0.37	21.04 ± 0.37	...
140	24.49 ± 0.30	23.72 ± 0.37	22.20 ± 0.37	21.87 ± 0.37	...	21.27 ± 0.37	21.61 ± 0.37	21.27 ± 0.37	20.53 ± 0.37	...
200	22.86 ± 0.30[a]	23.20 ± 0.35[a]	22.97 ± 0.35	23.18 ± 0.35	...	21.29 ± 0.35	21.12 ± 0.35	21.75 ± 0.35	20.76 ± 0.35	...
230	22.55 ± 0.30	21.31 ± 0.30	20.16 ± 0.30	19.95 ± 0.30	...	19.14 ± 0.30	19.01 ± 0.30	19.13 ± 0.30	19.06 ± 0.30	...
538	23.50 ± 0.30	21.84 ± 0.27	20.84 ± 0.27	20.96 ± 0.27	...	19.80 ± 0.27	19.36 ± 0.27	19.75 ± 0.27	19.09 ± 0.27	...
698	22.43 ± 0.30	21.11 ± 0.29	20.05 ± 0.29	19.27 ± 0.29	...	18.95 ± 0.29	18.68 ± 0.29	18.78 ± 0.29	18.37 ± 0.29	...
784	21.92 ± 0.30	20.59 ± 0.21	18.75 ± 0.21	18.34 ± 0.21	...	17.21 ± 0.21	16.84 ± 0.21	17.26 ± 0.21	16.31 ± 0.21	...
828	21.77 ± 0.30	19.37 ± 0.20	18.54 ± 0.20	18.45 ± 0.20	...	17.10 ± 0.20	17.28 ± 0.20	16.96 ± 0.20	16.22 ± 0.20	...
856	22.02 ± 0.30	20.57 ± 0.32	19.56 ± 0.32	19.38 ± 0.32	...	18.51 ± 0.32	18.37 ± 0.32	18.49 ± 0.32	17.90 ± 0.32	...
1075	23.54 ± 0.30	22.16 ± 0.27	21.08 ± 0.27	21.13 ± 0.27	...	20.24 ± 0.27	20.20 ± 0.27	20.19 ± 0.27	19.76 ± 0.27	...
1087	23.23 ± 0.30	22.12 ± 0.30	20.16 ± 0.30	17.52 ± 0.30[a]	17.32 ± 0.30[a]	16.77 ± 0.30[a]	16.00 ± 0.30[a]	18.93 ± 0.30	18.30 ± 0.30	18.17 ± 0.30
1146	19.32 ± 0.30	17.49 ± 0.12	16.60 ± 0.12	16.58 ± 0.12	16.05 ± 0.12	15.42 ± 0.12	15.37 ± 0.12	15.10 ± 0.12	14.24 ± 0.12	15.67 ± 0.12
1185	...	21.88 ± 0.28	20.76 ± 0.28	20.67 ± 0.28	20.12 ± 0.28	19.81 ± 0.28	19.70 ± 0.28	19.80 ± 0.28	19.42 ± 0.28	19.43 ± 0.28
1192	21.12 ± 0.30	19.70 ± 0.20	18.47 ± 0.20	18.44 ± 0.20	17.73 ± 0.20	17.61 ± 0.20	17.14 ± 0.20	17.23 ± 0.20	16.43 ± 0.20	...
1199	22.41 ± 0.30	20.63 ± 0.32	19.43 ± 0.32	19.08 ± 0.32	18.35 ± 0.32	18.25 ± 0.32	17.82 ± 0.32	18.01 ± 0.32	17.09 ± 0.32	...
1242	20.32 ± 0.30	19.12 ± 0.11	17.61 ± 0.11	17.37 ± 0.11	16.63 ± 0.11	16.25 ± 0.11	16.03 ± 0.11	16.09 ± 0.11	15.33 ± 0.11	...
1261	22.55 ± 0.30	21.39 ± 0.29	19.87 ± 0.29	20.33 ± 0.29	...	18.96 ± 0.29	18.59 ± 0.29	18.69 ± 0.29	18.69 ± 0.29	...
1283	22.75 ± 0.30	20.88 ± 0.29	19.94 ± 0.29	19.50 ± 0.29	18.89 ± 0.29	18.61 ± 0.29	18.32 ± 0.29	18.47 ± 0.29	17.50 ± 0.29	...
1355	23.48 ± 0.30	22.39 ± 0.26	21.10 ± 0.26	21.23 ± 0.26	20.67 ± 0.26	20.20 ± 0.26	20.06 ± 0.26	20.12 ± 0.26	19.68 ± 0.26	...
1407	23.36 ± 0.30	21.48 ± 0.29	20.76 ± 0.29	20.37 ± 0.29	19.94 ± 0.29	19.67 ± 0.29	19.38 ± 0.29	19.78 ± 0.29	19.31 ± 0.29	18.83 ± 0.29
1422	22.86 ± 0.30	21.31 ± 0.29	20.09 ± 0.29	19.99 ± 0.29	...	18.98 ± 0.29	18.76 ± 0.29	18.87 ± 0.29	18.32 ± 0.29	...
1431	22.16 ± 0.30	21.05 ± 0.30	19.89 ± 0.30	19.62 ± 0.30	...	18.83 ± 0.30	18.61 ± 0.30	18.79 ± 0.30	18.32 ± 0.30	...
1440	22.75 ± 0.30	21.09 ± 0.31	20.24 ± 0.31	19.80 ± 0.31	...	19.39 ± 0.31	18.36 ± 0.31	19.01 ± 0.31	18.54 ± 0.31	...
1489	24.38 ± 0.30	23.51 ± 0.38	22.41 ± 0.38	22.29 ± 0.38	...	21.63 ± 0.38	21.66 ± 0.38	21.62 ± 0.38	21.25 ± 0.38	...
1539	23.67 ± 0.30[a]	22.02 ± 0.27	21.20 ± 0.27	21.01 ± 0.27	20.53 ± 0.27	20.34 ± 0.27	20.36 ± 0.27	20.38 ± 0.27	19.74 ± 0.27	20.21 ± 0.27
1545	24.22 ± 0.30	22.50 ± 0.28	21.81 ± 0.28	21.29 ± 0.28	20.20 ± 0.28	20.28 ± 0.28	20.10 ± 0.28	20.61 ± 0.28	21.36 ± 0.28	19.05 ± 0.28
1619	23.30 ± 0.30	21.58 ± 0.19	18.99 ± 0.19	19.06 ± 0.19	...	17.86 ± 0.19	17.35 ± 0.19	17.78 ± 0.19	16.33 ± 0.19	...
1627	...	21.37 ± 0.30	20.20 ± 0.30	19.56 ± 0.30	...	20.03 ± 0.30	18.26 ± 0.30	18.81 ± 0.30	...	...
1630	21.80 ± 0.30	19.93 ± 0.20	18.67 ± 0.20	18.45 ± 0.20	...	17.35 ± 0.20	16.65 ± 0.20	17.04 ± 0.20	16.04 ± 0.20	...
1661	24.01 ± 0.30	22.12 ± 0.27	20.87 ± 0.27	20.23 ± 0.27	...	19.92 ± 0.27	19.36 ± 0.27	21.27 ± 0.27	19.28 ± 0.27	...
1826	22.69 ± 0.30	21.13 ± 0.29	20.05 ± 0.29	19.97 ± 0.29	...	18.99 ± 0.29	18.84 ± 0.29	18.91 ± 0.29	18.67 ± 0.29	...
1828	23.59 ± 0.30	22.81 ± 0.25	21.49 ± 0.25	21.44 ± 0.25	...	20.54 ± 0.25	20.39 ± 0.25	20.48 ± 0.25	20.17 ± 0.25	...
1861	21.95 ± 0.30	21.09 ± 0.29	20.01 ± 0.29	19.84 ± 0.29	...	19.02 ± 0.29	18.93 ± 0.29	18.92 ± 0.29	18.43 ± 0.29	...
1871	21.86 ± 0.30	20.32 ± 0.19	19.04 ± 0.19	19.31 ± 0.19	...	18.42 ± 0.19	17.58 ± 0.19	17.77 ± 0.19	17.15 ± 0.19	...
1883	20.03 ± 0.30	18.30 ± 0.13	17.61 ± 0.13	17.74 ± 0.13	...	29.30 ± 0.13[a]	16.09 ± 0.13	17.42 ± 0.13	15.53 ± 0.13	...
1886	24.27 ± 0.30[a]	23.06 ± 0.37	22.11 ± 0.37	22.02 ± 0.37	...	21.24 ± 0.37	21.30 ± 0.37	21.20 ± 0.37	21.10 ± 0.37	...
1910	22.36 ± 0.30	20.84 ± 0.31	19.74 ± 0.31	19.62 ± 0.31	19.01 ± 0.31	18.69 ± 0.31	18.53 ± 0.31	18.62 ± 0.31	18.30 ± 0.31	...
2019	23.01 ± 0.30	21.45 ± 0.32	20.27 ± 0.32	20.25 ± 0.32	...	19.27 ± 0.32	19.07 ± 0.32	19.18 ± 0.32	18.61 ± 0.32	...
2050	21.92 ± 0.30[a]	29.35 ± 0.37[a]	22.47 ± 0.37	23.08 ± 0.37	...	21.46 ± 0.37	22.11 ± 0.37	21.39 ± 0.37	20.56 ± 0.37	...

Note. Magnitudes have not been corrected for Milky Way foreground extinction.
[a] Magnitude excluded from analysis due to image artifacts, failure of GALFIT to converge on a model fit, or, in F300W, a non-detection.

Table 5
Photometric Measurements for Program Galaxies

VCC	F300W (AB mag)	u^* (AB mag)	F475W (AB mag)	g (AB mag)	r (AB mag)	i (AB mag)	z (AB mag)	F850LP (AB mag)	F160W (AB mag)	K_s (AB mag)
(1)	(2)	(3)	(4)	(5)	(6)	(7)	(8)	(9)	(10)	(11)
33	16.76 ± 0.30	16.05 ± 0.02	14.98 ± 0.02	14.90 ± 0.02	...	14.08 ± 0.02	13.83 ± 0.02	13.91 ± 0.02	13.50 ± 0.02	...
140	16.68 ± 0.30	15.26 ± 0.03	14.01 ± 0.03	13.95 ± 0.03	...	13.05 ± 0.03	12.83 ± 0.03	12.83 ± 0.03	12.52 ± 0.03	...
200	15.96 ± 0.30[a]	15.87 ± 0.02	14.69 ± 0.02	14.59 ± 0.02	...	13.70 ± 0.02	13.46 ± 0.02	13.50 ± 0.02	13.23 ± 0.02	...
230	17.41 ± 0.30	16.59 ± 0.02	15.47 ± 0.02	15.39 ± 0.02	...	14.50 ± 0.02	14.27 ± 0.02	14.32 ± 0.02	14.09 ± 0.02	...
538	18.89 ± 0.30	16.97 ± 0.02	15.87 ± 0.02	15.81 ± 0.02	...	14.91 ± 0.02	14.75 ± 0.02	14.74 ± 0.02	14.55 ± 0.02	...
698	15.51 ± 0.30	14.16 ± 0.01	12.98 ± 0.01	12.85 ± 0.01	...	11.91 ± 0.01	11.64 ± 0.01	11.65 ± 0.01	10.83 ± 0.01	...
784	15.81 ± 0.30	13.45 ± 0.10	12.23 ± 0.10	12.12 ± 0.10	...	11.12 ± 0.10	10.83 ± 0.10	10.83 ± 0.10	10.17 ± 0.10	...
828	15.68 ± 0.30	13.24 ± 0.10	12.36 ± 0.10	12.15 ± 0.10	11.76 ± 0.10	11.12 ± 0.10	10.78 ± 0.10	10.92 ± 0.10	10.25 ± 0.10	...
856	16.22 ± 0.30	15.38 ± 0.03	14.28 ± 0.03	14.19 ± 0.03	...	13.30 ± 0.03	13.09 ± 0.03	13.08 ± 0.03	12.85 ± 0.03	...
1075	17.00 ± 0.30	16.04 ± 0.02	14.87 ± 0.02	14.83 ± 0.02	...	13.92 ± 0.02	13.67 ± 0.02	13.68 ± 0.02	13.44 ± 0.02	...
1087	15.69 ± 0.30	15.46 ± 0.02	14.41 ± 0.02	14.11 ± 0.02[a]	13.41 ± 0.02[a]	13.18 ± 0.02[a]	13.05 ± 0.02[a]	13.06 ± 0.02	12.57 ± 0.02	12.95 ± 0.02
1146	15.18 ± 0.30	13.60 ± 0.04	12.48 ± 0.04	12.36 ± 0.04	11.68 ± 0.04	11.35 ± 0.04	11.16 ± 0.04	11.14 ± 0.04	10.56 ± 0.04	10.82 ± 0.04
1185	...	16.31 ± 0.03	15.20 ± 0.03	15.12 ± 0.03	14.56 ± 0.03	14.26 ± 0.03	13.97 ± 0.03	14.02 ± 0.03	13.30 ± 0.03	14.43 ± 0.03
1192	17.60 ± 0.30	16.18 ± 0.02	14.76 ± 0.02	14.66 ± 0.02	14.00 ± 0.02	13.61 ± 0.02	13.34 ± 0.02	13.29 ± 0.02	12.57 ± 0.02	...
1199	18.97 ± 0.30	17.68 ± 0.01	16.13 ± 0.01	16.02 ± 0.01	15.31 ± 0.01	14.90 ± 0.01	14.64 ± 0.01	14.57 ± 0.01	13.91 ± 0.01	...
1242	15.55 ± 0.30	13.33 ± 0.11	12.11 ± 0.11	12.01 ± 0.11	11.35 ± 0.11	10.95 ± 0.11	10.73 ± 0.11	10.73 ± 0.11	10.14 ± 0.11	...
1261	15.64 ± 0.30	14.50 ± 0.02	13.42 ± 0.02	13.31 ± 0.02	...	12.45 ± 0.02	12.23 ± 0.02	12.22 ± 0.02	11.75 ± 0.02	...
1283	14.30 ± 0.30	14.24 ± 0.01	13.05 ± 0.01	12.92 ± 0.01	12.25 ± 0.01	11.92 ± 0.01	11.63 ± 0.01	11.65 ± 0.01	10.81 ± 0.01	...
1355	16.84 ± 0.30	15.27 ± 0.03	14.17 ± 0.03	14.09 ± 0.03	13.53 ± 0.03	13.22 ± 0.03	13.01 ± 0.03	13.00 ± 0.03	12.73 ± 0.03	...
1407	16.62 ± 0.30	15.97 ± 0.02	14.94 ± 0.02	14.82 ± 0.02	14.26 ± 0.02	13.91 ± 0.02	13.70 ± 0.02	13.73 ± 0.02	13.14 ± 0.02	13.65 ± 0.02
1422	15.79 ± 0.30	14.48 ± 0.02	13.43 ± 0.02	13.34 ± 0.02	...	12.45 ± 0.02	12.17 ± 0.02	12.24 ± 0.02	11.73 ± 0.02	...
1431	17.06 ± 0.30	15.49 ± 0.03	14.27 ± 0.03	14.19 ± 0.03	13.53 ± 0.03	13.17 ± 0.03	12.92 ± 0.03	12.91 ± 0.03	12.50 ± 0.03	...
1440	17.96 ± 0.30	15.75 ± 0.02	14.78 ± 0.02	14.67 ± 0.02	...	13.74 ± 0.02	13.53 ± 0.02	13.53 ± 0.02	12.91 ± 0.02	...
1489	17.45 ± 0.30	16.84 ± 0.02	15.80 ± 0.02	15.76 ± 0.02	15.22 ± 0.02	14.94 ± 0.02	14.73 ± 0.02	14.76 ± 0.02	14.65 ± 0.02	...
1539	14.68 ± 0.30[a]	16.81 ± 0.02	15.68 ± 0.02	15.62 ± 0.02	15.07 ± 0.02	14.74 ± 0.02	14.56 ± 0.02	14.47 ± 0.02	16.09 ± 0.02	14.52 ± 0.02
1545	18.30 ± 0.30	15.93 ± 0.02	14.82 ± 0.02	14.69 ± 0.02	14.09 ± 0.02	13.75 ± 0.02	13.56 ± 0.02	13.55 ± 0.02	...	13.53 ± 0.02
1619	15.14 ± 0.30	13.36 ± 0.10	12.10 ± 0.10	12.03 ± 0.10	...	11.02 ± 0.10	10.69 ± 0.10	10.71 ± 0.10	10.55 ± 0.10[a]	...
1627	...	16.33 ± 0.02	15.04 ± 0.02	14.94 ± 0.02	...	13.90 ± 0.02	13.65 ± 0.02	13.63 ± 0.02	...	...
1630	15.24 ± 0.30	13.77 ± 0.10	12.41 ± 0.10	12.30 ± 0.10	...	11.27 ± 0.10	10.91 ± 0.10	10.93 ± 0.10	10.36 ± 0.10	...
1661	17.56 ± 0.30	16.88 ± 0.13	16.78 ± 0.13	15.58 ± 0.13	...	14.62 ± 0.13	14.40 ± 0.13	...	14.90 ± 0.13	...
1826	18.30 ± 0.30	16.74 ± 0.02	15.52 ± 0.02	15.47 ± 0.02	...	14.59 ± 0.02	14.37 ± 0.02	14.38 ± 0.02	14.18 ± 0.02	...
1828	17.65 ± 0.30	16.17 ± 0.02	15.08 ± 0.02	14.99 ± 0.02	...	14.07 ± 0.02	13.83 ± 0.02	13.85 ± 0.02	13.27 ± 0.02	...
1861	16.10 ± 0.30	15.28 ± 0.03	14.17 ± 0.03	14.03 ± 0.03	...	13.09 ± 0.03	12.86 ± 0.03	12.87 ± 0.03	12.76 ± 0.03	...
1871	16.88 ± 0.30	15.41 ± 0.03	14.14 ± 0.03	14.02 ± 0.03	...	12.98 ± 0.03	12.72 ± 0.03	12.73 ± 0.03	12.21 ± 0.03	...
1883	14.53 ± 0.30	12.91 ± 0.10	12.06 ± 0.10	11.68 ± 0.10	...	17.99 ± 0.10[a]	10.71 ± 0.10	10.49 ± 0.10	10.19 ± 0.10	...
1886	15.71 ± 0.30[a]	16.24 ± 0.03	15.26 ± 0.03	15.19 ± 0.03	...	14.40 ± 0.03	14.23 ± 0.03	14.25 ± 0.03	13.51 ± 0.03	...
1910	16.93 ± 0.30	15.32 ± 0.03	14.15 ± 0.03	13.99 ± 0.03	13.35 ± 0.03	13.02 ± 0.03	12.74 ± 0.03	12.78 ± 0.03	12.05 ± 0.03	...
2019	16.43 ± 0.30	15.63 ± 0.02	14.46 ± 0.02	14.42 ± 0.02	...	13.51 ± 0.02	13.30 ± 0.02	13.29 ± 0.02	12.89 ± 0.02	...
2050	17.57 ± 0.30[a]	14.33 ± 0.02	14.95 ± 0.02	14.82 ± 0.02	...	14.01 ± 0.02	13.74 ± 0.02	13.83 ± 0.02	13.71 ± 0.02	...

Note. Magnitudes have not been corrected for Milky Way foreground extinction.
[a] Magnitude excluded from analysis due to image artifacts, failure of GALFIT to converge on a model fit, or, in F300W, a non-detection.
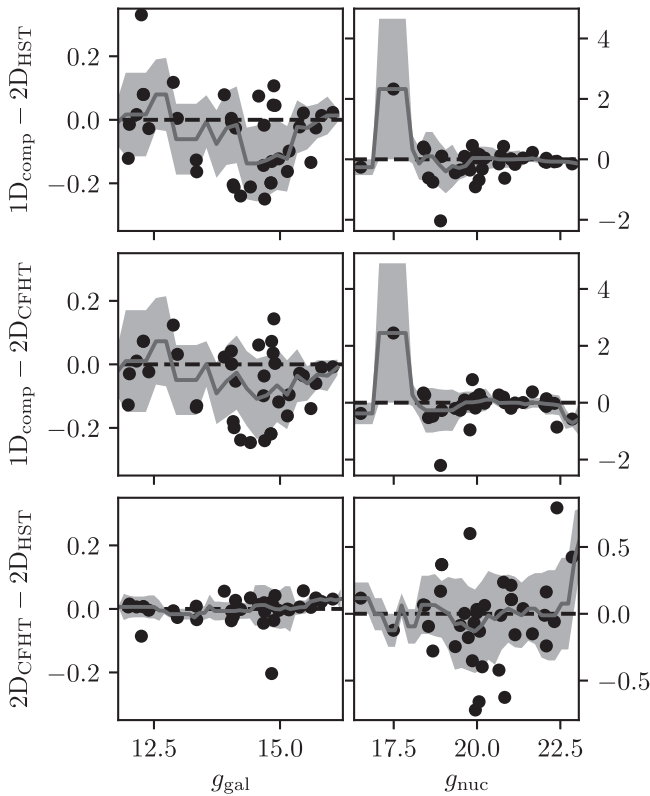
Figure 9. Differences in magnitudes measured, measured with different methods, plotted as a function of magnitude. The left column shows galaxy magnitudes, while the right shows nuclear magnitudes. The top row shows differences between the 1D *HST*+CFHT composite profile and 2D *HST* magnitudes. The middle row compares the 1D *HST*+CFHT composite profile and 2D CFHT magnitudes, while the bottom row compares the 2D CFHT and *HST* magnitudes. In each panel, the gray curve shows the average offset as a function of magnitude, with the shaded region showing the associated 1σ scatter.
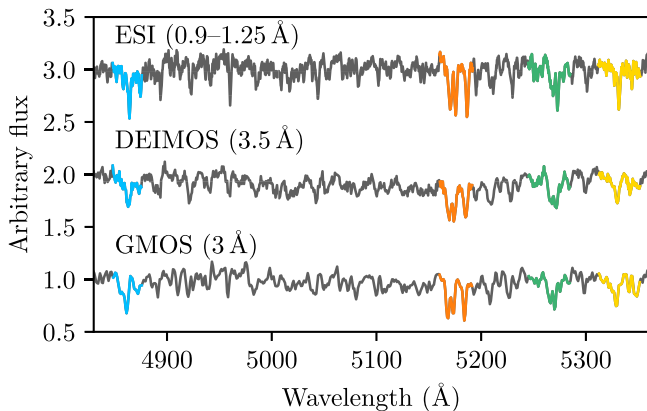
Figure 10. Wavelength-calibrated, continuum-normalized, rest-frame spectra for VCC 1545 obtained using the ESI, DEIMOS, and GMOS instruments. Four indices used to measure ages, metallicities, and α-element abundances have been highlighted: H_β (light blue), Mgb (orange), Fe5270 (green), and Fe5335 (yellow). The values in parentheses after each instrument name indicate the spectral resolution at 5000 Å.

some fraction of the stellar content consisting of a young ($\lesssim 2$ Gyr) population. Alternatively, redder UV colors in the nuclei could be a sign of internal dust extinction. Although dwarf early-type galaxies are not expected to have a *substantial*

dust content, any dust that is present tends to be more concentrated than the stellar content (di Serego Alighieri et al. 2013). In that case, nuclei may be more affected by centrally concentrated galactic dust. Moreover, nuclei may well show larger dust fractions if they have recently formed stars. In this work, we assumed zero internal extinction for both galaxies and nuclei, which may present a bias in the derived population parameters. In the future, high-resolution UV and MIR data could be used to investigate the dust content and extinction in these objects. Further details on the dust content and its effect on the results are included in Section 5.3.

5.2. SED Fitting and Parameter Estimation

The results of Section 3.3 suggest that the 2D image decomposition technique yields the most homogeneous photometry for each nucleus and galaxy. We therefore use these UV, optical, and IR measurements as the basis for our SED analysis for all objects.

The overarching goal of our SED analysis is to estimate the masses, ages, and metallicities for each nucleus and its galaxy in a consistent way. To do this, we adopt a Markov Chain Monte Carlo (MCMC) approach. MCMC methods are designed to select N samples from the parameter space in a random walk such that as N increases, the sample distribution approaches the true probability distribution. We constructed an SED fitting program in Python based on the emcee package (Foreman-Mackey et al. 2013). The emcee algorithm is the affine-invariant MCMC ensemble sampler, which has a few substantial differences from the more common Metropolis–Hastings algorithm. The Metropolis–Hastings method relies on a single Markov chain to probe the parameter space, and each time the chain attempts to jump to a new region of parameter space, the move is rejected or accepted based only on the likelihood of the proposed position relative to the likelihood of the current position. In contrast, the affine-invariant method uses multiple *walkers* to probe the parameter space, and the proposed jump for each walker is based on the likelihood of that walker's current position as well as the likelihood of one other randomly selected walker's position. As a result, this method should require fewer tuning parameters and be less sensitive to the initial choices of model parameters.

Predicted stellar population properties can vary substantially based on the models used for comparison in the SED fit (Kannappan & Gawiser 2007; Muzzin et al. 2009). When creating a model population, a number of components must be included, and the choices for these ingredients will naturally affect the resulting population. Such components include, for example, an IMF, spectral libraries, stellar isochrones, and the treatment of post-main sequence phases. The last point is especially important for poorly understood evolutionary phases such as the thermally pulsating asymptotic giant branch (TP-AGB). Depending on how TP-AGB stars are modeled, the population spectrum for ages $0.3 \leqslant t \leqslant 2$ Gyr can change dramatically (Maraston 2005). A thorough overview of the uncertainties among models is given in Conroy & Gunn (2010).

To minimize the effect of model-specific features, we fit our data to an assortment of model SEDs and look for any results that remain consistent regardless of the adopted model. We also have chosen similar or matching IMFs whenever possible, i.e., a Chabrier or Kroupa IMF, both of which are appropriate for

Table 6
Mean Measured Lick Indices

VCC	Instruments	H$_\beta$ (Å)	Mgb (Å)	Fe5270 (Å)	Fe5335 (Å)
(1)	(2)	(3)	(4)	(5)	(6)
33	ESI,GMOS	3.13 ± 0.41	1.38 ± 0.42	1.91 ± 0.47	1.12 ± 0.57
200	ESI	2.09 ± 0.90	2.27 ± 0.70	2.38 ± 1.45	2.12 ± 0.81
230	ESI	2.30 ± 0.61	1.56 ± 0.79	1.91 ± 0.59	1.58 ± 0.86
538	ESI	2.22 ± 0.73	2.09 ± 0.82	2.19 ± 0.67	2.21 ± 1.03
1075	ESI,DEIMOS	2.26 ± 0.58	1.17 ± 0.48	1.69 ± 0.61	1.52 ± 0.61[a]
1185	ESI,GMOS	2.29 ± 0.42	1.70 ± 0.41	1.96 ± 0.54	1.71 ± 0.77
1192	ESI	1.76 ± 0.71	4.06 ± 0.97	2.75 ± 0.79	2.43 ± 0.97
1199	ESI	1.86 ± 0.83	4.05 ± 0.70	3.12 ± 0.81	3.17 ± 0.77
1355	GMOS	2.81 ± 0.42	1.42 ± 0.48	0.80 ± 0.58	0.63 ± 0.66
1407	ESI,DEIMOS	2.66 ± 0.84	2.04 ± 0.54	1.55 ± 0.63	1.22 ± 1.00
1440	ESI	1.90 ± 0.76	2.63 ± 0.92	2.49 ± 0.62	2.29 ± 0.96
1489	ESI	2.84 ± 0.39	0.71 ± 0.54	1.11 ± 0.85	1.86 ± 0.92
1539	ESI,DEIMOS,GMOS	1.98 ± 0.47	1.76 ± 0.43	1.33 ± 0.55[c]	0.91 ± 0.57
1545	ESI,DEIMOS,GMOS	2.09 ± 0.26	2.81 ± 0.32	2.66 ± 0.44	2.53 ± 0.31
1627	ESI	1.87 ± 0.72	3.24 ± 0.73	2.81 ± 0.86	2.82 ± 0.79
1826	ESI	2.26 ± 0.66	1.96 ± 0.71	2.25 ± 1.11	1.55 ± 1.15
1828	ESI,DEIMOS	2.32 ± 0.49[b]	1.94 ± 0.86	2.47 ± 0.71	1.48 ± 0.60
1861	DEIMOS	2.33 ± 0.83	1.22 ± 0.55	1.79 ± 0.57	1.60 ± 0.63
1871	DEIMOS	1.80 ± 0.45	3.61 ± 0.20	2.92 ± 0.21	2.73 ± 0.24
2050	ESI	2.33 ± 0.76	1.45 ± 1.06	2.37 ± 1.23	1.23 ± 0.97

Notes.
[a] ESI data excluded from the measurement due to non-detection.
[b] DEIMOS data excluded from the measurement due to a gap in the spectrum.
[c] GMOS data excluded from the measurement due to non-detection.
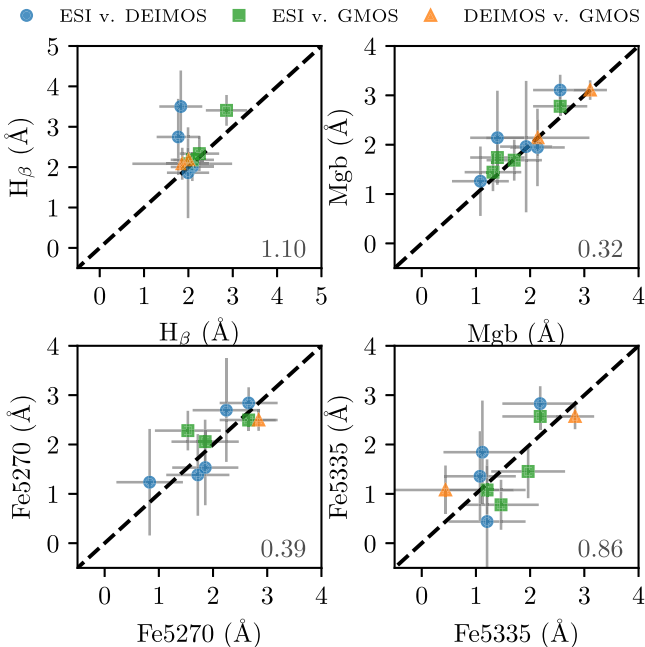
Figure 11. Comparison of Lick index measurements among the ESI, GMOS, and DEIMOS data sets. The blue points show the value measured with ESI data compared to that measured with the DEIMOS data. Similarly, green squares show the ESI values against the GMOS values. In both cases, ESI measurements are plotted along the abscissa. The orange triangles are DEIMOS values compared to GMOS values for the two nuclei (VCC 1539 and VCC 1545) that appear in both data sets. The dashed line in each panel shows the one-to-one relation, while numbers in the bottom-right corner show the rms scatter in angstroms.

dwarf, low-σ early-type galaxies (Cappellari et al. 2012; Mentz et al. 2016). We used SSP spectra from Bruzual & Charlot (2003, hereafter BC03), Fioc & Rocca-Volmerange

(1997, 1999, PÉGASE.2), and Maraston (2005, hereafter M05). We summarize the features of each model set in Table 7.

In all cases, the model SEDs are purely stellar in nature: i.e., we assume zero dust content and no nebular emission. Therefore, only three free parameters are needed: stellar mass $M_\star$, metallicity Z, and age t. We assume a flat prior in the mass range $1 \leqslant M_\star \leqslant 10^{14} \, M_\odot$ and across the full metallicity range of each model set (see Table 7). We also apply flat priors to ages in the range $0 \leqslant t \leqslant 14$ Gyr, eliminating ages older than that of the universe. Model grids were created with 50 metallicity steps and 100 age steps, regularly spaced across the full space of $\log_{10} Z$ and $\log_{10} t$ covered by each model family. To evaluate how well the model reproduces the observed data, we use the log-likelihood equation:

$$\ln \mathcal{L} = -\frac{1}{2} \sum_{i=1}^{N} \left[\ln(2\pi\sigma_{\mathrm{obs},i}^2) + \frac{\left(\frac{M_\star}{m(t,Z)} F_i(t,Z) - F_{\mathrm{obs},i} \right)^2}{\sigma_{\mathrm{obs},i}^2} \right].$$
(4)

Here, $F_{\mathrm{obs},i}$ is the observed flux in each filter, $\sigma_{\mathrm{obs},i}$ is the flux error, $m(t,Z)$ is the stellar mass of the model, and $F_i(t,Z)$ is the model flux in each filter. Because the model SEDs are normalized to one solar mass at $t = 0$, $M_\star/m(t,Z)$, this is effectively a scale factor that is applied to best match the model to the observed flux.

Before fitting each object, we omitted any magnitudes that were obvious outliers based on visual inspection of the SED. These outliers represent cases in which the GALFIT model clearly failed to converge on a reasonable fit, and affected, at most, a single data point for each observed SED. These values were often at least an order of magnitude brighter or fainter
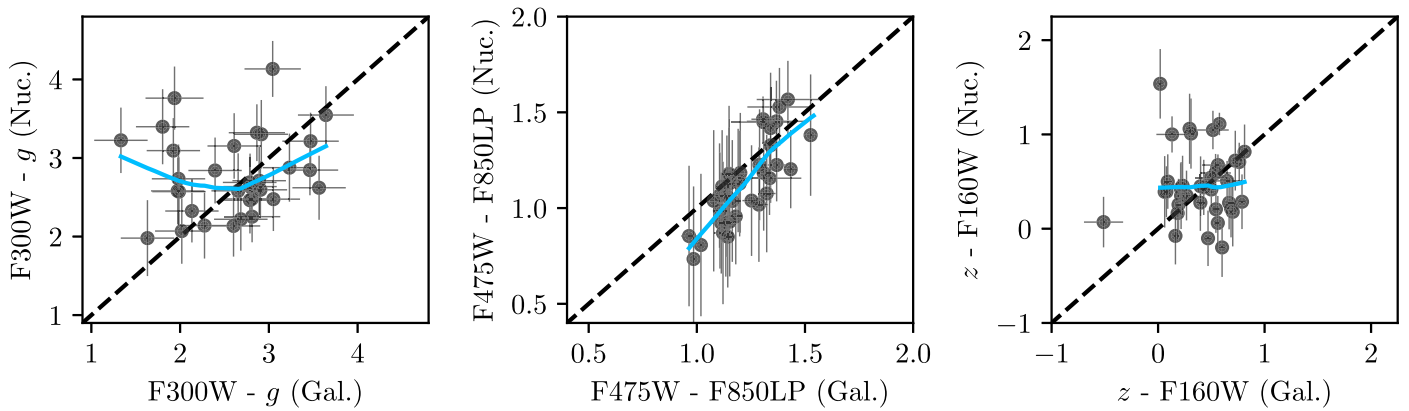
Figure 12. Nuclei UV–optical (left panel), optical (middle panel), and optical–IR (right panel) colors as a function of galaxy color. In each panel, one-to-one lines are shown to guide the eye. The blue lines in each panel are the LOWESS (Cleveland 1979) curves for the data to illustrate the typical color trend for the sample.

than the surrounding measurements and could be confidently excluded.

For each nucleus and galaxy, 500 walkers with 1000 steps through parameter space (after a burn-in period of 500 steps) provided a total of 500,000 samplings to generate posterior probability distributions for each parameter. Figure 13 shows an example of the joint and individual posteriors for the VCC 1422 nucleus and the selected best-fit parameters. We extracted the median of each distribution as the best-fit value and use the 16th and 84th percentiles as the 1σ uncertainties. The best-fit SED using these values is shown in Figure 14, again for the VCC 1422 nucleus. For comparison, we also calculate the χ^2 value for each parameter combination and determine an additional set of best-fit parameters based on χ^2 minimization. This technique is more consistent with previous work, but produces systematically different values from the median best-fit parameters, which are generally older and less metal-rich. We find that the χ^2 value changes very minimally due to the age–metallicity degeneracy, such that the χ^2 value of each set of median parameters is only marginally larger than the minimum χ^2. With this in mind, we adopt the median parameters as our final best-fit parameters, as we believe that the MCMC technique and error estimation better accounts for the degeneracy. The resulting masses, metallicities, and ages estimated using the BC03 models for the nuclei and galaxies are listed in Table 8.

By comparing results from different models, we can explore possible systematic differences among the calculated parameters. A comparison of the stellar population properties for the galaxies and nuclei derived from our three models is shown in Figure 15. The BC03 values are adopted as a baseline on the abscissa, with the M05 or PÉGASE.2 value on the ordinate. There are no strong systematic differences among the derived parameters. All models produce masses and metallicities that are in very good agreement within the uncertainties. The BC03 and PÉGASE.2 results are quite consistent with each other, although the M05 models do tend to predict a different range of ages. While the BC03 and PÉGASE.2 models tend to produce ages between 5 and 12 Gyr, the M05 ages can be as young as 1 Gyr. This is likely an effect of the treatment of the TP-AGB population and other post-main sequence evolutionary stages. The unique fuel consumption model employed by M05 for these stages of stellar evolution means that the contribution of these red stars to the population's total becomes highly significant at ages ∼1–3 Gyr. As a result, the M05 models

can match relatively redder observed colors with younger populations compared to the other models.

5.3. A Note on Dust Effects

Given the potential impact of internal dust on the measured colors and population parameters, we investigated the degree to which dust could alter the estimated stellar population parameters. We did so by carrying out an independent set of SED fits with the addition of a free parameter, $E(B - V)$. The model fluxes were reddened according to the attenuation law in Calzetti et al. (2000). On average, the best-fit $E(B - V)$ for the nuclei is ∼0.3 mag, and ∼0.1 mag for the galaxies. There are, however, large uncertainties on these values, as well as substantial degeneracies with the best-fit ages. The galaxy results appear to be relatively unchanged compared to the dust-free models, with generally only slight decreases (1–2 Gyr) in age after including the reddening parameter. The galaxy metallicities remain roughly the same, around solar values, but lower metallicity objects become even more metal-poor once reddening is included. The nucleus metallicities exhibit a similar change, while the shift in nucleus ages is more dramatic with reddening: i.e., the nuclei as a population become clustered around 0.5–1.5 Gyr. However, the uncertainties on these results do not rule out the possibility of older ages (3–6 Gyr)—consistent with the dust-free results.

In a parallel approach, we explored the method of using FIR data to constrain the range of plausible $E(B - V)$ values for our sample objects. In the *Herschel* Virgo Cluster Survey (HeViCS; di Serego Alighieri et al. 2013), only one of our program galaxies, VCC 1619, had a dust detection, with an estimated dust mass $(25.5 \pm 5.5) \times 10^4\,M_\odot$ and dust temperature 21.7 ± 1.0 K. For the remainder of the sample, we assume an upper limit on the dust mass of $2.44 \times 10^3\,M_\odot$, based on stacking the images of 227 early-type dwarfs with non-detections in HeViCS (De Looze et al. 2010).

For the simple scenario of a foreground dust screen in front of a stellar point source (much like a nucleus with foreground galactic dust), the dust optical depth at a given wavelength, τ_λ, is proportional to the reddening $E(B - V)$, following the equation

$$\tau_\lambda = 0.921 E(B - V)\kappa(\lambda),$$

where $\kappa(\lambda)$ is value of the attenuation curve at a given wavelength. The optical depth depends on the dust mass density, ρ_d, the path length through the dust, L, and the dust

Table 7
Properties of Population Synthesis Models

Model Set (1)	Stellar Tracks (2)	Spectral Libraries (3)	IMF (4)	Metallicities (5)
BC03	Padova 1994	STELIB and BaSeL 3.1	Chabrier	$0.0001 \leqslant Z \leqslant 0.05$
M05	Cassisi and Geneva	BaSeL 3.1	Kroupa	$0.0004 \leqslant Z \leqslant 0.04$
PÉGASE.2	Padova 1994	BaSeL 2.2	Kroupa	$0.0001 \leqslant Z \leqslant 0.1$
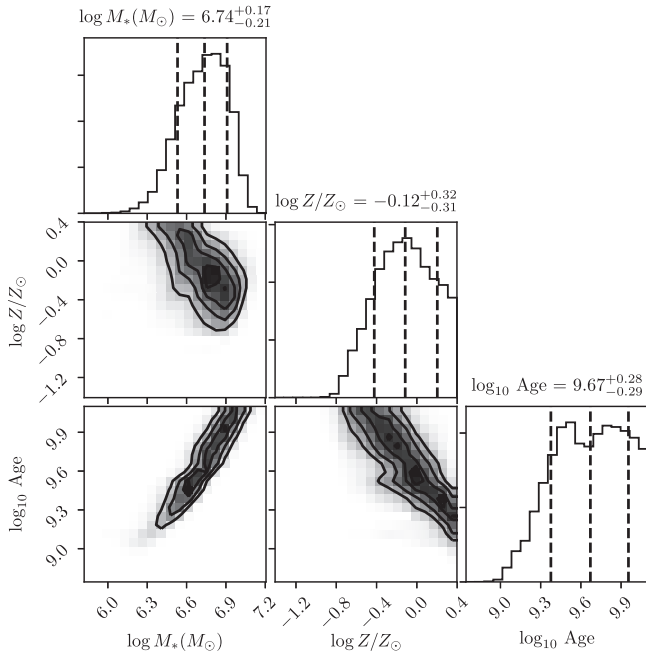
Figure 13. Stellar masses, metallicities, and ages derived using the BC03 models with a Chabrier IMF for the nucleus in VCC 1422. Plots along the diagonal show the collapsed individual posterior probability distributions for the mass (top left), metallicity (middle), and age (bottom right), while the other panels show the joint probability distributions. The median value for each parameter is quoted along the top of the diagonal, with error bars determined from the 16th and 84th percentiles.
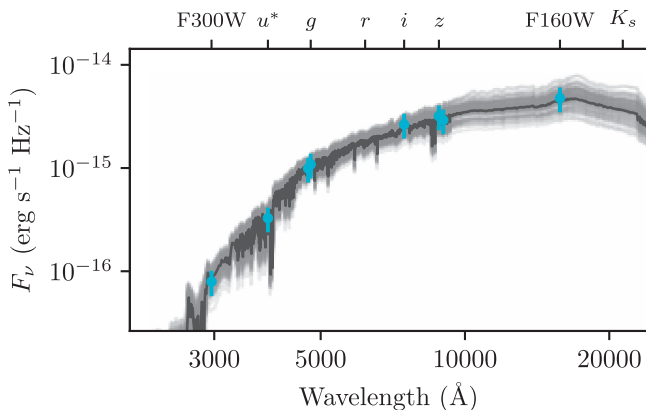
Figure 14. Best-fit model (in black) compared to the observed SED for the nucleus of VCC 1422 (blue points). The model SED has been generated using the best-fit parameters shown in Figure 13. 100 models have been randomly extracted from the posterior distribution and plotted in gray to demonstrate the uncertainty on the best-fit model.

absorption coefficient, k_λ, such that $\tau_\lambda = \rho_d L k_\lambda$. The dust mass density is determined by assuming various areas and values of L to create volumes in which the upper limit dust mass can be

distributed. In the following calculations, we adopt the extinction curve from Calzetti et al. (2000) and the absorption coefficients tabulated in Li & Draine (2001).

To estimate $E(B - V)$ in our program objects, we consider two cases. In the simplest scenario, we assume that all of the dust particles are evenly distributed across the galaxy in some sort of foreground screen. Assuming a typical dE effective radius of $\sim$1 kpc, and therefore a screen of 1 kpc $\times$ 1 kpc, this produces a negligibly small reddening of $E(B - V) = 0.0014$ mag. On the other hand, we find an (extreme) upper limit on $E(B - V)$ if we assume that all of the dust is contained in a foreground cylinder with a radius of $\sim$5 pc (i.e., the size of a typical nucleus). This leads to an upper limit of $E(B - V) = 18$ mag, which is obviously not a useful constraint on the plausible reddening values for these objects.

In a more realistic approach, we assume that the dust has uniform densities throughout the galaxy and nucleus. To estimate this density, we assume that 0.3% of the total dust mass is contained within a spherical volume with a nucleus-sized radius of 5 pc—in other words, the dust mass follows the same nucleus–galaxy stellar mass relation. The value of $E(B - V)$ can be calculated for various path lengths through a foreground screen with this density of dust. A dust screen 5 pc thick generates 0.04 mag of reddening, while a screen of 1 kpc (the typical r_e for early-type Virgo dwarfs) causes 8 mag of reddening. To produce $E(B - V) \sim 0.3$ mag, as suggested by the SED fits for the nuclei, the dust screen must be only 30–40 pc thick.

To summarize, we find that dust can produce non-negligible amounts of reddening, even in objects considered to contain minimal dust, like our program objects. The severity of the effect on the resulting stellar population parameters depends strongly on the distribution of this dust. Unfortunately, without high-resolution, deep imaging in FIR bands, we can only guess at the intrinsic dust distribution. We note, however, that the good agreement between the dust-free metallicity and the spectroscopic metallicities (see Section 5.6 for details) suggests that the assumption of minimal dust is reasonable for these objects, as the Lick indices—given the narrow wavelength coverage of each absorption feature—should be relatively unaffected by reddening.

5.4. Measurement of Spectroscopic Parameters

We use the Lick indices measured in Section 4.2 to estimate an age, [Fe/H], and [Mg/Fe] for each nucleus using the code EZ-AGES (Graves & Schiavon 2008). This code uses the models from Schiavon (2007), which probe ages $0.1 \leqslant t \leqslant 15.8$ Gyr and metallicities $-1.3 \leqslant [Fe/H] \leqslant 0.2$ for the solar-scaled isochrone that we chose for our analysis. EZ-AGES uses a sequential grid inversion technique to determine varied abundance ratios for Fe, Mg, C, N, and Ca (with options to specify ratios for O, Na, Si, Ti, and Cr); however, with the four Lick indices we have available, we can

Table 8
Masses, Metallicities, and Ages Derived from SED Fitting Using BC03

VCC	$\log_{10} M_{\star,\mathrm{gal}}$ ($M_\odot$)	$\log_{10} M_{\star,\mathrm{nuc}}$ ($M_\odot$)	T_{gal} (Gyr)	T_{nuc} (Gyr)	$\log_{10} Z/Z_{\odot,\mathrm{gal}}$ (dex)	$\log_{10} Z/Z_{\odot,\mathrm{nuc}}$ (dex)
(1)	(2)	(3)	(4)	(5)	(6)	(7)
33	$8.72^{+0.15}_{-0.27}$	$5.67^{+0.15}_{-0.24}$	$6.63^{+4.86}_{-4.28}$	$6.32^{+4.91}_{-3.94}$	$-0.85^{+0.33}_{-0.27}$	$-0.32^{+0.47}_{-0.27}$
140	$9.19^{+0.13}_{-0.20}$	$5.68^{+0.19}_{-0.21}$	$7.14^{+4.21}_{-3.89}$	$4.00^{+4.89}_{-2.14}$	$-0.48^{+0.31}_{-0.19}$	$-0.50^{+0.38}_{-0.25}$
200	$8.98^{+0.10}_{-0.17}$	$5.75^{+0.13}_{-0.18}$	$8.19^{+3.75}_{-4.19}$	$7.35^{+4.04}_{-3.60}$	$-0.38^{+0.29}_{-0.20}$	$-0.16^{+0.30}_{-0.36}$
230	$8.56^{+0.15}_{-0.22}$	$6.67^{+0.13}_{-0.25}$	$6.63^{+4.73}_{-3.70}$	$7.97^{+4.18}_{-4.84}$	$-0.61^{+0.31}_{-0.17}$	$-0.78^{+0.25}_{-0.16}$
538	$8.48^{+0.09}_{-0.15}$	$6.48^{+0.13}_{-0.20}$	$8.90^{+3.34}_{-4.05}$	$6.70^{+4.35}_{-3.74}$	$-0.42^{+0.27}_{-0.20}$	$-0.33^{+0.34}_{-0.26}$
698	$9.68^{+0.14}_{-0.19}$	$6.86^{+0.12}_{-0.19}$	$6.11^{+4.36}_{-3.22}$	$7.18^{+4.12}_{-3.82}$	$-0.19^{+0.33}_{-0.28}$	$-0.36^{+0.29}_{-0.23}$
784	$10.23^{+0.07}_{-0.11}$	$7.72^{+0.07}_{-0.10}$	$10.69^{+2.18}_{-3.20}$	$10.68^{+2.12}_{-2.92}$	$0.16^{+0.14}_{-0.14}$	$0.20^{+0.12}_{-0.14}$
828	$10.15^{+0.09}_{-0.13}$	$7.65^{+0.10}_{-0.15}$	$9.25^{+3.13}_{-3.63}$	$8.46^{+3.62}_{-3.69}$	$0.12^{+0.17}_{-0.17}$	$0.09^{+0.19}_{-0.20}$
856	$9.02^{+0.15}_{-0.25}$	$6.93^{+0.16}_{-0.23}$	$6.37^{+4.94}_{-3.82}$	$5.58^{+5.02}_{-3.16}$	$-0.72^{+0.32}_{-0.20}$	$-0.50^{+0.38}_{-0.22}$
1075	$8.78^{+0.15}_{-0.24}$	$6.22^{+0.16}_{-0.27}$	$6.04^{+5.01}_{-3.46}$	$6.13^{+5.54}_{-3.97}$	$-0.63^{+0.32}_{-0.20}$	$-0.73^{+0.39}_{-0.21}$
1087	$9.14^{+0.11}_{-0.16}$	$6.94^{+0.10}_{-0.15}$	$7.98^{+3.75}_{-3.83}$	$8.68^{+3.46}_{-3.59}$	$-0.34^{+0.25}_{-0.20}$	$0.09^{+0.17}_{-0.18}$
1146	$9.93^{+0.11}_{-0.18}$	$8.04^{+0.16}_{-0.23}$	$7.36^{+3.93}_{-3.73}$	$6.16^{+5.12}_{-3.44}$	$-0.23^{+0.25}_{-0.21}$	$-0.61^{+0.30}_{-0.16}$
1185	$8.70^{+0.11}_{-0.18}$	$6.38^{+0.17}_{-0.25}$	$8.81^{+3.53}_{-4.48}$	$5.29^{+5.34}_{-3.06}$	$-0.79^{+0.17}_{-0.15}$	$-0.57^{+0.35}_{-0.21}$
1192	$9.09^{+0.10}_{-0.16}$	$7.44^{+0.13}_{-0.19}$	$7.77^{+4.04}_{-3.58}$	$6.32^{+4.26}_{-3.41}$	$-0.02^{+0.23}_{-0.23}$	$-0.25^{+0.34}_{-0.23}$
1199	$8.60^{+0.10}_{-0.14}$	$7.30^{+0.10}_{-0.15}$	$8.31^{+3.69}_{-3.41}$	$8.49^{+3.67}_{-3.70}$	$0.04^{+0.20}_{-0.21}$	$0.03^{+0.21}_{-0.20}$
1242	$10.04^{+0.13}_{-0.19}$	$8.11^{+0.08}_{-0.11}$	$6.42^{+4.21}_{-3.44}$	$9.70^{+2.81}_{-3.21}$	$-0.30^{+0.32}_{-0.26}$	$0.08^{+0.16}_{-0.14}$
1261	$9.37^{+0.16}_{-0.23}$	$6.31^{+0.30}_{-0.29}$	$5.20^{+5.23}_{-2.94}$	$3.25^{+7.16}_{-2.01}$	$-0.53^{+0.38}_{-0.24}$	$-0.71^{+0.64}_{-0.46}$
1283	$9.64^{+0.15}_{-0.19}$	$7.13^{+0.10}_{-0.15}$	$5.85^{+4.32}_{-3.09}$	$8.42^{+3.68}_{-3.74}$	$-0.26^{+0.35}_{-0.29}$	$0.05^{+0.20}_{-0.20}$
1355	$9.10^{+0.14}_{-0.22}$	$6.25^{+0.15}_{-0.23}$	$6.81^{+4.41}_{-3.94}$	$5.92^{+4.96}_{-3.29}$	$-0.52^{+0.32}_{-0.18}$	$-0.59^{+0.33}_{-0.19}$
1407	$8.83^{+0.14}_{-0.20}$	$6.41^{+0.18}_{-0.26}$	$6.97^{+4.29}_{-3.76}$	$4.14^{+5.10}_{-2.55}$	$-0.51^{+0.29}_{-0.17}$	$-0.37^{+0.49}_{-0.29}$
1422	$9.39^{+0.15}_{-0.22}$	$6.86^{+0.11}_{-0.17}$	$5.59^{+4.85}_{-3.09}$	$7.57^{+3.99}_{-3.93}$	$-0.49^{+0.36}_{-0.23}$	$-0.27^{+0.29}_{-0.23}$
1431	$9.21^{+0.11}_{-0.17}$	$6.81^{+0.16}_{-0.24}$	$7.77^{+3.82}_{-3.98}$	$5.56^{+5.16}_{-3.11}$	$-0.32^{+0.28}_{-0.22}$	$-0.59^{+0.35}_{-0.20}$
1440	$8.97^{+0.12}_{-0.20}$	$6.69^{+0.05}_{-0.06}$	$7.19^{+4.20}_{-3.92}$	$13.26^{+0.40}_{-0.79}$	$-0.21^{+0.31}_{-0.25}$	$0.38^{+0.01}_{-0.01}$
1489	$8.39^{+0.13}_{-0.25}$	$5.65^{+0.17}_{-0.27}$	$8.15^{+3.88}_{-4.74}$	$6.81^{+4.79}_{-4.22}$	$-1.08^{+0.27}_{-0.43}$	$-1.19^{+0.38}_{-0.56}$
1539	$8.23^{+0.18}_{-0.21}$	$6.19^{+0.18}_{-0.29}$	$5.69^{+4.14}_{-2.92}$	$6.30^{+5.61}_{-4.21}$	$-1.81^{+0.41}_{-0.33}$	$-0.79^{+0.34}_{-0.22}$
1545	$8.85^{+0.15}_{-0.25}$	$6.18^{+0.17}_{-0.18}$	$6.46^{+4.80}_{-3.75}$	$4.34^{+4.59}_{-2.12}$	$-0.69^{+0.28}_{-0.18}$	$-0.06^{+0.33}_{-0.35}$
1619	$9.98^{+0.14}_{-0.21}$	$7.55^{+0.07}_{-0.09}$	$6.44^{+4.36}_{-3.47}$	$11.46^{+1.68}_{-2.53}$	$-0.51^{+0.31}_{-0.21}$	$0.31^{+0.06}_{-0.10}$
1627	$8.90^{+0.12}_{-0.17}$	$6.35^{+0.25}_{-0.34}$	$7.51^{+4.04}_{-3.85}$	$4.78^{+6.05}_{-3.51}$	$-0.29^{+0.33}_{-0.27}$	$-1.23^{+0.79}_{-0.67}$
1630	$10.04^{+0.10}_{-0.16}$	$7.78^{+0.07}_{-0.11}$	$8.17^{+3.78}_{-3.93}$	$10.51^{+2.32}_{-3.34}$	$-0.11^{+0.26}_{-0.22}$	$0.24^{+0.10}_{-0.14}$
1661	$8.40^{+0.19}_{-0.21}$	$6.43^{+0.09}_{-0.14}$	$6.66^{+4.29}_{-3.29}$	$9.80^{+2.76}_{-3.94}$	$-0.05^{+0.30}_{-0.51}$	$-0.54^{+0.21}_{-0.13}$
1826	$8.50^{+0.15}_{-0.24}$	$6.72^{+0.15}_{-0.23}$	$6.48^{+4.82}_{-3.77}$	$6.54^{+4.77}_{-3.77}$	$-0.72^{+0.29}_{-0.18}$	$-0.60^{+0.33}_{-0.18}$
1828	$8.79^{+0.14}_{-0.20}$	$6.11^{+0.15}_{-0.23}$	$6.40^{+4.55}_{-3.55}$	$6.18^{+5.00}_{-3.44}$	$-0.40^{+0.33}_{-0.24}$	$-0.68^{+0.28}_{-0.18}$
1861	$9.10^{+0.15}_{-0.23}$	$6.71^{+0.16}_{-0.24}$	$6.31^{+4.77}_{-3.59}$	$5.24^{+5.51}_{-3.03}$	$-0.62^{+0.31}_{-0.19}$	$-0.61^{+0.38}_{-0.22}$
1871	$9.27^{+0.12}_{-0.17}$	$7.17^{+0.13}_{-0.19}$	$7.30^{+3.96}_{-3.69}$	$6.38^{+4.39}_{-3.41}$	$-0.26^{+0.28}_{-0.23}$	$-0.19^{+0.33}_{-0.22}$
1883	$10.09^{+0.14}_{-0.20}$	$4.89^{+0.21}_{-0.46}$	$6.71^{+4.24}_{-3.68}$	$5.76^{+5.34}_{-4.91}$	$-0.47^{+0.31}_{-0.22}$	$-1.27^{+0.98}_{-0.73}$
1886	$8.56^{+0.17}_{-0.27}$	$5.87^{+0.10}_{-0.20}$	$5.92^{+5.33}_{-3.87}$	$9.37^{+3.14}_{-4.74}$	$-0.91^{+0.42}_{-0.47}$	$-1.16^{+0.29}_{-0.40}$
1910	$9.19^{+0.15}_{-0.20}$	$6.89^{+0.14}_{-0.20}$	$5.85^{+4.48}_{-3.14}$	$7.04^{+4.36}_{-3.83}$	$-0.32^{+0.35}_{-0.28}$	$-0.55^{+0.30}_{-0.17}$
2019	$8.94^{+0.15}_{-0.22}$	$6.69^{+0.13}_{-0.20}$	$5.58^{+5.08}_{-3.05}$	$6.89^{+4.35}_{-3.77}$	$-0.59^{+0.34}_{-0.22}$	$-0.40^{+0.32}_{-0.23}$
2050	$8.94^{+0.07}_{-0.10}$	$5.65^{+0.15}_{-0.21}$	$11.04^{+2.07}_{-3.99}$	$6.70^{+4.59}_{-3.74}$	$-0.11^{+0.19}_{-0.16}$	$-0.23^{+0.41}_{-0.48}$

only determine [Fe/H] and [Mg/Fe]. Following the default settings of EZ-AGES, C, N, Ca, O, and Cr are fixed to solar values ([X/Fe] = 0), and Na, Si, and Ti are fixed to Mg ([X/Fe] = [Mg/Fe]).

In brief, EZ-AGES first calculates an initial guess for the population age and [Fe/H] using a model grid of H_β and $\langle Fe \rangle$, an average of Fe5270 and Fe5335. It then creates another model grid using $\langle Fe \rangle$ and Mgb to probe [Mg/Fe], and adjusts [Mg/Fe] until this grid fits a model with age and [Fe/H] values sufficiently similar to the fiducial estimates. For our purposes, the code stops here because we provide no other indices to constrain other element ratios. Lastly, the code computes errors on the age and [Fe/H] by shifting the H_β, Fe5270, and Fe5335 indices by their error bars and repeating the grid inversion. For other element abundances, errors are determined by

uncertainties on the fiducial age and [Fe/H] as well as errors on the relevant Lick indices.

There are a few caveats to the results of this analysis. In some nuclei, low S/N can influence the pseudo-continuum estimates surrounding the Lick indices, introducing a bias to the measurements. Additional uncertainty arises due to smoothing the spectra to the Lick resolution, which may not be matched perfectly. Finally, even though there is evidence indicating that these objects may be α-enhanced (Liu et al. 2016), we used the solar-scaled isochrones in EZ-AGES rather than the α-enhanced versions because those have been found to predict ages that are too old (Weiss et al. 2006; Schiavon 2007). The fitting process in EZ-AGES can still produce supersolar enhancements for *individual* elements such as Mg (and the other elements set to follow the [Mg/Fe]
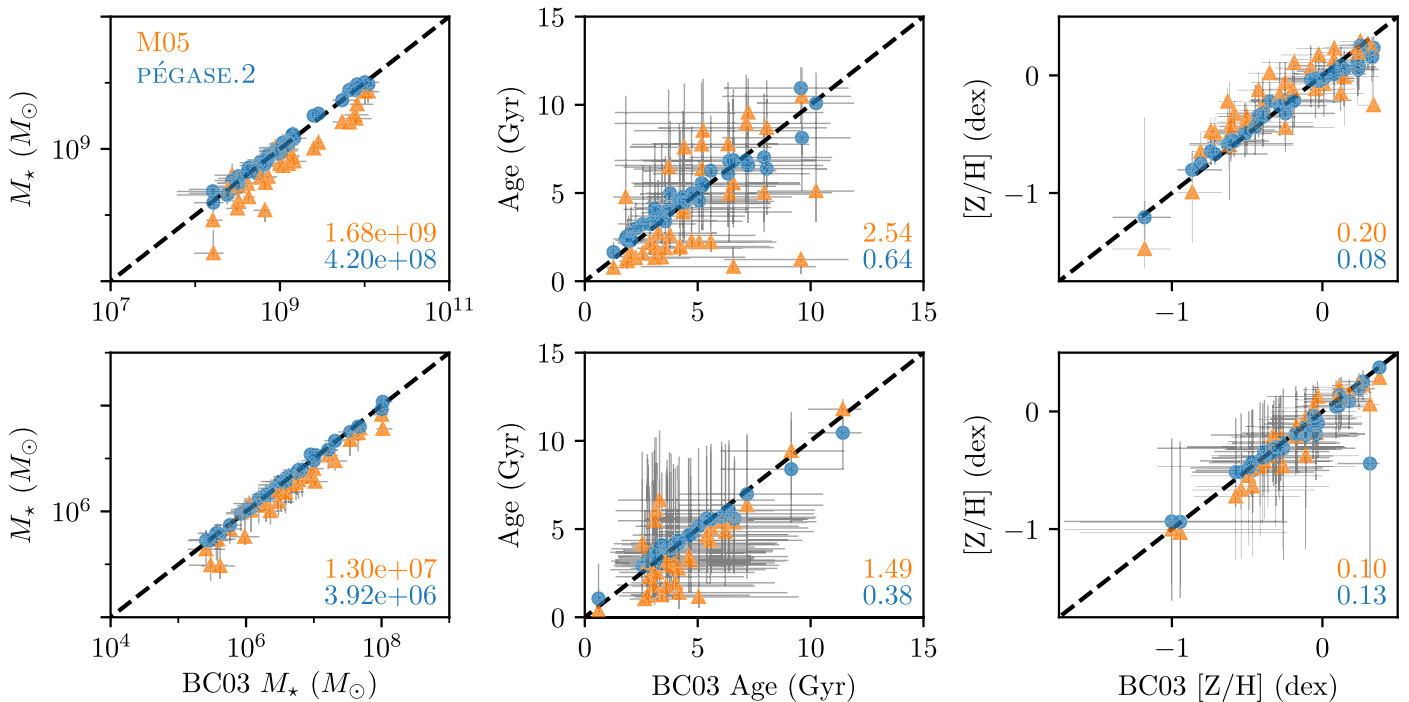
Figure 15. Comparison of stellar masses (left column), ages (middle column), and metallicities (right column) found using different SSP models in the SED-fitting analysis. Values from the BC03 models (plotted along the abscissa, listed in Table 8, and adopted as our preferred values) are plotted against the M05 (Maraston 2005) and PÉGASE.2 (Fioc & Rocca-Volmerange 1997, 1999) values (orange triangles and blue circles, respectively). Results are shown for both galaxies (top row) and nuclei (bottom row). The dashed line in each panel shows the one-to-one relation, while the numbers in the bottom-right corner show the rms scatter, in the same units in each panel, between M05 and BC03 (in orange), and PÉGASE.2 and BC03 (in blue).

value); however, the abundances of the remaining elements will remain solar-scaled as we do not provide any index measurements for those elements. This may be a non-physical model for α-enhanced objects and introduces uncertainty in our estimates.

For consistency with the photometric results, we quote [Z/H] based on the estimated [Fe/H] and [Mg/Fe] values using the equation

$$[Z/H] = [Fe/H] + 0.94 \, [\alpha/Fe], \quad (5)$$

where we use [Mg/Fe] as a proxy for [α/Fe] (Trager et al. 2000; Thomas et al. 2003). Considering that most of the α-elements are set to match the Mg abundance, this is a reasonable approximation. Our resulting age, [Z/H], and [α/Fe] estimates are provided in Table 9. When multiple measurements are available for a nucleus, we quote the weighted median value.

Just as we did for the indices in Section 4.2, we now compare the age and abundance estimates for objects included in two or more of the spectroscopic data sets. These comparisons are shown in Figure 16. There are fewer data here compared to Figure 11 because EZ-AGES could not always converge on a fit to the provided index measurements. We find excellent agreement for [α/Fe] and [Z/H] among the data sets. Age estimates are less consistent and less certain than the abundance estimates, likely due to the inherent challenges of separating SSP ages for populations older than a few Gyr.

5.5. Comparison to Previous Spectroscopic Studies

In Figure 17, we show the published spectroscopic age and metallicity measurements for our sample galaxies along with our estimates from SED fitting of the photometry. In general,

Table 9
Best-fit SSP Parameters from Spectroscopy

VCC	Instruments	T (Gyr)	[Z/H] (dex)	[α/Fe] (dex)
(1)	(2)	(3)	(4)	(5)
33	ESI, GMOS	$2.12^{+0.32}_{-0.75}$	$-0.61^{+0.37}_{-0.42}$	$0.03^{+0.18}_{-0.19}$
200	ESI	$3.40^{+1.29}_{-4.69}$	$-0.15^{+0.38}_{-0.43}$	$0.00^{+0.20}_{-0.20}$
230	ESI	$3.68^{+1.46}_{-4.01}$	$-0.56^{+0.47}_{-0.54}$	$0.00^{+0.28}_{-0.26}$
538	ESI	$3.26^{+1.18}_{-4.51}$	$-0.22^{+0.39}_{-0.43}$	$-0.04^{+0.20}_{-0.20}$
1075	ESI, DEIMOS	$4.44^{+1.56}_{-5.40}$	$-0.87^{+0.46}_{-0.47}$	$-0.04^{+0.24}_{-0.22}$
1185	ESI, GMOS	$4.77^{+1.56}_{-3.57}$	$-0.59^{+0.29}_{-0.32}$	$-0.04^{+0.16}_{-0.16}$
1192	ESI	$6.51^{+3.77}_{-6.60}$	$0.23^{+0.31}_{-0.39}$	$0.24^{+0.22}_{-0.20}$
1199	ESI	$3.78^{+1.89}_{-6.60}$	$0.20^{+0.33}_{-0.33}$	$0.04^{+0.14}_{-0.14}$
1407	ESI, DEIMOS	$5.63^{+2.22}_{-2.46}$	$-0.62^{+0.36}_{-0.37}$	$0.31^{+0.26}_{-0.23}$
1440	ESI	$5.59^{+2.89}_{-7.90}$	$-0.11^{+0.36}_{-0.41}$	$0.04^{+0.23}_{-0.23}$
1489	ESI	$3.67^{+1.46}_{-2.90}$	$-1.00^{+0.46}_{-0.47}$	$-0.22^{+0.14}_{-0.21}$
1539	ESI, DEIMOS, GMOS	$10.72^{+3.60}_{-2.27}$	$-0.98^{+0.41}_{-0.40}$	$0.28^{+0.21}_{-0.20}$
1545	ESI, DEIMOS, GMOS	$4.75^{+1.29}_{-2.66}$	$0.00^{+0.13}_{-0.16}$	$-0.04^{+0.08}_{-0.08}$
1627	ESI	$4.93^{+3.20}_{-7.95}$	$0.19^{+0.33}_{-0.32}$	$0.04^{+0.15}_{-0.12}$
1826	ESI	$3.73^{+1.53}_{-4.68}$	$-0.44^{+0.44}_{-0.51}$	$0.00^{+0.26}_{-0.26}$
1828	ESI	$5.20^{+2.59}_{-6.15}$	$-0.56^{+0.49}_{-0.57}$	$0.12^{+0.29}_{-0.29}$
1861	DEIMOS	$5.47^{+3.33}_{-5.33}$	$-0.80^{+0.43}_{-0.49}$	$-0.12^{+0.24}_{-0.26}$
1871	DEIMOS	$9.15^{+5.67}_{-4.40}$	$0.04^{+0.12}_{-0.14}$	$0.00^{+0.08}_{-0.09}$
2050	ESI	$3.31^{+1.20}_{-3.99}$	$-0.50^{+0.46}_{-0.51}$	$0.00^{+0.26}_{-0.26}$

spectroscopic values are consistent within their uncertainties, although the average age differences among measurements are 4.3 ± 2.2 Gyr for ages and 0.48 ± 0.23 dex for metallicities. Some of these discrepancies can likely be explained by the use of different model sets when fitting the data, or by differences in the spatial coverage of the galaxies themselves. Consider, for
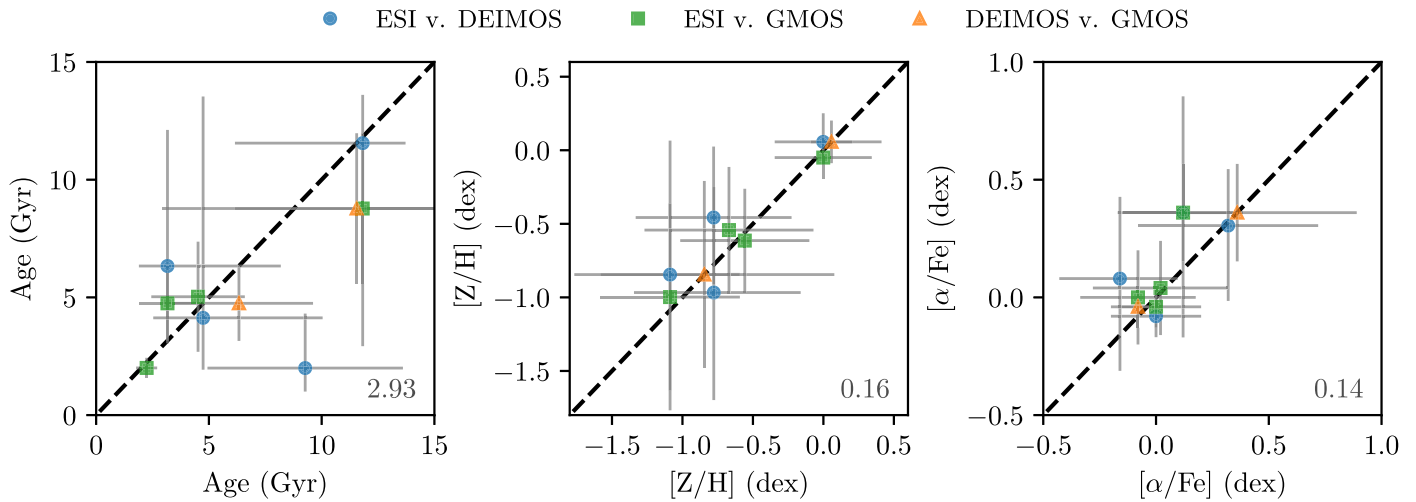
Figure 16. Comparison of age, [Z/H], and [α/Fe] estimates among the ESI, GMOS, and DEIMOS data sets. Symbols are the same as in Figure 11. The dashed line in each panel shows the one-to-one relation, while numbers in the bottom-right corner show the rms scatter in the units of each panel.

example, the ATLAS3D measurements from McDermid et al. (2015), whose values are measured within one effective radius and use the Schiavon (2007) models for comparison to Lick index measurements. Their measurements often differ from those of Koleva et al. (2011), who relied on full spectral fitting and compared to the PÉGASE.HR models (although they too focused on the region inside one effective radius). Similarly, the discrepancies with Yamada et al. (2006) are likely due to model differences (i.e., they used SSP models from Vazdekis 1999), the large number of spectral indices used in their analysis, and differences in spatial sampling (i.e., the latter study focused on the galaxy spectrum within ∼0.1 R_e). An additional hurdle in measuring ages is the difficulty in distinguishing between SSP models older than ∼6 Gyr (see, e.g., Powalka et al. 2016). Since most early-type galaxies contain a prominent old stellar population, it is clear that the estimation of accurate ages is quite challenging.

In Figure 18, we show a similar comparison for the nuclei. Parameter estimates for the nuclei have an additional source of uncertainty—possible contamination of the nucleus spectrum by the underlying galaxy, which could affect the derived nuclei parameters. A comparison of independent spectroscopic measurements may therefore help us understand the importance of such possible systematic errors. Unfortunately, such measurements are available in the literature for only four nuclei in our sample, from two studies: Chilingarian (2009) and Paudel et al. (2011). The ages are generally in good agreement, with only one nucleus, VCC 856, showing discrepant spectral age estimates from the literature. Three nuclei (VCC 856, VCC 1261, and VCC 2019) have conflicting metallicity estimates from the literature. We note that Paudel et al. (2011) modeled the galaxy light profile and subtracted it from their nuclei estimates, while Chilingarian (2009) did not. This is likely a key factor in the overall discrepancy between the two sets of measurements. It is also interesting to note that our photometric metallicities seem more consistent with those from Chilingarian (2009), even though our extraction methodology is more similar to that of Paudel et al. (2011). This is perhaps an effect of the different SSP models used in each analysis. Of course, it is difficult to draw firm conclusions with only four nuclei in common among the samples.
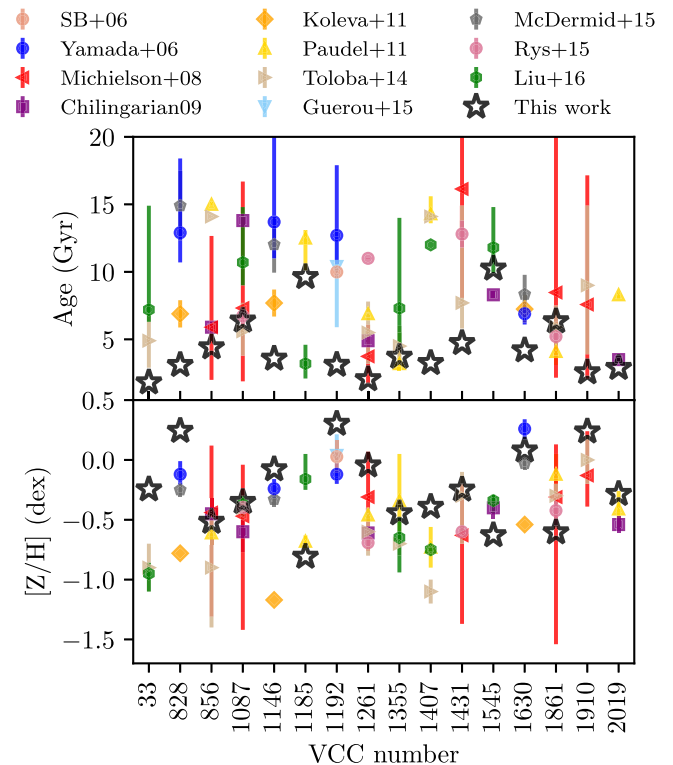
Figure 17. Comparison of our spectroscopic ages (upper panel) and metallicities (lower panel) with estimates from the literature for our program galaxies. Only objects with more than one literature estimate are included. Estimates derived from our SED analysis are plotted as black stars.

5.6. Comparison of Spectroscopic and Photometric Results

In this section, we compare the ages and metallicities derived for the nuclei using the ESI, GMOS, and DEIMOS spectra to those found from SED fitting of the photometry. It is worth emphasizing that spectra have all been reduced in similar ways, with the galaxy light modeled and removed from the nucleus in all cases (see Section 4.1). In addition, the spectra have been analyzed in an identical manner, using a single model set and methodology (as described in Sections 4.2 and 5.4). This homogeneous analysis should reduce the possible sources of
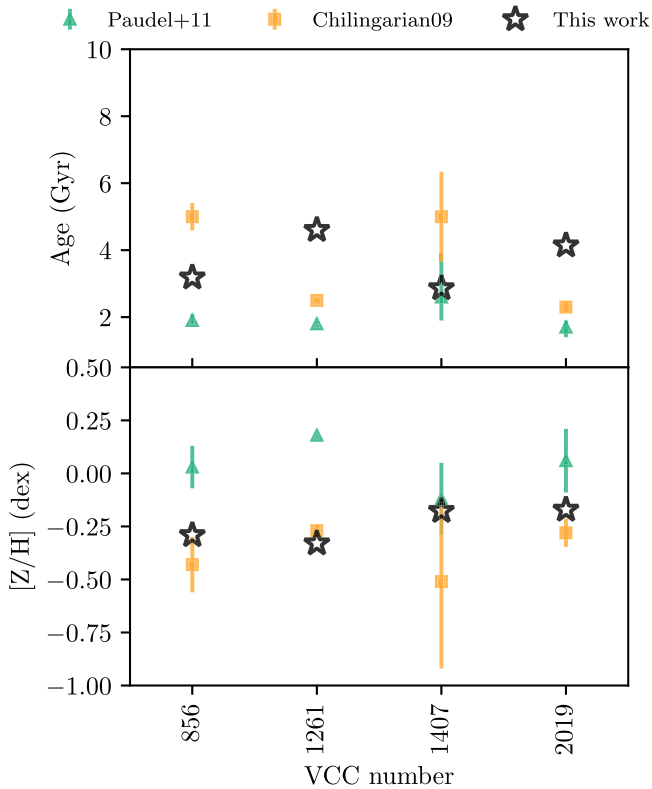
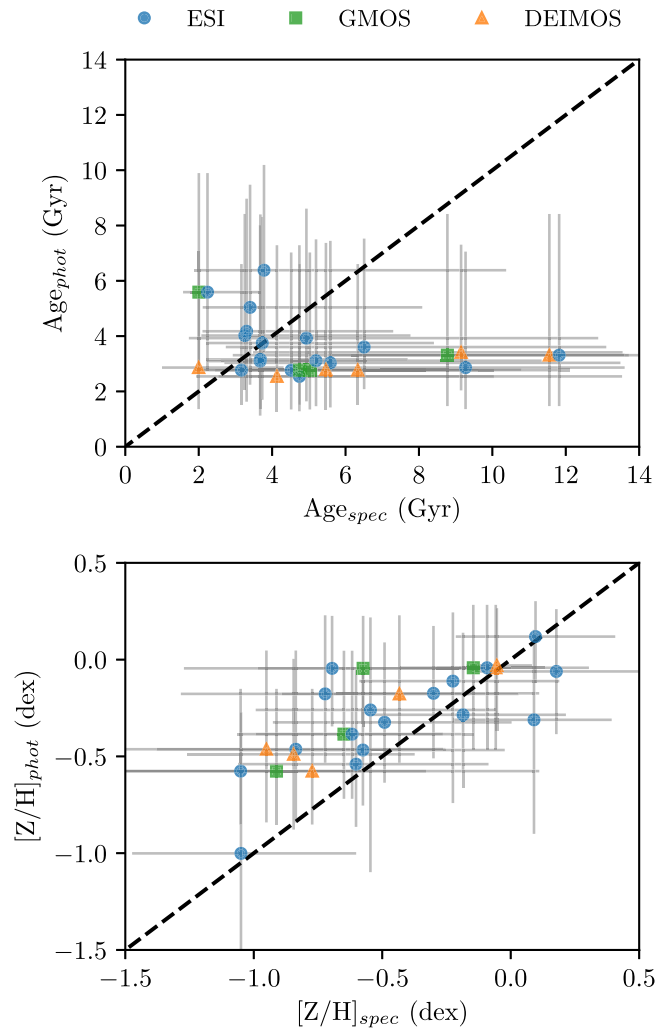**Figure 18.** Same comparison as in Figure 17, but for the nuclei.

Figure 19. Comparison of nuclei ages (top panel) and metallicities (bottom panel) derived from our photometric and spectroscopic analyses. The values from SED fitting were calculated using the BC03 models. Typical uncertainties for the measurements are shown by the black error bars in each panel. The dashed line in each panel shows the one-to-one relation.

disagreement among the data sets, so that any scatter in the results should largely be attributable to the data.

Figure 19 compares our photometric age and metallicity estimates (calculated using the BC03 models) to the corresponding spectroscopic estimates. In general, there is good agreement within the uncertainties. In particular, the derived metallicities appear to be robust; the rms scatter is 0.3 dex with a Spearman rank correlation coefficient $\rho = 0.79$. The ages seem to be more uncertain, five nuclei having fairly old (9–12 Gyr) spectroscopically derived ages but younger (~ 3 Gyr) photometric ages. This discrepancy can be attributed to the similar broadband features of populations older than a few Gyr. In addition, the spectroscopic data only include four optical lines, which also limits their ability to discriminate in age. Overall, this comparison illustrates, once again, the challenges inherent in distinguishing between old ($\gtrsim 5$ Gyr) and intermediate-age populations. Based on these comparisons, we conclude that photometry alone can provide accurate metallicity estimates for galaxies and nuclei. The age estimates, while less tightly constrained, can at least eliminate the presence of prominent young ($\lesssim 2$ Gyr) stellar populations in either system.

6. Discussion

6.1. Masses and Relation to Host Galaxies

In the SED fitting process, we measure stellar masses for both nuclei and their host galaxies. The uncertainties in the derived masses range from $\sim 15\%$ to $\sim 75\%$, with most masses having a precision of $\sim 35\%$. These uncertainties are dramatically improved over previous literature estimates (Ferrarese et al. 2006a; Leigh et al. 2012; Georgiev et al. 2016), even without imposing fixed values for the age,

metallicity, or M/L. Our mass uncertainties are dominated by the relatively large uncertainties on age: i.e., at a given metallicity, a 10 Gyr population will require $\sim 30\%$ more mass to emit as much light as a 2 Gyr population.

In Figure 20, we show the nucleus–galaxy mass relation found using our median masses (which were computed using the BC03 SSP models and a Chabrier IMF). To extend the nucleus–galaxy relation to lower masses, we included masses for 107 nucleated galaxies from the NGVS located in the 4 deg^2 region surrounding M87 (R. Sánchez-Janssen et al. 2017, in preparation). Note that these masses are approximate, being calculated from the observed i-band magnitudes and a mean M/L computed from the NGVS optical colors. The gray curve shows the best-fit relation of R. Sánchez-Janssen et al. (2017, in preparation).

We overplot the observed data with predictions from three different simulations: Antonini et al. (2015, hereafter A15), Gnedin et al. (2014, hereafter G14), and Bekki (2007, hereafter B07). A15 provide an analytic mass relation for their model CliN. This is a simple model of GC infall within an isolated spheroid. A15 also use a more complex model (GxeV) that allows for in situ star formation as well as galaxy and black hole mergers in addition to GC infall. However, the resulting
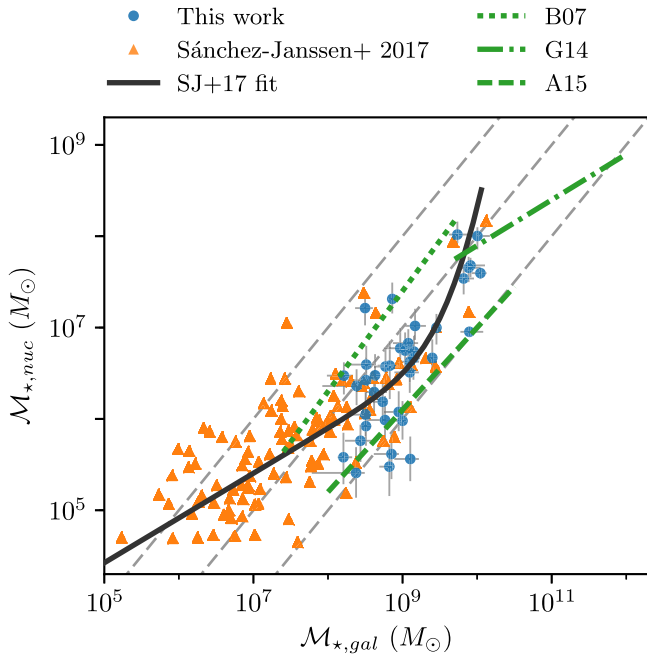
Figure 20. Nucleus stellar mass plotted as a function of galaxy stellar mass. Blue points show the 39 galaxies from this work, while green points are estimates based on NGVS u^*griz photometry from R. Sánchez-Janssen et al. (2017, in preparation) for 107 nucleated galaxies in a 4 deg^2 region centered on M87. Dotted light gray lines indicate, from left to right, mass fractions of 10%, 1%, and 0.1%. The solid dark gray curve shows the mass relation derived by R. Sánchez-Janssen et al. (2017, in preparation). We also include a comparison to three nucleus formation models: Antonini et al. (2015), Gnedin et al. (2014), and Bekki (2007). A description of these models is given in the text.

Figure 21. Mass–metallicity relations for our sample nuclei and galaxies (blue circles and green squares, respectively). For comparison, orange triangles show UCDs in the M87 region from Liu et al. (2015). Masses and metallicities for the three different types of stellar systems were derived homogeneously using the BC03 SSP models with a Chabrier IMF. Note, however, that F300W and F160W photometry is unavailable for the UCDs, and roughly a third of the sample also does not have r or K_s imaging. The dotted line shows the fitted relation for the nuclei, while the solid line shows the galaxy mass–metallicity relation from the simulations in Ma et al. (2016), shifted to higher metallicities by 0.3 dex. VCC numbers are labeled for galaxies that diverge from this mass–metallicity relation.

mass relations for both models look quite similar in the regime of our data, with GxeV producing a relation with larger scatter.

The G14 model is a numerical model based on pure cluster infall via dynamical friction. This model produces nucleus-to-galaxy mass fractions that are consistent with the observed fractions for Virgo nuclei (as well as other samples). However, these mass fractions are for more massive simulated galaxies (ranging from galaxies comparable to the Milky Way to M87-like systems). The results from G14 show that nuclei become slightly more prominent as galaxy mass decreases. Therefore, once their mass relation is extrapolated to the mass regime of this work, the predicted nuclei masses are somewhat over-massive. However, it is important to note that G14 quote the total stellar mass within 10 pc of the galaxy center as the nucleus mass; they also caution that their dynamical friction model might be too effective in migrating clusters to the galaxy center. The G14 predicted mass relation differs significantly from the CliN relation; this is likely due to the absence of black hole disruption in the G14 scenario.

Lastly, there is the prediction from the B07 model, which is a pure dissipative formation model accounting for nucleus growth regulation from stellar feedback and a central black hole. The model galaxy is a spheroid (usually about 10^9 solar masses), within which is embedded a 1 kpc gas disk. Different iterations of the model assign between 2% and 50% of the mass to the gas disk. The models typically produce a nucleus with ~4.6% of the spheroid mass, a larger mass fraction than observed in this sample. This efficient formation scenario may be appropriate for nuclei in the lower-mass galaxies considered

in the model ($M_{\star,\text{gal}} \approx 10^8$), which tend to be more prominent within the host galaxy.

The B07 and A15 mass relations have slopes that are roughly consistent with the trend among the most massive nucleated galaxies ($M_{\star,\text{gal}} \geqslant 10^8$), although the B07 relation produces overmassive nuclei, while the A15 relation produces under-massive nuclei. The observed mass relation is effectively bounded by these two cases, suggesting that variation in mass fraction can be produced by varying the contribution of dissipative and dissipationless formation processes. This is supported by the results shown in A15, in which the GxeV model produces a wide range of nucleus masses at fixed galaxy mass.

6.2. Abundances

In this section, we examine the photometrically derived SSP ages and metallicities, focusing mainly on the estimates found using a Chabrier IMF and the BC03 SSP models (Table 8).

A comparison of the masses and metallicities for the galaxies and nuclei is shown in Figure 21. For comparison, we also show results for UCDs based on the sample of Liu et al. (2015). We used the published u^*giz photometry (and, when available, r and K_s photometry) to estimate the mass, metallicity, and age using the SED fitting procedure described in Section 5.2. This figure shows that a remarkably similar mass–metallicity relation holds for both the nuclei and galaxies. Fitting an equation of the form $\log_{10} Z/Z_\odot = \alpha \log_{10} M_\star + \beta$ yields $\alpha = 0.41 \pm 0.05$ and $\beta = -2.80 \pm 0.35$ for the nuclei. We compare the galaxies to the relation produced by the simulations of Ma et al. (2016). The slope of this relation fits the data well; however, a shift of +0.3 dex in metallicity is required to match the data. This offset may be explained by morphological or environmental
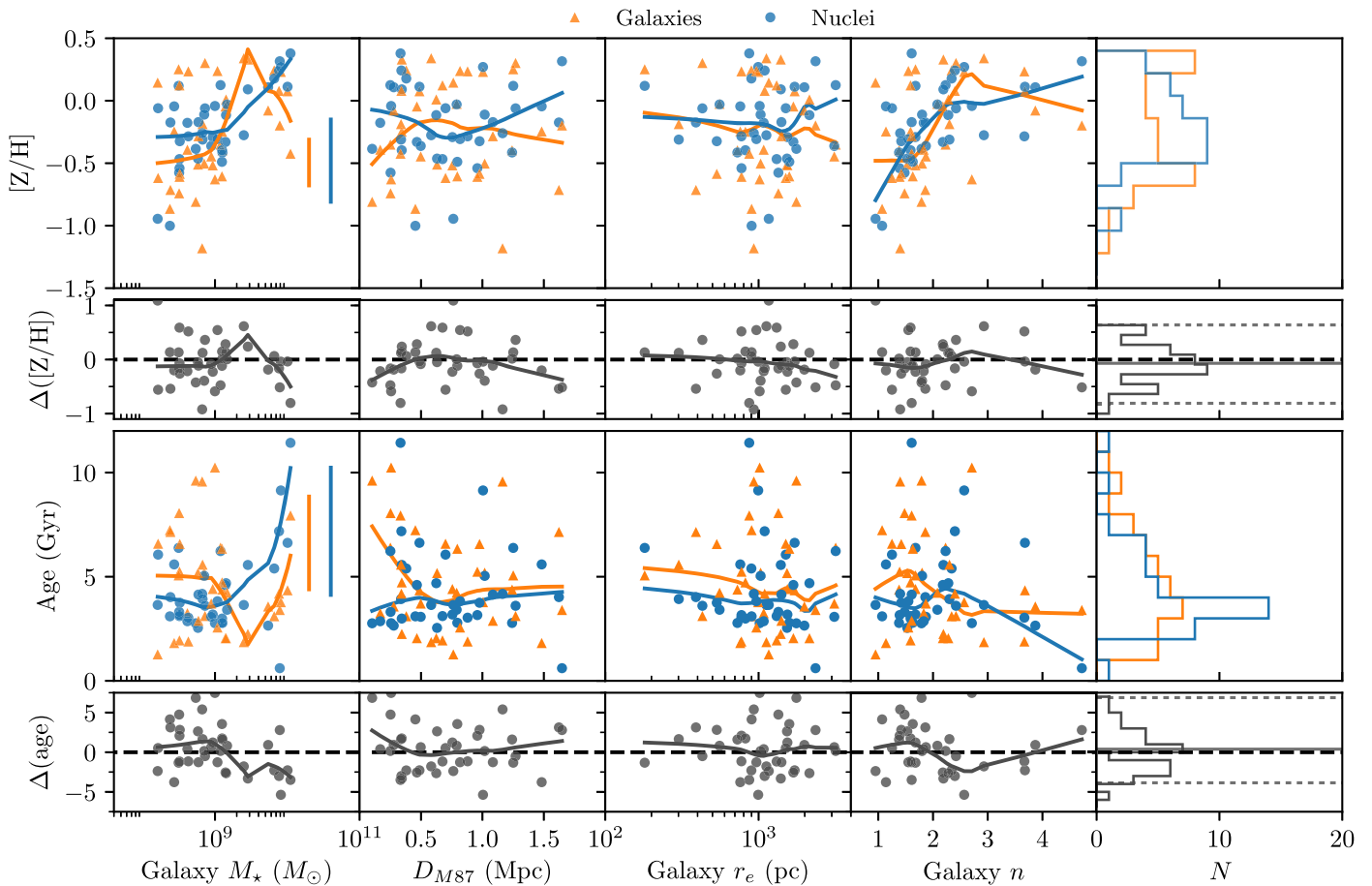
Figure 22. Metallicities (first row), metallicity differences (galaxy [Z/H]–nucleus [Z/H]; second row), ages (third row), and age differences (galaxy age–nucleus age; fourth row) for galaxies (orange triangles) and nuclei (blue circles). These parameters are plotted, from left to right, against galaxy stellar mass, distance to M87 (as a proxy for environment density), galaxy effective radius, and galaxy Sérsic index. LOWESS (Cleveland 1979) fits are shown as solid lines in each panel. Typical error bars are shown in the first column in orange and blue for galaxies and nuclei, respectively. Distributions for each population are shown in the far right column, with the mean (solid line) and 2.5 and 97.5 percentiles (dotted lines) shown for the metallicity and age difference distributions. Metallicity and age values are derived using the BC03 models with a Chabrier IMF.

differences—since we are looking exclusively at early-type galaxies in a cluster environment—or by different model assumptions. A few outliers are found to have metallicities even higher than the shifted relation. These include the compact ellipticals VCC 1192, VCC 1199, and VCC 1440, as well as the bright, structurally complex galaxies VCC 698 and VCC 1283.

Nuclei and galaxies are found to occupy a similar, broad range in metallicity. It is interesting to note that, at fixed mass, the UCDs are systematically *less* metal-rich (by 0.56 ± 0.12 dex) than the nuclei. UCDs are thought to be either the stripped remains of nucleated galaxies, or simply the high-mass tail of the globular cluster luminosity function (e.g., Mieske et al. 2013; Norris et al. 2014; Pfeffer et al. 2014; Janz et al. 2016). In the mass range 10^6–$10^8\,M_\odot$, Janz et al. (2016) find that the UCDs span a broad metallicity range $-1.1 \leqslant [Z/H] \leqslant 0.2$, consistent with a sample containing both stripped objects and GCs. We do not detect any solar or supersolar metallicity UCDs, which may suggest that our sample is predominantly high-mass GCs. However, a subset of the UCDs overlap with the nucleus sample, suggesting that these UCDs and nuclei are drawn from the same population. Perhaps the UCD hosts were stripped or disrupted at early times, removing the surrounding supply of gas and halting their chemical enrichment. However, firm conclusions regarding UCD metallicities would be premature because other factors

may be at play. For instance, the sample of galaxies and nuclei examined in this paper are scattered throughout the entire cluster (see Figure 3), whereas the UCDs of Liu et al. (2015) are drawn from the central $\sim 4\,\mathrm{deg}^2$ and, thus, may be among the oldest stellar systems in Virgo (e.g., Lisker et al. 2009).

In the top two rows of Figure 22, we plot the nucleus and galaxy metallicities, as well as the metallicity differences, as a function of galaxy stellar mass, number density, galaxy effective radius, and galaxy Sérsic index. We see that both galaxies and nuclei trend toward higher metallicities as the mass increases. On average, the nuclei in our sample have metallicities statistically indistinguishable from those of their host galaxies, with a mean metallicity 0.07 ± 0.3 dex higher than that of their hosts. However, if we exclude the galaxies (and their corresponding nuclei) that deviate from the mass–metallicity relation in Figure 21, then the nuclei are, on average, 0.20 ± 0.28 dex more metal-rich than their hosts. This suggests that most nuclei are not formed primarily via GC infall, as GC systems typically have lower metallicities than their host galaxies (Jordán et al. 2004b; Puzia et al. 2005). It is also apparent that the metallicity distributions, shown in the top right panel of Figure 22, are shaped differently, with nuclei having a broad, single-peaked distribution, compared to a bimodal distribution for the galaxies.
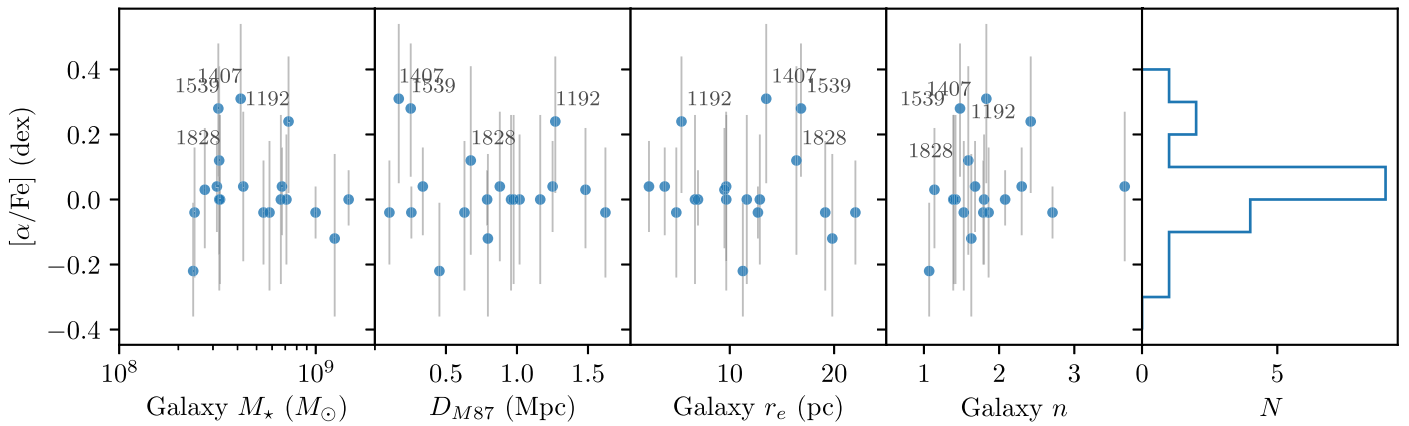
Figure 23. Nucleus [α/Fe] plotted as a function of, from left to right, galaxy stellar mass, distance to M87 (as a proxy for environmental density), galaxy effective radius, and galaxy Sérsic index. The far right panel shows the [α/Fe] histogram. Nuclei with [α/Fe] > 0.1 are labeled by VCC number.

The third column of Figure 22 suggests that the smallest galaxies in our sample exclusively have metallicities [Z/H] $\geqslant$ −0.5. Although this may seem counterintuitive, the relation is, in fact, driven by the small number of intrinsically rare, compact ellipticals in our sample: e.g., VCC 1192, VCC 1199, and VCC 1627. These galaxies, despite their low masses and compact sizes, have some of the oldest ages and highest metallicities in our sample. This would be consistent with the notion that they represent the tidally stripped relics of initially much more massive galaxies (Guérou et al. 2015).

The relationship between metallicity and Sérsic index in the fourth column of Figure 22 is likely another manifestation of the mass–metallicity relation. Dwarf ellipticals tend to have lower indices than their more massive counterparts (e.g., Caon et al. 1993; Ferrarese et al. 2006a; Mahajan et al. 2015), so the Sérsic index effectively traces mass.

6.3. α-element Abundances

The α-element abundance [α/Fe] is known to trace star formation timescales, with short timescales corresponding to higher [α/Fe] values. Type II supernovae from the most massive, rapidly evolving stars eject relatively large amounts of α elements. The [α/Fe] of the galaxy only begins to decrease after less α-enhanced ejecta from Type Ia supernovae begin to appear. Previous results for low-mass galaxies show that their star formation timescales are regulated by the density of their environment, with galaxies in the densest regions having both supersolar [α/Fe] and higher GC specific frequencies (Liu et al. 2016). In addition, GCs in early-type galaxies are known to have supersolar [α/Fe] (Puzia et al. 2005). Therefore, the [α/Fe] of nuclei may indicate the importance of environment and/or GC infall in nucleus formation.

Although our spectroscopic analysis does not include the galaxies in our sample, we can still investigate any trends among the 19 nuclei for which we have measured [α/Fe]. We show [α/Fe] as a function of galaxy mass, distance to M87, galaxy r_e, and galaxy n in Figure 23. There are no clear trends, with most nuclei having roughly solar [α/Fe] regardless of environment or galaxy properties. However, it is interesting to note that the galaxies VCC 1407 and VCC 1539, which were found to have supersolar [α/Fe] and high GC specific frequency by Liu et al. (2016), have similar [α/Fe] in their nuclei. The VCC 1185 galaxy also has a similarly high [α/Fe], but its nucleus has [α/Fe] = −0.04, and it has a low GC

specific frequency for its [α/Fe]. In general, though, the lack of significant α enhancement suggests that nuclei have not formed through particularly brief star formation episodes. A more thorough investigation of the connections among nuclei, GC populations, and [α/Fe] is beyond the scope of this paper.

6.4. Ages

As discussed previously, measuring accurate ages for SSP populations older than a few Gyr can be challenging, given the similarities among the model spectra within one model family, and the differences between predictions from various codes (Powalka et al. 2016). Therefore, our age estimates are hampered by somewhat large uncertainties and any apparent trends should be considered with caution.

As can be seen in the left panel of the third row of Figure 22, there appear to be two populations, clustered distinctly in age, among the galaxies and the nuclei. The most massive objects ($M_{\star,\mathrm{gal}} \geqslant 2 \times 10^9\,M_\odot$) contain nuclei that are consistently older, with typical ages of $\sim$7 Gyr, than the lower-mass nuclei (which have ages scattered around 4 Gyr). The overall age distributions for galaxies and nuclei (shown in the far right panel of the third row) appear quite similar, and there are no clear age offsets between the two types of object. However, the age differences in the bottom-right panel do have a tail toward positive values in which the galaxy is older than the nucleus.

The density of the surrounding environment, as traced by distance from M87, does not appear to have a strong effect on the galaxies or the nuclei. There is perhaps some evidence that older objects tend to be found in higher density environments, as expected if the earliest objects to fall into the Virgo Cluster are now found close to the bottom of the cluster potential. Having been stripped of any gas upon infall, only old stellar populations would remain.

We reiterate that the derived ages are SSP-equivalent ages. The galaxies almost certainly host complex populations, and it is quite possible that nuclei consist of multiple stellar populations. As a result, fitting an SSP model introduces some bias and uncertainty. If the actual stellar content is primarily that of an old population, even a small contribution from a substantially younger population could skew the SSP-equivalent, luminosity-weighted age. Also, the results of this work do not consider the effect of dust extinction. Future analyses should consider stellar populations that are more complex than SSPs and explore the possibility of non-zero dust extinction.
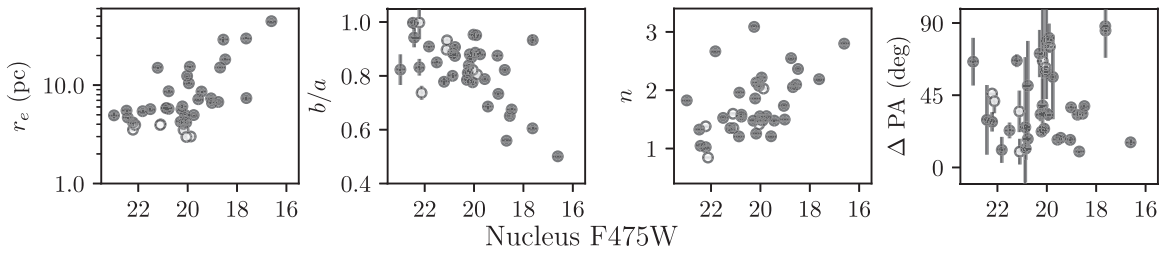
Figure 24. Trends in nucleus effective radius, axis ratio, Sérsic index, and position angle offset between the nucleus and galaxy, plotted as a function of nucleus F475W magnitude. Open circles denote nuclei that we consider marginally resolved ($r_e < 4$ pc or $0''05$) and as such have less robust structural measurements. All parameters were measured using a single Sérsic component fitted to the nucleus using GALFIT as described in Section 3.2 with the exception of the galaxy position angle (see the text for details).

6.5. Structural Parameters of Nuclei

By fitting each nucleus with a Sérsic profile, we can measure not only its effective radius, r_e, but also its concentration index n, axis ratio b/a, and position angle PA. However, for nuclei that are only marginally resolved, these structural parameters are clearly not very meaningful—after convolving the model with the PSF, any intrinsic flattening would go unnoticed. Nevertheless, in this section, we look for possible trends in r_e, b/a, n, and the offset between nucleus and galaxy PA, ΔPA. Because most of the galaxies were modeled with multiple components in our 2D decomposition, there is no single PA that we can provide for the galaxy. Therefore, we estimate a mean PA from the ELLIPSE isophotes between $1''$ and $1r_e$, with r_e determined through a curve of growth analysis (L. Ferrarese et al. 2017, in preparation).

We searched for trends in these structural parameters as a function of magnitude, environment, metallicity, and color, finding that most parameters are tightly correlated with nucleus magnitude. In Figure 24, we show the nucleus r_e, b/a, n and ΔPA as a function of nucleus magnitude. Côté et al. (2006) determined the resolution limit for ACSVCS images to be 2 pc, so we consider nuclei with $r_e < 4$ pc ($0''05$) to be marginally resolved. Seven nuclei meet this criterion and are indicated by open circles in the figure. Looking over these nuclei, some trends emerge. Unsurprisingly, the brightest nuclei tend to be larger (Côté et al. 2006) and have larger Sérsic indices compared to the fainter nuclei. Indeed, the trends in these nuclear parameters mimic what we observe for the galaxies. However, it is interesting to note that as nucleus luminosity increases, the nuclei become more flattened and are weakly aligned with the semimajor axis of the host galaxy. If this flattening is indicative of rotation, then it is likely that these nuclei formed predominantly via dissipative processes when gas falls to the center of the galaxy and forms a rotating disk. On the other hand, recent dissipationless models have been able to produce a rotating, flattened nucleus as well (Tsatsi et al. 2017). Understanding the significance of the observed trends may shed light on the various formation scenarios, although it is already clear that kinematic information with high spatial and spectral resolution would be extremely useful in discriminating between the competing models. For now, we simply note that these results suggest that different formation mechanisms may dominate in different regimes of nucleus and galaxy mass (Turner et al. 2012).

6.6. Coexistence with SMBHs

Many studies have established that both a nucleus and SMBH exist in the Milky Way (e.g., Becklin & Neugebauer

1968; Schödel et al. 2007; Ghez et al. 2008), a situation that is true of some other galaxies as well (Seth et al. 2008; Neumayer & Walcher 2012). In this section, we investigate whether any nuclei in our sample might contain an SMBH as well—a possibility that bears consideration following the recent discovery of an SMBH in a Virgo UCD (Seth et al. 2014). In addition, the various proposed modes of SMBH formation produce different occupation fractions in this regime of galaxy mass, so SMBH detections can be a valuable constraint in our understanding of SMBH formation and galaxy evolution (Volonteri 2010; Greene 2012).

To test this possible coexistence, we adopt the black hole mass to galaxy mass relation from McConnell & Ma (2013),

$$\begin{aligned} \log_{10}(M_\bullet) = &(8.46 \pm 0.08) \\ &+ (1.05 \pm 0.11)\log_{10}(M_{\star,\mathrm{bulge}}/10^{11}\,M_\odot), \end{aligned} \quad (6)$$

where $M_\bullet$ is the mass of the SMBH and $M_{\star,\mathrm{bulge}}$ is equal to the galaxy stellar mass for early-type galaxies. For a simple, first-order approach, we assume that this relation applies for the total "compact massive object" (CMO) mass (Ferrarese et al. 2006b), noting that previous work suggests nuclei and SMBHs may follow separate mass relations (Balcells et al. 2007; Graham 2012; Leigh et al. 2012; Scott & Graham 2013). We then highlight any nucleus that deviates from the expected relation at the 3σ level or more.

The results of this exercise are shown in Figure 25, along with any confirmed SMBH masses based on X-ray detections in the AMUSE-Virgo survey (Gallo et al. 2010). VCC 140 is an undermassive outlier nucleus; an SMBH of $\sim 10^{6.4}\,M_\odot$ would be necessary to match the relation from Equation (6). We also consider galaxies in our sample that may have overmassive nuclei. Significant outliers in this region include the compact ellipticals VCC 1192 and VCC 1199, and the bright galaxies VCC 1146 and VCC 1242, which have structurally complex inner regions. One might expect to find compact ellipticals in this region if they are indeed the tidally stripped relics of more massive galaxies that hosted a similarly massive nucleus. Meanwhile, the nuclei of galaxies such as VCC 1146 and VCC 1242 seem to be markedly different morphologically from other nuclei (Turner et al. 2012), which may be evidence that these nuclei have experienced a different evolutionary path, perhaps leading to increased growth of the CMO.

7. Summary

We carried out a comprehensive analysis of the stellar populations and masses of 39 nuclei belonging to early-type
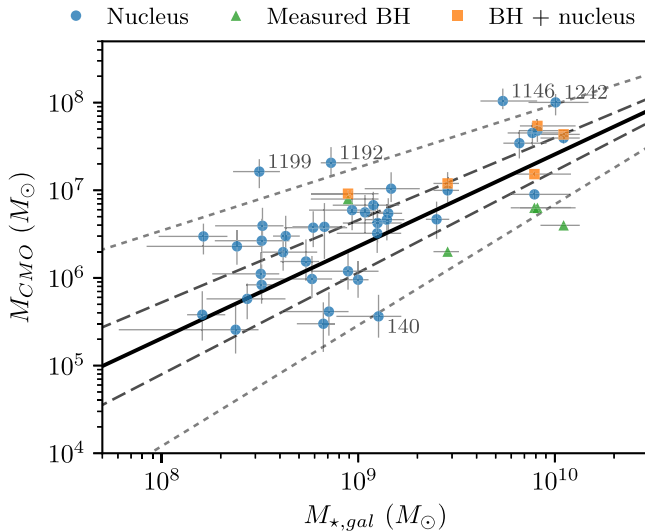
Figure 25. Relationship between galaxy stellar mass and the mass of the central massive object (CMO), including confirmed black holes within nuclei. The solid line shows the relation from McConnell & Ma (2013) with the 1σ and 3σ uncertainties indicated by the dashed and dotted lines, respectively. The stellar masses of our nuclei are shown as blue circles. Green triangles indicate black hole detections from AMUSE-Virgo (Gallo et al. 2010), while orange squares show the total mass of these black holes and their corresponding nuclei. Objects that fall outside the 3σ region are labeled with their VCC numbers.

galaxies in the Virgo cluster. The UV, optical, and infrared data sets that form the basis of our analysis—consisting of both imaging and spectroscopy—are the most extensive ever used to characterize the stellar content of nuclei in nearby, early-type galaxies. Our photometric analysis rests on multiband imaging from *HST* (ACS, WFPC2, and NICMOS) and CFHT (Mega-Cam and WIRCam) that was collected in the course of the Virgo Redux survey, ACSVCS (Côté et al. 2004), and NGVS (Ferrarese et al. 2012). For 19 of our program nuclei, we also analyzed long-slit and/or IFU optical spectroscopy from the Keck II (DEIMOS and ESI) and Gemini South (GMOS) telescopes.

Nucleus and galaxy magnitudes were extracted using two methods: (1) a two-component (nucleus and galaxy) surface brightness profile decomposition, using composite profiles created from the high-resolution *HST* data combined with deep, wide-field CFHT data, and (2) a multicomponent image decomposition, allowing for more complex galaxy structure, using GALFIT. After a careful comparison of the two methods, the two-dimensional approach was used to produce our final photometric measurements for the extracted nucleus and its host. Through MCMC fitting of the spectral energy distributions to various sets of SSP models, we determined robust mass and metallicity measurements, as well as broad age estimates. Parameters obtained from our photometric analysis were compared to the spectroscopic results, derived homogeneously using the EZ-AGES code (Schiavon 2007; Graves & Schiavon 2008).

The main results of this work can be summarized as follows.

1. Regardless of the choice of SSP model, there are no strong systematic trends in the derived properties. The Maraston (2005) models can produce a broader, younger range of ages for the sample, likely due to their treatment of the TP-AGB stellar evolutionary phase. Nuclei stellar population parameters derived from the Keck-DEIMOS, Keck-ESI, and Gemini-GMOS spectra show good

internal agreement, despite the different instrumental setups.

2. A comparison of spectroscopic age and metallicity estimates in the literature for the nuclei and galaxies in our sample shows a significant level of scatter among the measured parameters. Some variations may be due to differences in model assumptions (i.e., adopted isochrones, spectral libraries, and stellar evolution treatments) or data analysis methods (i.e., the radius selected for analysis or decomposition techniques). Although homogeneous data sets should still provide reliable relative age and metallicity estimates, this comparison suggests that conclusions on the stellar populations in the nuclei, and differences with respect to their host galaxies, should be viewed with caution.

3. The photometric metallicities are in reasonable agreement with those derived from spectroscopy for the nuclei, with an rms scatter of $\sim$0.3 dex. Photometric ages are scattered around 4 Gyr, although spectroscopic ages can be as old as 12 Gyr. This discrepancy may be caused by (1) loss of age sensitivity for old stellar populations in optical spectra or (2) the possible presence of a small young stellar population that can enhance the blue-optical and UV fluxes in the nuclei. The limited age resolution at old and intermediate ages available from SED fitting is due, in part, to the modest S/N in the UV data, and the underlying assumption of pure SSP populations (which can display similar broadband features for most ages older than a few Gyr).

4. Our computed stellar masses (measured from SED fitting to six to ten photometric bands) are accurate to typical precisions of 35%. This is nearly a factor of two improvement over previous measurements that have usually been derived using just one or two photometric bands with assumed ages and/or metallicities (Ferrarese et al. 2006a; Leigh et al. 2012; Georgiev et al. 2016). Over the range of $10^{8.4}$ to $10^{10.3}\ M_\odot$ in galaxy stellar mass for our galaxies, the nuclei are found to contribute a fraction of $0.33^{+0.09}_{-0.07}\%$ of the total stellar mass, consistent with previous results for early-type galaxies based on less precise stellar masses for the nuclei and simpler nucleus–galaxy decompositions (Côté et al. 2006; Ferrarese et al. 2006a; Turner et al. 2012). The M_{nuc} versus M_{gal} relation is also consistent with new results from R. Sánchez-Janssen (2017, in preparation), which extend the relation to much lower masses (after combining the observed *i*-band luminosities with an assumed $M/L = 1$).

5. The nuclei show evidence for a rather steep mass–metallicity relation of the form $\log_{10} Z/Z_\odot \propto \alpha \log_{10} M_\star$ with $\alpha = 0.41 \pm 0.05$. A similar trend is exhibited by UCDs (with masses $10^6 \leqslant M_\star \leqslant 10^{7.3}\ M_\odot$) in the Virgo core region, although the UCDs are more metal-poor, by 0.56 ± 0.12 dex, at fixed mass. The galaxies follow the slope of the relation measured in Ma et al. (2016), but systematically shifted to higher metallicities by $\sim$0.3 dex.

6. Nuclei metallicities are statistically indistinguishable from those of their hosts, appearing 0.07 ± 0.3 dex more metal-rich on average. However, excluding outlier galaxies (i.e., compact ellipticals and morphologically unusual galaxies) that do not follow the mass–metallicity relationship, nuclei are 0.20 ± 0.28 dex more metal-rich

than their hosts, qualitatively consistent with conclusions from previous studies (Chilingarian 2009; Koleva et al. 2011; Paudel et al. 2011). There is no clear age difference, with nuclei ages showing a broad distribution between ~3 and ~12 Gyr.

7. There is a clear trend for the brightest nuclei to be the most flattened; these bright nuclei may also be more closely aligned with the major axes of their hosts. Due to the barely resolved sizes of the fainter nuclei, it is unclear how these trends manifest in the fainter regimes. However, this suggests that the largest nuclei—which belong to galaxies with stellar masses greater than $\sim10^{9.5}M_{\odot}$—may be formed predominantly through dissipative processes that can induce flattening and rotation.

A number of questions regarding the stellar populations and the formation of nuclei remain unanswered. This work adopted a fairly simple approach to the stellar populations of the nuclei. Future work should consider the effects of internal extinction as well as more complex stellar populations, which may provide a better understanding of the systematics of the age estimates. Given current predictions from formation scenarios, it is still difficult to determine how much each mechanism might contribute to the formation of a particular nucleus, or whether certain processes become more important in different regimes of mass, environment, or other properties. This could be addressed with model predictions for not only size, mass, and velocity dispersion relations, but also ages and abundances, which would provide more points of comparison with observations. While some models have presented qualitative statements about the ages of nuclei relative to their hosts (Bekki 2007), precise predictions for relative or absolute ages could prove useful. Simulations that include multiple processes of nucleus formation, such as those in Antonini et al. (2015), would be ideal for investigating the relative contributions of dissipative and dissipationless processes, and any differences these may produce in abundance and age distributions.

The present study has focused on a somewhat limited sample of nuclei—in the sense that we have explored a restricted morphological type and mass range for the host galaxies—so we do not yet have a complete picture of the nucleus population. Fortunately, many hundreds of nucleated galaxies are available in the NGVS survey area. By applying our methods to the full sample in NGVS, albeit with a smaller number of photometric bands, it should be possible to examine the nucleation fraction, stellar population parameters, and scaling relations for a greatly expanded number of nuclei. This will include exploring a new and important regime in galaxy mass (see, e.g., R. Sánchez-Janssen et al. 2017, in preparation, for first results). The large numbers of UCDs and GCs detected in the NGVS imaging should also enable a full comparison of the properties of compact stellar systems within a single, homogeneous data set (Powalka et al. 2016; Liu et al. 2015).

ORCID iDs

Chelsea Spengler ● https://orcid.org/0000-0002-1685-4284
Patrick Côté ● https://orcid.org/0000-0003-1184-8114
Joel Roediger ● https://orcid.org/0000-0002-0363-4266
Laura Ferrarese ● https://orcid.org/0000-0002-8224-1128
Rubén Sánchez-Janssen ● https://orcid.org/0000-0003-4945-0056
Elisa Toloba ● https://orcid.org/0000-0001-6443-5570
Puragra Guhathakurta ● https://orcid.org/0000-0001-8867-4234
Andrew Zirm ● https://orcid.org/0000-0002-6707-275X
Roberto Muñoz ● https://orcid.org/0000-0003-1743-0456
Thomas Puzia ● https://orcid.org/0000-0003-0350-7061
Ariane Lançon ● https://orcid.org/0000-0002-7214-8296
Eric W. Peng ● https://orcid.org/0000-0002-2073-2781
Simona Mei ● https://orcid.org/0000-0002-2849-559X
Mathieu Powalka ● https://orcid.org/0000-0002-1218-3276

References

Allington-Smith, J., Murray, G., Content, R., et al. 2002, PASP, 114, 892
Anders, P., Bissantz, N., Fritze-v. Alvensleben, U., & de Grijs, R. 2004, MNRAS, 347, 196
Antonini, F., Barausse, E., & Silk, J. 2015, ApJ, 812, 72
Antonini, F., Capuzzo-Dolcetta, R., Mastrobuono-Battisti, A., & Merritt, D. 2012, ApJ, 750, 111
Astropy Collaboration, Robitaille, T. P., Tollerud, E. J., et al. 2013, A&A, 558, A33
Balcells, M., Graham, A. W., & Peletier, R. F. 2007, ApJ, 665, 1084
Barlow, T. A., & Sargent, W. L. W. 1997, AJ, 113, 136
Becklin, E. E., & Neugebauer, G. 1968, ApJ, 151, 145
Bekki, K. 2007, PASA, 24, 77
Bekki, K. 2015, ApJL, 812, L14
Bertin, E. 2011, in ASP Conf. Ser. 442, Astronomical Data Analysis Software and Systems XX, ed. I. N. Evans et al. (San Francisco, CA: ASP), 435
Binggeli, B., Sandage, A., & Tammann, G. A. 1985, AJ, 90, 1681
Blakeslee, J. P., Jordán, A., Mei, S., et al. 2009, ApJ, 694, 556
Böker, T., Laine, S., van der Marel, R. P., et al. 2002, AJ, 123, 1389
Böker, T., Sarzi, M., McLaughlin, D. E., et al. 2004, AJ, 127, 105
Boulade, O., Charlot, X., Abbon, P., et al. 2003, Proc. SPIE, 4841, 72
Bourne, M. A., & Power, C. 2016, MNRAS, 456, L20
Bruzual, G., & Charlot, S. 2003, MNRAS, 344, 1000
Butler, D. J., & Martínez-Delgado, D. 2005, AJ, 129, 2217
Caon, N., Capaccioli, M., & D'Onofrio, M. 1993, MNRAS, 265, 1013
Cappellari, M., McDermid, R. M., Alatalo, K., et al. 2012, Natur, 484, 485
Capuzzo-Dolcetta, R., & Miocchi, P. 2008, MNRAS, 388, L69
Carollo, C. M., Stiavelli, M., de Zeeuw, P. T., & Mack, J. 1997, AJ, 114, 2366
Carollo, C. M., Stiavelli, M., & Mack, J. 1998, AJ, 116, 68
Carson, D. J., Barth, A. J., Seth, A. C., et al. 2015, AJ, 149, 170

Chilingarian, I. V. 2009, MNRAS, 394, 1229
Chilingarian, I. V., Sil'Chenko, O. K., Afanasiev, V. L., & Prugniel, P. 2007, AstL, 33, 292
Cleveland, W. S. 1979, J. Am. Stat. Assoc., 74, 829
Cole, D. R., Debattista, V. P., Varri, A. L., Hartmann, M., & Seth, A. C. 2017, MNRAS, 466, 2895
Conroy, C., & Gunn, J. E. 2010, ApJ, 712, 833
Côté, P., Blakeslee, J. P., Ferrarese, L., et al. 2004, ApJS, 153, 223
Côté, P., Piatek, S., Ferrarese, L., et al. 2006, ApJS, 165, 57
Crockett, R. M., Kaviraj S., Silk, J. I., et al. 2011, ApJ, 727, 115
De Looze, I., Baes, M., Zibetti, S., et al. 2010, A&A, 518, L54
de Meulenaer, P., Narbutis, D., Mineikis, T., & Vansevičius, V. 2014, A&A, 569, A4
den Brok, M., Peletier, R. F., Seth, A., et al. 2014, MNRAS, 445, 2385
di Serego Alighieri, S., Bianchi, S., Pappalardo, C., et al. 2013, A&A, 552, A8
Drinkwater, M. J., Gregg, M. D., Hilker, M., et al. 2003, Natur, 423, 519
Durrell, P. R., Côté, P., Peng, E. W., et al. 2014, ApJ, 794, 103
Faber, S. M., Phillips, A. C., Kibrick, R. I., et al. 2003, Proc. SPIE, 4841, 1657
Fan, Z., & de Grijs, R. 2012, MNRAS, 424, 2009
Fan, Z., & de Grijs, R. 2014, ApJS, 211, 22
Ferrarese, L., Côté, P., Cuillandre, J.-C., et al. 2012, ApJS, 200, 4
Ferrarese, L., Côté, P., Dalla Bontà, E., et al. 2006a, ApJL, 644, L21
Ferrarese, L., Côté, P., Jordán, A., et al. 2006b, ApJS, 164, 334
Fioc, M., & Rocca-Volmerange, B. 1997, A&A, 326, 950
Fioc, M., & Rocca-Volmerange, B. 1999, arXiv:astro-ph/9912179
Ford, H. C., Bartko, F., Bely, P. Y., et al. 1998, Proc. SPIE, 3356, 234
Foreman-Mackey, D. 2016, JOSS, 24
Foreman-Mackey, D., Hogg, D. W., Lang, D., & Goodman, J. 2013, PASP, 125, 306
Gallo, E., Treu, T., Marshall, P. J., et al. 2010, ApJ, 714, 25
Geha, M., Guhathakurta, P., & van der Marel, R. P. 2002, AJ, 124, 3073
Georgiev, I. Y., & Böker, T. 2014, MNRAS, 441, 3570
Georgiev, I. Y., Böker, T., Leigh, N., Lützgendorf, N., & Neumayer, N. 2016, MNRAS, 457, 2122
Georgiev, I. Y., Goudfrooij, P., & Puzia, T. H. 2012, MNRAS, 420, 1317
Ghez, A. M., Salim, S., Weinberg, N. N., et al. 2008, ApJ, 689, 1044
Glass, L., Ferrarese, L., Côté, P., et al. 2011, ApJ, 726, 31
Gnedin, O. Y., Ostriker, J. P., & Tremaine, S. 2014, ApJ, 785, 71
Goerdt, T., Moore, B., Kazantzidis, S., et al. 2008, MNRAS, 385, 2136
Goudfrooij, P., & Kruijssen, J. M. D. 2014, ApJ, 780, 43
Graham, A. W. 2012, MNRAS, 422, 1586
Graves, G. J., & Schiavon, R. P. 2008, ApJS, 177, 446
Greene, J. E. 2012, NatCo, 3, 1304
Guérou, A., Emsellem, E., McDermid, R. M., et al. 2015, ApJ, 804, 70
Guillard, N., Emsellem, E., & Renaud, F. 2016, MNRAS, 461, 3620
Gwyn, S. D. J. 2008, PASP, 120, 212
Häussler, B., McIntosh, D. H., Barden, M., et al. 2007, ApJS, 172, 615
Hempel, M., Hilker, M., Kissler-Patig, M., et al. 2003, A&A, 405, 487
Hook, I. M., Jørgensen, I., Allington-Smith, J. R., et al. 2004, PASP, 116, 425
Janz, J., Laurikainen, E., Lisker, T., et al. 2012, ApJL, 745, L24
Janz, J., & Lisker, T. 2008, ApJL, 689, L25
Janz, J., & Lisker, T. 2009, ApJL, 696, L102
Janz, J., Norris, M. A., Forbes, D. A., et al. 2016, MNRAS, 456, 617
Jedrzejewski, R. I. 1987, MNRAS, 226, 747
Jordán, A., Blakeslee, J. P., Peng, E. W., et al. 2004a, ApJS, 154, 509
Jordán, A., Côté, P., West, M. J., et al. 2004b, AJ, 127, 24
Kannappan, S. J., & Gawiser, E. 2007, ApJL, 657, L5
Kaviraj, S., Crockett, R. M., Whitmore, B. C., et al. 2012, MNRAS, 422, L96
Kaviraj, S., Rey, S.-C., Rich, R. M., Yoon, S.-J., & Yi, S. K. 2007a, MNRAS, 381, L74
Kaviraj, S., Schawinski, K., Devriendt, J. E. G., et al. 2007b, ApJS, 173, 619
Kim, S., Rey, S.-C., Jerjen, H., et al. 2014, ApJS, 215, 22
King, I. R. 1966, AJ, 71, 64
Koleva, M., Prugniel, P., de Rijcke, S., & Zeilinger, W. W. 2011, MNRAS, 417, 1643
Kuntschner, H. 2004, A&A, 426, 737
Lange, R., Moffett, A. J., Driver, S. P., et al. 2016, MNRAS, 462, 1470
Leigh, N., Böker, T., & Knigge, C. 2012, MNRAS, 424, 2130
Li, A., & Draine, B. T. 2001, ApJ, 554, 778
Li, Z., Han, Z., & Zhang, F. 2007, A&A, 464, 853
Lisker, T., Janz, J., Hensler, G., et al. 2009, ApJL, 706, L124
Liu, C., Peng, E. W., Côté, P., et al. 2015, ApJ, 812, 34
Liu, Y., Ho, L. C., & Peng, E. 2016, ApJL, 829, L26
Lotz, J. M., Miller, B. W., & Ferguson, H. C. 2004, ApJ, 613, 262

Lotz, J. M., Telford, R., Ferguson, H. C., et al. 2001, ApJ, 552, 572
Ma, X., Hopkins, P. F., Faucher-Giguère, C.-A., et al. 2016, MNRAS, 456, 2140
Mahajan, S., Drinkwater, M. J., Driver, S., et al. 2015, MNRAS, 446, 2967
Maraston, C. 2005, MNRAS, 362, 799
McConnell, N. J., & Ma, C.-P. 2013, ApJ, 764, 184
McDermid, R. M., Alatalo, K., Blitz, L., et al. 2015, MNRAS, 448, 3484
McLaughlin, D. E., King, A. R., & Nayakshin, S. 2006, ApJL, 650, L37
Mei, S., Blakeslee, J. P., Côté, P., et al. 2007, ApJ, 655, 144
Mendel, J. T., Simard, L., Palmer, M., Ellison, S. L., & Patton, D. R. 2014, ApJS, 210, 3
Mentz, J. J., La Barbera, F., Peletier, R. F., et al. 2016, MNRAS, 463, 2819
Mieske, S., Frank, M. J., Baumgardt, H., et al. 2013, A&A, 558, A14
Mieske, S., Hilker, M., Jordán, A., et al. 2008, A&A, 487, 921
Mihos, J. C., & Hernquist, L. 1994, ApJL, 437, L47
Milosavljević, M. 2004, ApJL, 605, L13
Muñoz, R. P., Puzia, T. H., Lançon, A., et al. 2014, ApJS, 210, 4
Muzzin, A., Marchesini, D., van Dokkum, P. G., et al. 2009, ApJ, 701, 1839
Neumayer, N., & Walcher, C. J. 2012, AdAst, 2012, 709038
Norris, M. A., Kannappan, S. J., Forbes, D. A., et al. 2014, MNRAS, 443, 1151
Oh, K. S., & Lin, D. N. C. 2000, ApJ, 543, 620
Paudel, S., Lisker, T., & Kuntschner, H. 2011, MNRAS, 413, 1764
Peng, C. Y., Ho, L. C., Impey, C. D., & Rix, H.-W. 2002, AJ, 124, 266
Peng, C. Y., Ho, L. C., Impey, C. D., & Rix, H.-W. 2010, AJ, 139, 2097
Pfeffer, J., & Baumgardt, H. 2013, MNRAS, 433, 1997
Pfeffer, J., Griffen, B. F., Baumgardt, H., & Hilker, M. 2014, MNRAS, 444, 3670
Phillips, A. C., Illingworth, G. D., MacKenty, J. W., & Franx, M. 1996, AJ, 111, 1566
Powalka, M., Lançon, A., Puzia, T. H., et al. 2016, ApJS, 227, 12
Puget, P., Stadler, E., Doyon, R., et al. 2004, Proc. SPIE, 5492, 978
Puzia, T. H., Kissler-Patig, M., Thomas, D., et al. 2005, A&A, 439, 997
Puzia, T. H., Zepf, S. E., Kissler-Patig, M., et al. 2002, A&A, 391, 453
Roediger, J. C., Ferrarese, L., Côté, P., et al. 2017, ApJ, 836, 120
Rossa, J., van der Marel, R. P., Böker, T., et al. 2006, AJ, 132, 1074
Salim, S., Rich, R. M., Charlot, S., et al. 2007, ApJS, 173, 267
Schiavon, R. P. 2007, ApJS, 171, 146
Schinnerer, E., Böker, T., Meier, D. S., & Calzetti, D. 2008, ApJL, 684, L21
Schlafly, E. F., & Finkbeiner, D. P. 2011, ApJ, 737, 103
Schödel, R., Eckart, A., Alexander, T., et al. 2007, A&A, 469, 125
Schweizer, F. 1979, ApJ, 233, 23
Scott, N., & Graham, A. W. 2013, ApJ, 763, 76
Seth, A., Agüeros, M., Lee, D., & Basu-Zych, A. 2008, ApJ, 678, 116
Seth, A. C., Dalcanton, J. J., Hodge, P. W., & Debattista, V. P. 2006, AJ, 132, 2539
Seth, A. C., van den Bosch, R., Mieske, S., et al. 2014, Natur, 513, 398
Sheinis, A. I., Bolte, M., Epps, H. W., et al. 2002, PASP, 114, 851
Stetson, P. B. 1987, PASP, 99, 191
Stetson, P. B. 1993, in IAU Coll. 136, Stellar Photometry—Current Techniques and Future Developments, ed. C. J. Butler & I. Elliott (Cambridge: Cambridge Univ. Press), 291
Taylor, E. N., Hopkins, A. M., Baldry, I. K., et al. 2011, MNRAS, 418, 1587
Thomas, D., Maraston, C., & Bender, R. 2003, MNRAS, 339, 897
Thompson, R. I. 1994, Proc. SPIE, 2209, 319
Toloba, E., Li, B., Guhathakurta, P., et al. 2016, ApJ, 822, 51
Trager, S. C., Faber, S. M., Worthey, G., & González, J. J. 2000, AJ, 119, 1645
Tremaine, S. D., Ostriker, J. P., & Spitzer, L., Jr. 1975, ApJ, 196, 407
Tsatsi, A., Mastrobuono-Battisti, A., van de Ven, G., et al. 2017, MNRAS, 464, 3720
Turner, M. L., Côté, P., Ferrarese, L., et al. 2012, ApJS, 203, 5
Vazdekis, A. 1999, ApJ, 513, 224
Volonteri, M. 2010, A&ARv, 18, 279
Walcher, C. J., Böker, T., Charlot, S., et al. 2006, ApJ, 649, 692
Walcher, C. J., van der Marel, R. P., McLaughlin, D., et al. 2005, ApJ, 618, 237
Wehner, E. H., & Harris, W. E. 2006, ApJL, 644, L17
Weiss, A., Salaris, M., Ferguson, J. W., & Alexander, D. R. 2006, arXiv:astro-ph/0605666
Worthey, G., Faber, S. M., Gonzalez, J. J., & Burstein, D. 1994, ApJS, 94, 687
Yamada, Y., Arimoto, N., Vazdekis, A., & Peletier, R. F. 2006, ApJ, 637, 200
Yi, S. K., Yoon, S.-J., Kaviraj, S., et al. 2005, ApJL, 619, L111
Zhang, H.-X., Peng, E. W., Côté, P., et al. 2015, ApJ, 802, 30